

1 **Characterizing regional oceanography and bottom environmental conditions at two**  
2 **contrasting sponge grounds on the northern Labrador Shelf.**

3 *Evert de Froe<sup>1,2,3\*</sup>, Igor Yashayaev<sup>4</sup>, Christian Mohn<sup>5</sup>, Johanne Vad<sup>6</sup>, Furu Mienis<sup>1</sup>, Gerard*  
4 *Duineveld<sup>1</sup>, Ellen Kenchington<sup>4</sup>, Erica Head<sup>4</sup>, Steve W. Ross<sup>7</sup>, Sabena Blackbird<sup>8</sup>, George A.*  
5 *Wolff<sup>8</sup>, Murray Roberts<sup>6</sup>, Barry MacDonald<sup>4</sup>, Graham Tulloch<sup>9</sup>, Dick van Oevelen<sup>10</sup>*

6 <sup>1</sup> NIOZ Royal Netherlands Institute for Sea Research, Department of Ocean Systems, PO  
7 Box 59, 1790 AB, Den Burg, the Netherlands

8 <sup>2</sup> Centre for Fisheries Ecosystems Research, Fisheries and Marine Institute of Memorial  
9 University of Newfoundland and Labrador, St. John's, Newfoundland and Labrador, Canada

10 <sup>3</sup> Wageningen Marine Research, Wageningen University and Research, PO Box 77, 4400 AB  
11 Yerseke, the Netherlands

12 <sup>4</sup> Bedford Institute of Oceanography, Department of Fisheries and Oceans, PO Box 1006,  
13 Dartmouth, NS, Canada B2Y 4A2

14 <sup>5</sup> Department of Ecoscience, Aarhus University, Frederiksborgvej 399, 4000 Roskilde,  
15 Denmark

16 <sup>6</sup> Changing Oceans Research Group, School of GeoSciences, The University of Edinburgh,  
17 Edinburgh, United Kingdom

18 <sup>7</sup> Univ. of North Carolina at Wilmington, Center for Marine Science, 5600 Marvin Moss Ln.,  
19 Wilmington, NC, 28409 USA

20 <sup>8</sup> School of Environmental Sciences, University of Liverpool, 4 Brownlow Street, Liverpool,  
21 L69 3GP, UK.

22 <sup>9</sup> British Geological Survey, Lyell Centre, Research Avenue South, Edinburgh, EH14 4AP

23 <sup>10</sup> NIOZ Royal Netherlands Institute for Sea Research, Department of Estuarine and Delta  
24 Systems, PO Box 140, 4400 AC, Yerseke, the Netherlands

25

26

27 **\*Corresponding author:** [evert.defroe@wur.nl](mailto:evert.defroe@wur.nl)

28

29 Key words: deep-sea sponges, sponge grounds, benthic-pelagic coupling, organic matter  
30 transport, tidal dynamics, nutrients

31

33 Deep-sea sponge grounds are distributed globally and are considered hotspots of biological  
34 diversity and biogeochemical cycling. To date, little is known about the environmental  
35 conditions that allow high sponge biomass to develop in the deep sea. Here, we characterize  
36 oceanographic conditions at two contrasting sites off the northern Labrador Shelf with high-  
37 and low-sponge-biomass. Data were collected by year-long benthic lander deployments  
38 equipped with current meters, a turbidity and chlorophyll-*a* measuring device, and a sediment  
39 trap. Additionally, regional oceanography was described by analysing vertical conductivity -  
40 temperature-depth (CTD) casts, Argo float profiles, and surface buoy drifter data for the  
41 northern Labrador Shelf from 2005 to 2022. Stable isotopic composition of benthic fauna was  
42 determined to investigate food web structure at the sponge grounds. Our results revealed strong  
43 ( $0.26 \pm 0.14 \text{ m s}^{-1}$ ; mean  $\pm$  SD) semidiurnal tidal currents at the high-sponge-biomass site, but  
44 twofold weaker currents ( $0.14 \pm 0.08 \text{ m s}^{-1}$ ; mean  $\pm$  SD) at the low-sponge-biomass site. Tidal  
45 analysis suggests that, at the high-sponge-biomass site, kinetic energy is dissipated from  
46 barotropic tide to baroclinic tide/turbulence, which could enhance food availability for benthic  
47 organisms. Bottom nutrient concentrations were elevated at the high-sponge-biomass site  
48 which would benefit growth in deep-sea sponges. Organic matter flux to the seafloor was  
49 increased at the high-sponge-biomass site and consisted of fresher material. Finally, both  
50 sponge grounds demonstrated tight benthic-pelagic coupling prior to the onset of stratification.  
51 Stable isotope signatures indicated that soft corals (*Primnoa resedaeformis*) fed on suspended  
52 particulate organic matter, while massive sponges (*Geodia* spp.) likely utilized additional food  
53 sources. Our results imply that benthic fauna at the high-sponge-biomass site benefit from  
54 strong tidal currents, which increases food supply, and favourable regional ocean currents that  
55 increase nutrient concentration in bottom waters.

58 Sponges are an ancient group of sessile filter feeders capable of pumping large quantities of  
59 water through their bodies (Vogel, 1977; Bergquist, 1978; Leys et al., 2011), thereby  
60 exchanging significant amounts of particulate- and dissolved organic matter and nutrients with  
61 the water column (e.g., van Duyl et al., 2008; Maldonado et al., 2012; Kahn et al., 2015; Rix  
62 et al., 2016). In the deep sea, sponges can form dense aggregations, known as sponge grounds,  
63 which are considered hotspots of macrofaunal diversity and abundance (Klitgaard, 1995; Buhl-  
64 Mortensen et al., 2010; Beazley et al., 2013; McIntyre et al., 2016), carbon- and nutrient cycling  
65 (Kutti et al., 2013; Cathalot et al., 2015; Maldonado et al., 2020a), and benthic-pelagic coupling  
66 (Pile and Young, 2006). Sponge grounds form complex habitats that provide breeding grounds  
67 and shelter for (commercially important) fish, increasing demersal fish biomass and diversity  
68 (Kenchington et al., 2013; Kutti et al., 2015; Meyer et al., 2019; Brodnicke et al., 2023).  
69 Finally, they are often classified as Vulnerable Marine Ecosystems (VMEs) as defined by the  
70 Food and Agriculture Organization of the United Nations (FAO, 2009).

71 Deep-sea sponge ecosystems are currently under threat from anthropogenic disturbances such  
72 as deep-water bottom trawling, deep-sea mining, and climate change. Pham et al. (2019) found  
73 that large quantities of sponges (~4% of total stock) have been removed by bottom trawling  
74 from sponge grounds on the Flemish Cap. Deep-sea sponges are especially vulnerable to  
75 bottom fishing due their longevity and slow growth (Leys and Lauzon, 1998; Hogg et al.,  
76 2010). Benthic trawling reduces the density and diversity of deep-sea sponge grounds  
77 (Morrison et al., 2020; Colaço et al., 2022), and recovery of disturbed sponge habitats can take  
78 decades to centuries (Vieira et al., 2020). In addition, prolonged exposure to elevated  
79 concentrations of suspended sediments, e.g. due to deep-sea mining, could adversely affect  
80 deep-sea sponges (Wurz et al., 2021). Recent studies suggest that climate change also impacts  
81 deep-sea benthic fauna (Brito-Morales et al., 2020; Jorda et al., 2020). For example, modelling  
82 predicted that the suitable area for *Vazella pourtalesii* on the Scotian Shelf would increase four-  
83 fold in the coming years due to warming of colder waters around its current habitat (Beazley  
84 et al., 2021). Nevertheless, research on the effect of climate change on deep-sea sponges is still  
85 in its infancy and to predict its effects on sponge grounds, a better understanding of the  
86 environmental conditions that favour their occurrence is needed.

87 In the past decades, research on deep-sea sponges has focused on their physiology and feeding  
88 behaviour (e.g., Leys and Lauzon, 1998; Yahel et al., 2007; Kahn et al., 2015; Robertson et al.,  
89 2017; Kazanidis et al., 2018; Maier et al., 2020b; Bart et al., 2021; de Kluijver et al., 2021),  
90 and assessing their spatial distributions using habitat suitability models (Knudby et al., 2013;

91 Howell et al., 2016; Beazley et al., 2018; Murillo et al., 2018). More recently, data on the  
92 environmental conditions where sponge grounds are found have been gathered using long-term  
93 measurements from lander-mounted equipment. These data indicate that sponge grounds are  
94 commonly found in areas with internal waves (Davison et al., 2019) and comparatively strong  
95 tidal currents which flush the seafloor with oxygen and nutrient-rich water, and with a high  
96 suspended particle matter load near the seabed (Roberts et al., 2018; Hanz et al., 2021a, 2021b).  
97 In addition, sponges can alter the hydrodynamic conditions of the benthic boundary layer by  
98 increasing the bottom roughness, creating conditions favourable for larval recruitment and  
99 suspended particle deposition (Abelson and Denny, 1997; Culwick et al., 2020). These studies  
100 show that sponge grounds are found in areas with a variety of environmental conditions, but  
101 little is known of the mechanisms controlling their spatial distribution or what controls their  
102 biomass.

103 The Canadian Atlantic continental shelf breaks and upper slopes, including the northern  
104 Labrador Shelf, host extensive sponge grounds (Kenchington et al., 2010; Knudby et al., 2013).  
105 Sponge assemblages occur over a large depth range (200 – 2875 m) and are often aligned along  
106 depth contours with presumably similar environmental conditions (Murillo et al., 2012;  
107 Knudby et al., 2013). On the northern Labrador Shelf and upper slope, sponge assemblages  
108 consist mostly of *Geodia* spp. and glass (hexactinellid) sponges (Kenchington et al., 2010) but  
109 with locally variable sponge biomass. Therefore, this region provides a suitable setting to study  
110 which environmental conditions favour high sponge biomass and to provide insight into the  
111 factors that drive the spatial distribution of sponge assemblages on the eastern Canadian Shelf.  
112 Furthermore, research on present environmental conditions on the seafloor is timely as the  
113 Labrador Shelf region is one of the fastest warming large marine ecosystems globally ( $\sim 1$  °C  
114 decade<sup>-1</sup>; Belkin, 2009), and according to ensemble-based climate change prediction, critical  
115 water mass properties there, including temperature, particulate organic carbon, pH, and  
116 aragonite saturation, are likely to change substantially by 2100 (Puerta et al., 2020). Recent  
117 work on the Labrador Sea also shows that Arctic sea-ice melt can impact the hydrographic  
118 conditions in this region (Yashayaev, 2024). Therefore, analysis of the contemporary  
119 conditions provides a baseline or a benchmark for referencing future ocean and ecosystem  
120 conditions. This study presents a valuable reference dataset for the upper slope of the northern  
121 Labrador Shelf against which future changes could be evaluated.

122 To obtain a better understanding of the environmental conditions and ecosystem functioning  
123 of high- and low-sponge-biomass sites on the upper slope of the northern Labrador Shelf, this  
124 study specifically aimed to examine: (i) differences in ocean dynamics and seawater  
125 properties,, (ii) the annual dynamics of near-bed environmental and hydrodynamic conditions,

126 and (iii) differences in organic matter flux and isotopic signatures for sponges and associated  
127 macrofauna. To this end, data on regional oceanography of the Northern Labrador shelf was  
128 collected from CTD casts, Argo float profiles, and surface drifter buoys. Bottom  
129 hydrodynamic- and environmental conditions were assessed using two year-long benthic  
130 lander deployments. Organic matter fluxes were measured with sediment traps, and benthic  
131 macrofauna was sampled by two rock dredge deployments. This study is the first to collect  
132 year-long hydrodynamic and environmental data simultaneously at a high- and a low-biomass  
133 sponge ground.

## 134 2 Material and methods

### 135 2.1 Oceanographic setting and the study area

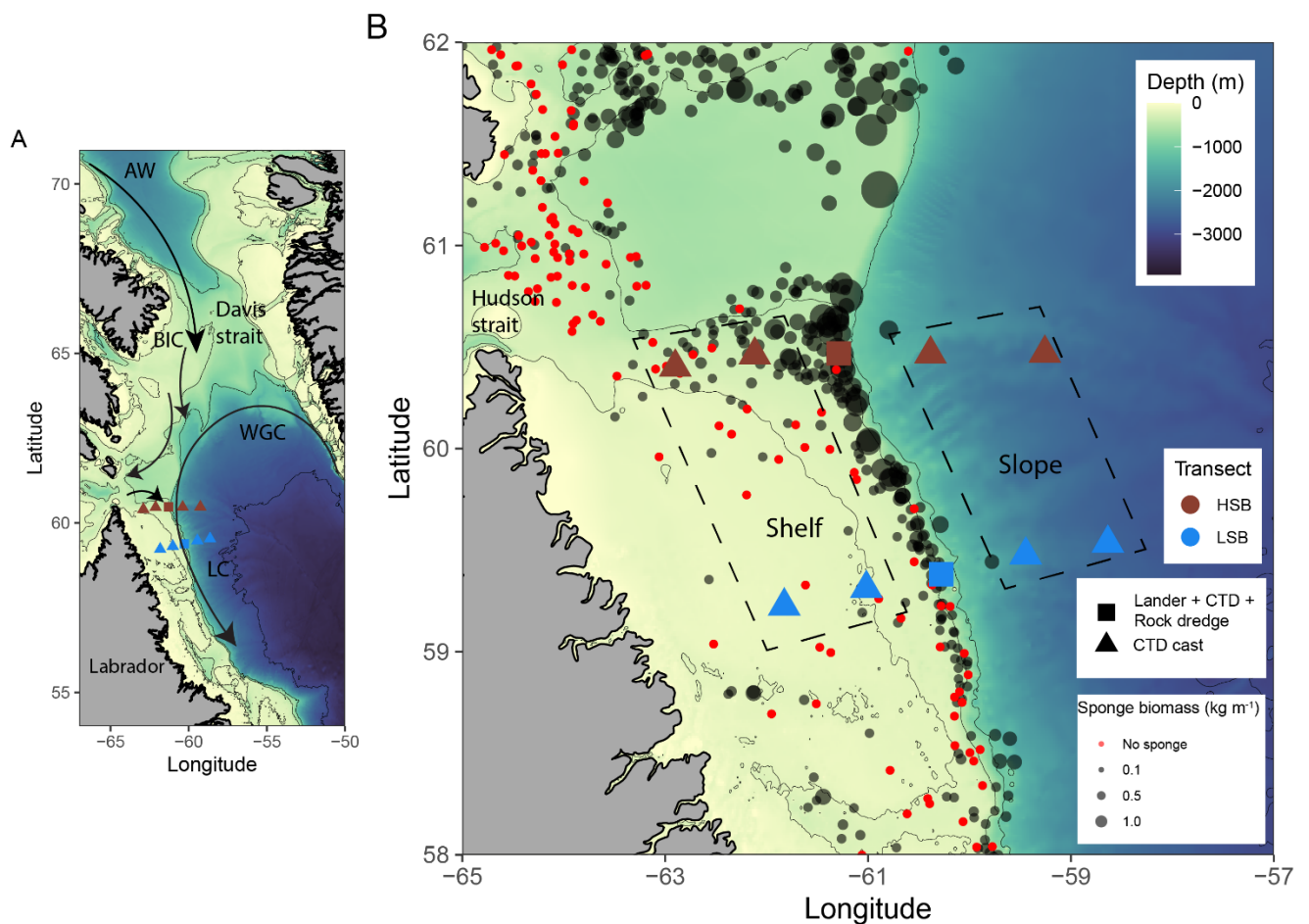
136 The study area comprises the northern Labrador Shelf and upper slope and extends from the  
137 south-eastern Hudson Strait outflow region to the base of the Labrador slope (Figure 1A). This  
138 region is known for intense mixing and water mass transformation (Dunbar, 1951; Kollmeyer  
139 et al., 1967; Griffiths et al., 1981; Drinkwater and Jones, 1987) and four distinct flow  
140 components can be identified (Figure 1A; Smith et al., 1937; Yashayaev, 2007; Straneo and  
141 Saucier, 2008; Curry et al., 2011, 2014): first, the cold and relatively fresh Arctic outflow,  
142 passing through the Davis Strait via the Baffin Island Current (BIC), enters the region from the  
143 north as Arctic Water (AW) and Baffin Bay Water (BBW; Sherwood et al., 2021); second, the  
144 West Greenland Current (WGC) approaches our study site from the northeast; third, Irminger  
145 Water (IW), a warmer and saltier water mass, can often be seen below the WGC, usually >150  
146 m depth; and fourth, Hudson Strait outflow water which enters the region from the west. The  
147 resulting aggregated boundary current joins the Labrador Current (LC) flowing southward  
148 along the Labrador Shelf/slope, effectively forming and maintaining a baroclinic transition  
149 between the less-saline shelf water and the more-saline deep-basin water (Yashayaev, 2007).

150 The northern Labrador Shelf hosts multiple sponge grounds with contrasting sponge  
151 community composition, density, and biomass (Kenchington et al., 2010; Dinn et al., 2020).  
152 We selected a high-sponge-biomass site (HSB; 410 m depth) in the north and a low-sponge-  
153 biomass site (LSB; 558 m depth) in the south of the study area (Table S1; Figure 1B),  
154 approximately 130 km apart.

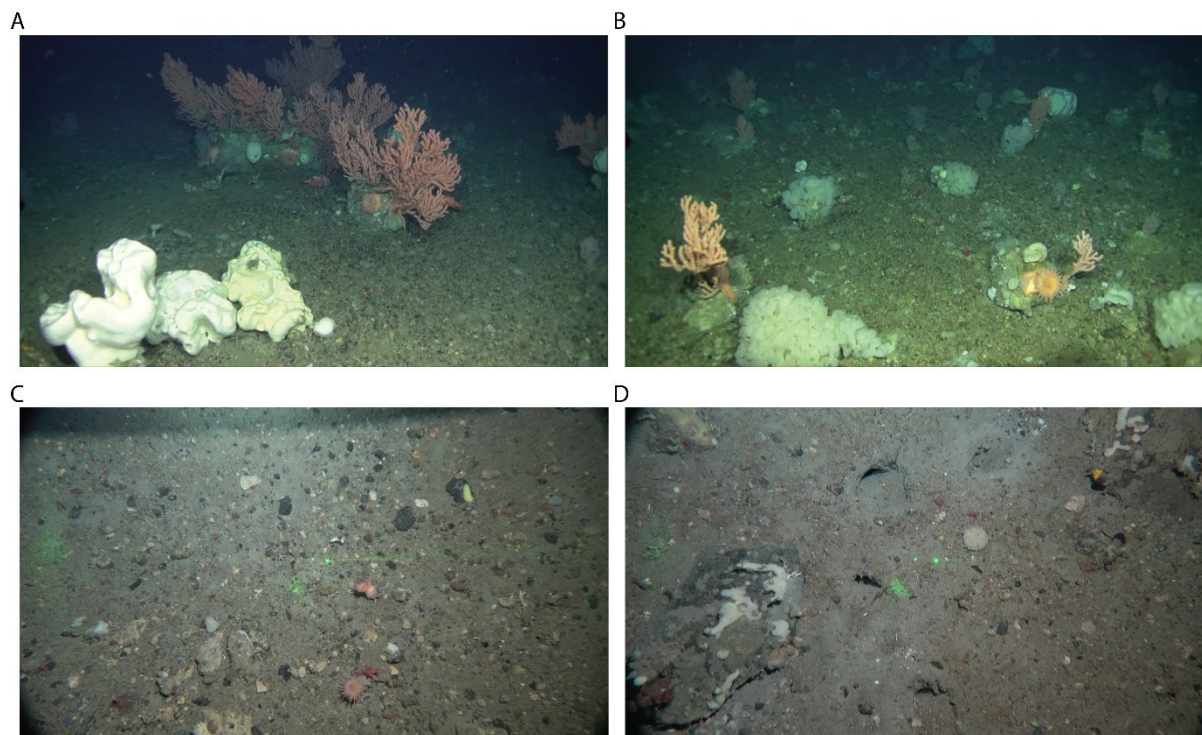
155 The substrate at the HSB lander location consisted mostly of pebbles, cobbles, and boulders  
156 (Figure 2 A & B; Kenchington et al., 2010; Dinn et al., 2020) and a visual assessment of the  
157 sediment type at the LSB lander location suggested the dominance of gravel (Coté et al., 2019).

158 The seafloor at the HSB lander was characterized by large-sized massive demosponges (e.g.  
 159 *Geodia* spp.), glass sponges (e.g. *Asconema* spp.), and large gorgonian corals (*Primnoa*  
 160 *resedaeformis*; Figure 2 A & B; Kenchington et al., 2010; Dinn et al., 2020). The benthic  
 161 community at LSB consisted mostly of small specimens of corals including *Anthomastus* sp.,  
 162 as well sponges as *Polymastia* sp, *Craniella* sp., *Axinella* sp, and possibly *Mycale* sp. (Figure  
 163 2 C & D; Coté et al., 2019).

164 The HSB lander was located on the shelf on a 2° slope and slope aspect was directed northwest  
 165 at 60°. The LSB lander was located on the upper slope, east of the shelf break, on a 7° slope  
 166 and aspect was directed southeast at 105° (Figure S1).



167  
 168 *Figure 1: Map of the study area with (A) the general circulation pattern (Curry et al., 2014). Cold Arctic Water (AW) flows*  
 169 *southward through the Davis Strait and continues as the surface-intensified Baffin Island Current. The warmer, more saline*  
 170 *West Greenland Slope Current (WGC) of North Atlantic origin largely follows the continental slope in the depth range 150 –*  
 171 *800 m and is deflected westward at approximately 64° N. Cold and fresh water leaves Hudson Strait and joins the BIC and*  
 172 *WGC to form the offshore branch of the Labrador Current (Straneo and Saucier, 2008). (B) Location of lander deployments*  
 173 *and CTD-casts, with sponge biomass (in kg m<sup>-1</sup>) based on Kenchington et al. (2010). Dotted line boxes indicate the shallow*  
 174 *shelf and deeper slope stations at both sites. HSB = high-sponge-biomass transect (red symbols), LSB = low-sponge-biomass*  
 175 *transect (blue symbols).*



177

178 *Figure 2: Images of benthic lander deployment sites, at the high-sponge-biomass lander site (HSB; A,B) and low-sponge-*  
 179 *biomass lander site (LSB; C, D). ROV image credits: ArcticNet/Canadian Scientific Submersible Facility (CSSF)/Department*  
 180 *of Fisheries and Oceans (DFO). Laser points in panel C & D are 6 cm apart.*

## 181 2.2 Sampling methodology

### 182 2.2.1 Near-bed lander deployment

183 Landers were deployed during research cruise Amundsen 2018 leg 2c (27 July 2018) and  
 184 retrieved during research cruise Amundsen 2019 leg 1b (1 & 2 July 2019). The landers were  
 185 each equipped with a 2 MHz single point measurement ADCP (upward-looking, Nortek  
 186 Aquadopp), a sediment trap, and a combined optical backscatter sensor (OBS) for turbidity and  
 187 fluorescence (Wetlabs ECO-FLNTU; Table S1).

188 The ADCPs collected data on pressure, water velocity, echo intensity (ABS; acoustic  
 189 backscatter signal), and water temperature at a 10 minute interval. Furthermore, the built-  
 190 in accelerometer and magnetometer in the ADCPs collected data on heading, pitch, and roll.  
 191 The ADCP was mounted 2 m above the bottom, the blanking distance was 1.14 m. Velocity  
 192 data were recorded in beam coordinates and transformed in MATLAB to ENU coordinates  
 193 (East, North, Up) after recovery using the transformation matrix provided by the manufacturer.  
 194 The 2 MHz ADCP have a lower particle size detection limit of 12  $\mu\text{m}$  in diameter, and a  
 195 maximum sensitivity for particles of 242  $\mu\text{m}$  diameter (Haalboom et al., 2021, 2023). The  
 196 combined optical backscatter sensor for turbidity and fluorescence was programmed to

197 measure every 10 minutes over the one-year period. The sediment trap (PPS 4/3, Technicap  
198 Inc.) with a surface area of 0.05 m<sup>2</sup> was equipped with twelve bottles for suspended particulate  
199 matter collection and with the aperture mounted at 2 m above the bottom. Collection started at  
200 15/08/2018 and lasted until the end of the deployment. Different time intervals of bottle rotation  
201 were set to increase sampling resolution during spring and summer months. The bottles rotated  
202 every 15 days from mid-August to mid-September 2018, every 30 days from mid-September  
203 to mid-November 2018, every 60 days from mid-November to mid-March 2019, then every 30  
204 days from mid-March to mid-May 2019, and every 15 days again from mid-May to mid-July  
205 2019. Prior to deployment, a 4% solution of formalin in brined seawater (40 psu) was added to  
206 each bottle.

### 207 2.2.2 Water column and benthic sampling

208 Conductivity-Temperature-Depth (CTD) casts were performed over two cross-shelf transects  
209 crossing the LSB and HSB lander sites (Coté et al., 2018; Figure 1B; Table S1). Two CTD  
210 casts were carried out on the continental shelf and three on the continental slope, where the  
211 third or middle cast was performed above each benthic lander deployment. The CTD-Rosette  
212 water column profiling and sampling package was equipped with a Seabird SBE 911*plus*  
213 system, which contained sensors to measure temperature (Seabird SBE 3*plus*), conductivity  
214 (Seabird SBE 4), pressure (Paroscientific Digiquartz®), dissolved oxygen (Seabird SBE 43),  
215 fluorescence (Seapoint), and a rosette water sampler with 12 Niskin bottles (12L each). CTD  
216 data were processed and “cleaned” with the *Sea-Bird SBE Data Processing* software (Guillot,  
217 2018). Water samples were taken from Niskin bottles at five depths (5 m, 50 m, mid-water,  
218 100 m above bottom, 10 m above bottom) for the determination of nutrients (NH<sub>4</sub><sup>+</sup>, NO<sub>2</sub><sup>-</sup> +  
219 NO<sub>3</sub><sup>-</sup>, PO<sub>4</sub><sup>3-</sup>, SiO<sub>2</sub>), and suspended particulate matter (SPM).

220 Benthic macrofauna samples for stable isotope analysis were collected at the two lander  
221 locations using a rock dredge on retrieval of the benthic landers (Coté et al., 2019; Table S3).  
222 A description of the species found at the two locations can be found in Coté et al. (2019). The  
223 rock dredge (7 mm mesh size) was deployed in “drift” mode at HSB, with a maximum speed  
224 of two knots (~4 km h<sup>-1</sup>) for 10-20 minutes, and “tow” mode at LSB, with the ship moving at  
225 one knot for 10 minutes. During CCGS Amundsen cruise 2019 leg1B, it was the first time that  
226 a rock dredge was operated on this research vessel, and therefore different operational modes  
227 of deployment were tested. At the LSB lander station, the rock dredge collected lots of soft  
228 sediment, and therefore “drift” mode was used. On deck, the dredge was rinsed, and the catch  
229 was subsampled and deposited in fish totes (64 L). The remaining material was sieved through  
230 a 2 mm mesh for analysis of invertebrates and fishes. The total catch was photographed and



231 preserved for species identification and quantification. Samples for stable isotopes were frozen  
232 (-20 °C) for further analysis at the Netherlands Institute for Sea Research (NIOZ).

### 233 2.2.3 Regional oceanography, sea-ice cover, and bottom temperature/salinity profiles

234 To explore the regional oceanography on the northern Labrador Shelf and upper slope,  
235 vertical Argo float profiles collected within the water depth range 330 - 2575 m (Figure S3)  
236 were extracted from the NOAA NODC World Ocean Dataset and profiling Argo float Global  
237 Argo Data Repository archives (Kieke and Yashayaev, 2015; Yashayaev and Loder, 2017)  
238 using the approach of Kenchington et al. (2017). We used Argo float profile data (N = 1472)  
239 collected between 2005 and 2022 to determine the seasonal variability in temperature and  
240 salinity along the northwest Labrador shelf break. Specifically, seawater properties of the  
241 corresponding water layers to the depth of the benthic landers (LSB = 350 – 450 m, HSB = 550  
242 – 650 m depth) were assessed. We report the mean temperature and salinity values binned per  
243 water layer. Argo float profiles below ~59° N latitude were considered LSB and above as HSB.  
244 Temperature and salinity values were detrended for interannual variability using an 8<sup>th</sup> degree  
245 least-square polynomial fit. Time-average surface currents were derived from trajectories of  
246 satellite-tracked surface drifting buoys (drifters) deployed within the NOAA Global Drifter  
247 Program during 2000–2020 (Centurioni et al., 2019). The trajectories were obtained from  
248 delayed-mode hourly data and real-time variable time-step data (Elipot et al., 2016, 2022). The  
249 drifter data were temporally interpolated into 15-min time intervals, binned hourly, and a low-  
250 pass filter was used to remove tidal and inertial oscillations. Then, the surface velocities were  
251 binned into a 1/3° grid. The drifter-derived surface currents reveal well-defined large-scale  
252 cyclonic circulation of the Labrador Sea, recirculation gyres, and mesoscale circulation  
253 features.

254 Sea-ice cover above the two benthic landers was extracted from weekly ice charts (Canadian  
255 Ice Service, 2022). Slope angle and aspect was estimated for each lander by taking the wider  
256 topography into account (Figure S1; Gille et al., 2004). Along-slope and across-slope bottom  
257 velocities are derived from the bottom current direction, slope aspect, and bottom horizontal  
258 current speed.

### 259 2.3 Laboratory analysis

260 Water column nutrient concentrations were analysed with a SEAL QuAATro analyser (Bran +  
261 Luebbe, Norderstedt, Germany) following standard colorimetric procedures. SPM samples  
262 were freeze-dried, weighed, and analysed for organic carbon content and total nitrogen content.

263 Sediment trap samples were filtered through a 1 mm sieve to remove large particles and  
264 swimmers, then split into five sub-samples using a McLane WSD-10 rotary splitter, rinsed with  
265 demineralized water to remove salts and formalin and subsequently freeze-dried and weighed  
266 (Newton et al., 1994; Mienis et al., 2012). Lipids were extracted and analysed following the  
267 method of Kiriakoulakis et al. (2004). Briefly, samples were spiked with internal standard  
268 ( $5\alpha(H)$ -cholestane), extracted by sonication in dichloromethane:methanol (9:1; x3). The  
269 solvent was removed and samples were first trans-methylated (Christie, 1982) and then treated  
270 with bis-trimethylsilyltrifluoroacetimide: trimethylsilane (99:1; 30-50  $\mu$ L; 60  $^{\circ}$ C; 1 h) prior to  
271 analysis by gas chromatography-mass spectrometry (GCMS). GCMS analyses were conducted  
272 using a GC Trace 1300 fitted with a split-splitless injector and column DB-5MS (60m x  
273 0.25mm (i.d.), with film thickness 0.1  $\mu$ m, non-polar stationary phase of 5% phenyl and 95%  
274 methyl silicone), using helium as a carrier gas (2 mL  $\text{min}^{-1}$ ). The GC oven was programmed  
275 after 1 minute to rise from 60 $^{\circ}$ C to 170 $^{\circ}$ C at 6 $^{\circ}$ C  $\text{min}^{-1}$ , then from 170 $^{\circ}$ C to 315 $^{\circ}$ C at 2.5  $^{\circ}$ C  
276  $\text{min}^{-1}$  and was then held at 315  $^{\circ}$ C for 15 min. The eluent from the GC was transferred directly  
277 *via* a transfer line (320  $^{\circ}$ C) to the electron impact source of a Thermoquest ISQMS single  
278 quadrupole mass spectrometer. Typical operating conditions were: ionisation potential 70 eV;  
279 source temperature 215 $^{\circ}$ C; trap current 300  $\mu$ A. Mass data were collected at a resolution of  
280 600, cycling every second from 50– 600 Daltons and were processed using Xcalibur software.

281 Compounds were identified either by comparison of their mass spectra and relative retention  
282 indices with those available in the literature and/or by comparison with authentic standards.  
283 Quantitative data were calculated by comparison of peak areas of the internal standard with  
284 those of the compounds of interest, using the total ion current (TIC) chromatogram. The  
285 relative response factors of the analytes were determined individually for 36 representative  
286 fatty acids and sterols using authentic standards. Response factors for analytes where standards  
287 were unavailable were assumed to be identical to those of available compounds of the same  
288 class.

289 Sponges and other benthic fauna collected using a rock dredge were subsampled on-board the  
290 CCGS Amundsen, as parts of the specimens' bodies were used in separate studies and parts for  
291 isotopic analysis in this study. In the laboratory, the collected fauna was freeze-dried and  
292 homogenized with a pestle mortar/ball mill. Subsamples (*ca.* 10 mg) were transferred into  
293 silver cups and acidified by addition of dilute HCL (2%, 5%, and 30%) to remove carbonates.  
294 Organic carbon and  $\delta^{13}\text{C}$  were analysed on acidified subsamples, and total nitrogen and  $\delta^{15}\text{N}$   
295 was determined on non-acidified subsamples using an Electron Analyser coupled to an Isotope  
296 Ratio Mass Spectrometer (Thermo flash EA 1112).  $\delta^{13}\text{C}$  and  $\delta^{15}\text{N}$  isotope values are expressed

297 in parts per thousand (‰) relative to the international standard Vienna Pee Dee Belemnite and  
298 atmospheric N<sub>2</sub> for carbon and nitrogen, respectively. Standard deviation of  $\delta^{13}\text{C}$  and  $\delta^{15}\text{N}$   
299 measurements was 0.15 ‰.

## 300 2.4 Data analysis

### 301 2.4.1 Data processing

302 The transformation of beam coordinates to ENU coordinates for the ADCP data was  
303 carried out in MATLAB (MATLAB, 2010), and other data processing steps used R. The  
304 following R packages are used during data analysis: oce, ggplot2, RColorBrewer, cowplot,  
305 knitr, reshape2, RNetCDF, readxl, lubridate, xts, ggalt, tibble, dplyr, clifro, mapdata, metR,  
306 patchwork, tibbletime, readr, viridis, biwavelet, signal, axtsa, terra, and raster (Wickham, 2007,  
307 2016; Grolemund and Wickham, 2011; Neuwirth, 2014; signal developers, 2014; Michna and  
308 Woods, 2019; Pedersen, 2019; R Core Team, 2019; Wickham and Bryan, 2019; Wilke, 2019;  
309 Kelley and Richards, 2020; Stoffer, 2020; Vaughan and Dancho, 2020; Xie, 2020; Lovelace et  
310 al., 2022). Statistics are presented as means  $\pm$  standard deviations.

### 311 2.4.2 Benthic lander analysis

312 Occasionally, pitch and roll data from the ADCP sensor at HSB were shifted for a small period  
313 of the deployment, implying the lander was occasionally moving slightly (Figure S3).  
314 Pitch/heading/roll was almost identical before and after these disturbances. Furthermore, the  
315 ADCPs correct for the pitch/roll/heading of the respective device when producing the raw beam  
316 data. Removing datapoints during disturbance did not change the outcome of any of the  
317 analyses, statistical tests, or descriptive statistics and therefore datapoints were retained in the  
318 HSB lander time series.

319 Chl-*a* concentration (in  $\mu\text{g L}^{-1}$ ) and turbidity (in Nephelometric Turbidity Unit; NTU) were  
320 calculated from ping counts as described in the manual of the manufacturer.

321 Spectral analyses of lander data based on a Fourier transformation (Bloomfield, 2004) were  
322 performed to examine recurring patterns or periodicity in the time-series data (e.g. Shumway  
323 et al., 2000; Bloomfield, 2004). Prior to these analyses, time series data were smoothed using  
324 modified lowpass Daniell filters (Bloomfield, 2004), to remove periodicities shorter than 3  
325 hours. The magnitude and direction of ADCP-recorded tidal currents were analysed with least-  
326 squares harmonic analysis.

328 Internal tides are generated by the barotropic tide interacting with sloping bottom topography  
329 and can have a profound influence on the thermohaline structure and local mixing processes.  
330 Internal tides are found at complex deep-sea topographic features such as continental shelves,  
331 ridges, seamounts and canyons (e.g., Cacchione et al., 2002). Internal tide – topography  
332 interactions can be classified by the slope parameter  $\alpha / c$  (St Laurent and Garrett, 2002;  
333 Cacchione et al., 2002). The internal wave slope  $c$  is calculated from  $c = \sqrt{\frac{\omega^2 - f^2}{N^2 - \omega^2}}$ , with tidal  
334 frequency  $\omega = 1.4053 \times 10^{-4} \text{ rad s}^{-1}$  (representing the dominant M2 tidal component) and local  
335 inertial frequency  $f \text{ (s}^{-1}\text{)}$ . The Brunt-Väisälä frequency  $N^2 \text{ (rad s}^{-2}\text{)}$  was calculated as the mean  
336 value ( $1.4228 \times 10^{-5} \text{ rad s}^{-2}$ ) from all CTD stations and depths below the deep pycnocline at  
337 250 m or from bottom values at shallower profiles. The topographic slope  $\alpha$  was calculated  
338 from the maximum depth gradients in latitude and longitude based on GEBCO\_2023 data  
339 (GEBCO Bathymetric Compilation Group, 2023). At critical or near-critical slopes ( $\alpha \approx c$ ), the  
340 internal tide is locally amplified and vertical mixing is intensified. At subcritical slopes ( $\alpha < c$ ),  
341 internal waves pass the topographic slope without being locally modified. At steeper  
342 supercritical slopes ( $\alpha > c$ ), internal waves are reflected into deeper waters.

343 Bottom currents and direction were compared to model derived barotropic tidal currents,  
344 retrieved from the Oregon State University (OSU) Tidal Inversion Software (OTIS; Egbert and  
345 Erofeeva, 2002).

## 346 3 Results

### 347 3.1 Seawater properties over the northern Labrador Shelf and upper slope

348 The CTD casts, performed in July 2018, revealed different seawater properties between the  
349 two transects (Figure 3; Figure S4). The surface water at the time of survey was relatively warm  
350 ( $2 - 6 \text{ }^\circ\text{C}$ ) and fresh (31.2 to 33.8 psu) showing an offshore increase in temperature and salinity.  
351 From the surface to the depth of 20-70 m, depending on the transect and location, temperature  
352 decreased to sub-zero or near-zero at the shelf locations, to  $3 \text{ }^\circ\text{C}$  at the slope locations, and then  
353 increased again to  $2.8 \text{ }^\circ\text{C}$  at 250 m depth on the shelf and to  $4.3 \text{ }^\circ\text{C}$  at 150 m on the slope. A  
354 cold intermediate layer was visible at all profiles between 50 – 150 m depth. Salinity increased  
355 nearly monotonically with depth up to the pycnocline across all stations. The stations at LSB  
356 were more saline overall than those at the matching water depths on the HSB transect.  
357 Buoyancy frequency showed peak values at the upper- and lower boundaries of the above  
358 described cold intermediate layer at both transects (Figure S4F).

359 The oxygen concentration was highest in the surface waters (0 – 50 m) on the shelf and  
360 decreased with depth at all CTD stations (Figure 4A). Although oxygen concentrations were  
361 still generally high, the bottom oxygen concentrations at the lander stations were, for both  
362 transects, relatively depleted compared to the deep water CTD transects at similar depths.  
363 Concentrations of nitrate, phosphate, and silicate were lowest above the thermocline and  
364 increased with depth, while ammonium and nitrite were higher near the surface than at depth  
365 (Figure 4B & C, Figure S5). The HSB station exhibited relatively high nitrate, phosphate, and  
366 silicate concentrations at 10 and 100 metres above bottom compared to similar depths at shelf  
367 and deep stations (Figure 4B & C, Figure S5). This increased nutrient concentration in the  
368 bottom waters was also apparent for silicate at the LSB station (Figure 4C), but not for nitrate  
369 (Figure 4B). Chl-*a* profiles showed a deep chlorophyll maximum along both transects at 50 m  
370 (Figure 4C), and near-zero concentrations in the bottom waters (Figure S4D). Particulate  
371 organic carbon (POC) concentrations were highest in the surface waters (8 – 38  $\mu\text{mol POC L}^{-1}$   
372 <sup>1</sup>) and on the shelf (Figure S6:). POC concentrations decreased with depth, and concentrations  
373 10 m above bottom were 1.48  $\mu\text{mol POC L}^{-1}$  at HSB, and 5.95  $\mu\text{mol POC L}^{-1}$  at LSB.

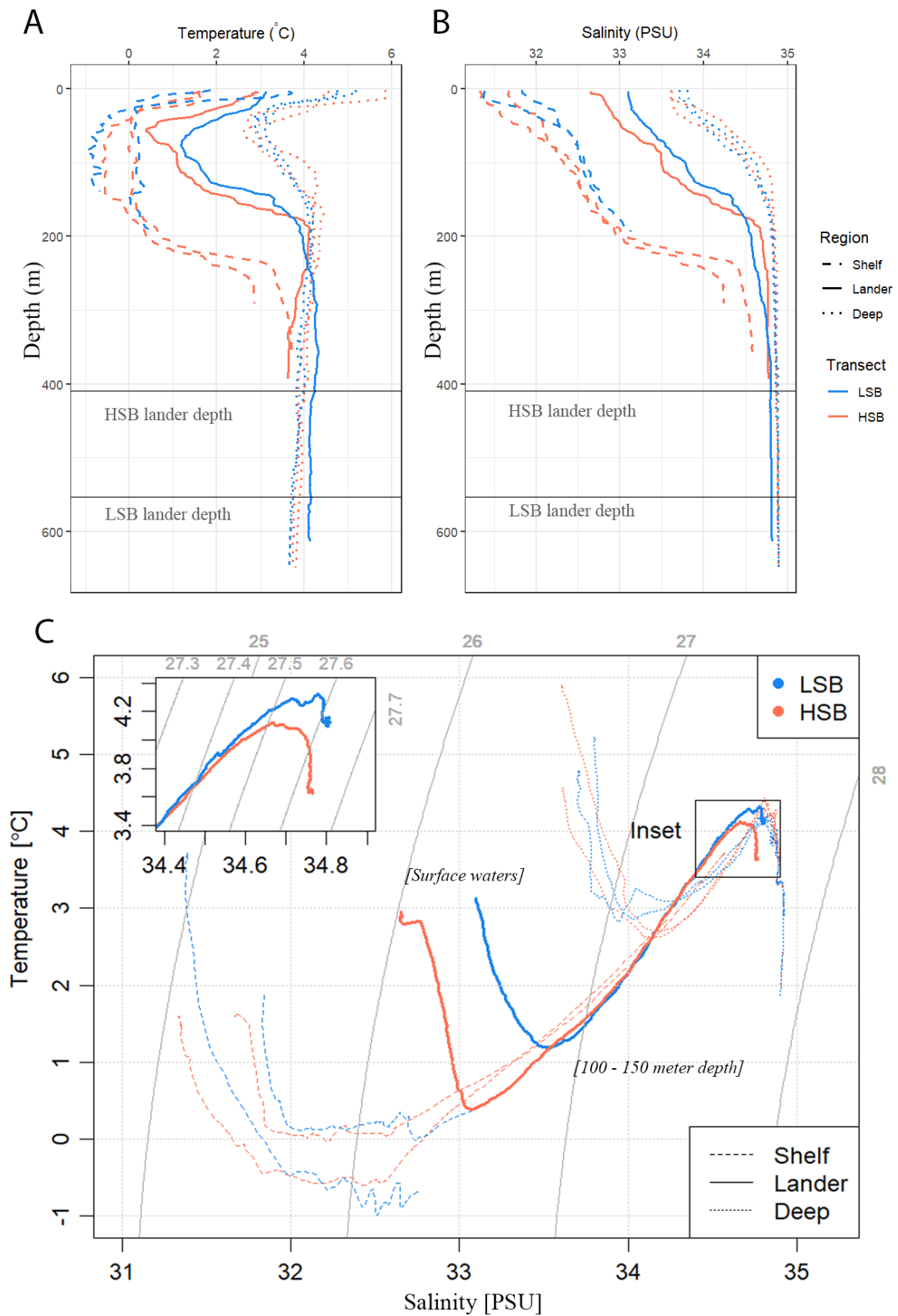
374 Surface water above the benthic lander locations was partly ice-covered from December to  
375 June, but both sites were located at the sea-ice border in the study area and ice cover was highly  
376 variable (Figure S11). Only during January ice-coverage was above 70% at both sites. Both  
377 locations showed a short ice-free period in February and March. During the spring bloom,  
378 between the end of March and early May, sea-ice coverage tended to be higher at HSB than at  
379 LSB (Figure S11D).

### 380 3.2 Regional oceanography and seasonal temperature patterns

381 Surface buoy drifter data showed that the HSB lander was located in an area where three  
382 (surface) currents converge (Figure 5A). Strong surface currents ( $>0.24 \text{ m s}^{-1}$  on average) carry  
383 water from the Hudson strait towards the Labrador shelf break, where this current meets two  
384 others that, respectively, flowed toward the HSB site from the north and northeast. On  
385 convergence, the currents followed the bathymetry of the Labrador shelf break or upper slope  
386 southwardly.

387 The seawater in the region of HSB was warmer and less saline than around LSB for both depth  
388 ranges within which the landers were deployed (Figure 5B & C; Figure S7). Bottom water  
389 temperature shows a steeper decrease in February at LSB compared to HSB (Figure 5C).  
390 Temperature and salinity show higher scatter at HSB than LSB throughout the season, but  
391 variability in temperature is highest at HSB in February/March (Figure 5B & C; Figure S7).

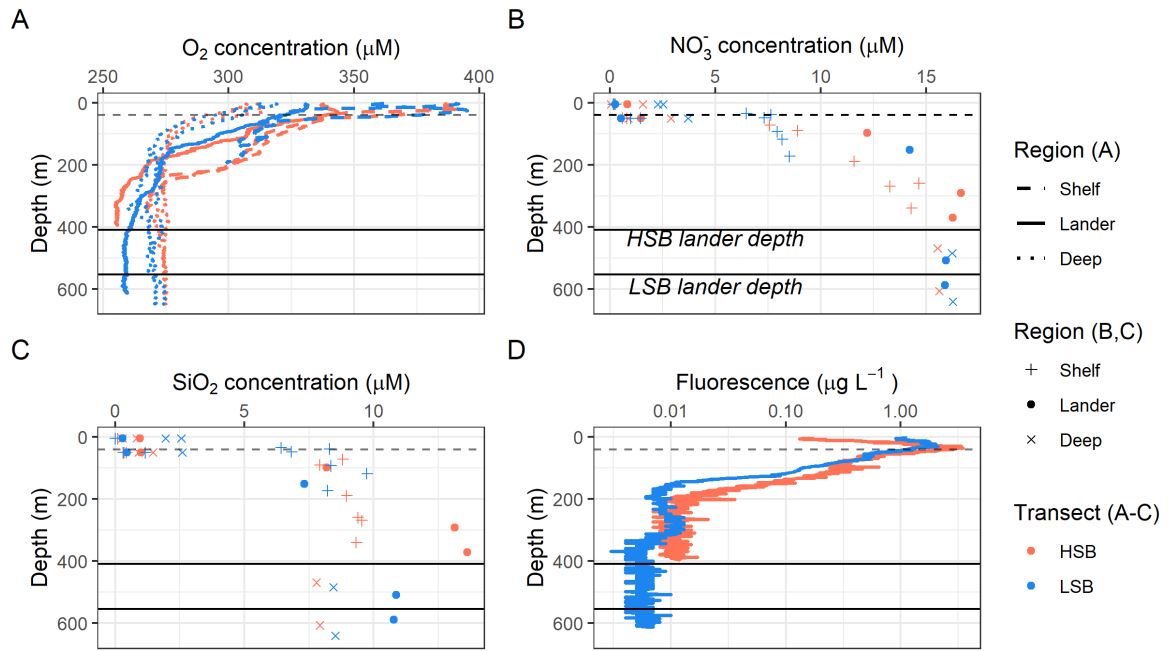




393

394 *Figure 3: Hydrographic conditions in the study area: (A) temperature, (B) salinity and (C) temperature – salinity (TS) plots*  
 395 *for the two transects. LSB = low-sponge-biomass, HSB = high-sponge-biomass. Depths of landers are indicated by the*  
 396 *horizontal grey lines in A and B. Temperature and salinity profiles in A and B only show top 600 m, while TS plots include the*  
 397 *entire water column. The thin grey lines in subplot C resemble isopycnals.*

398

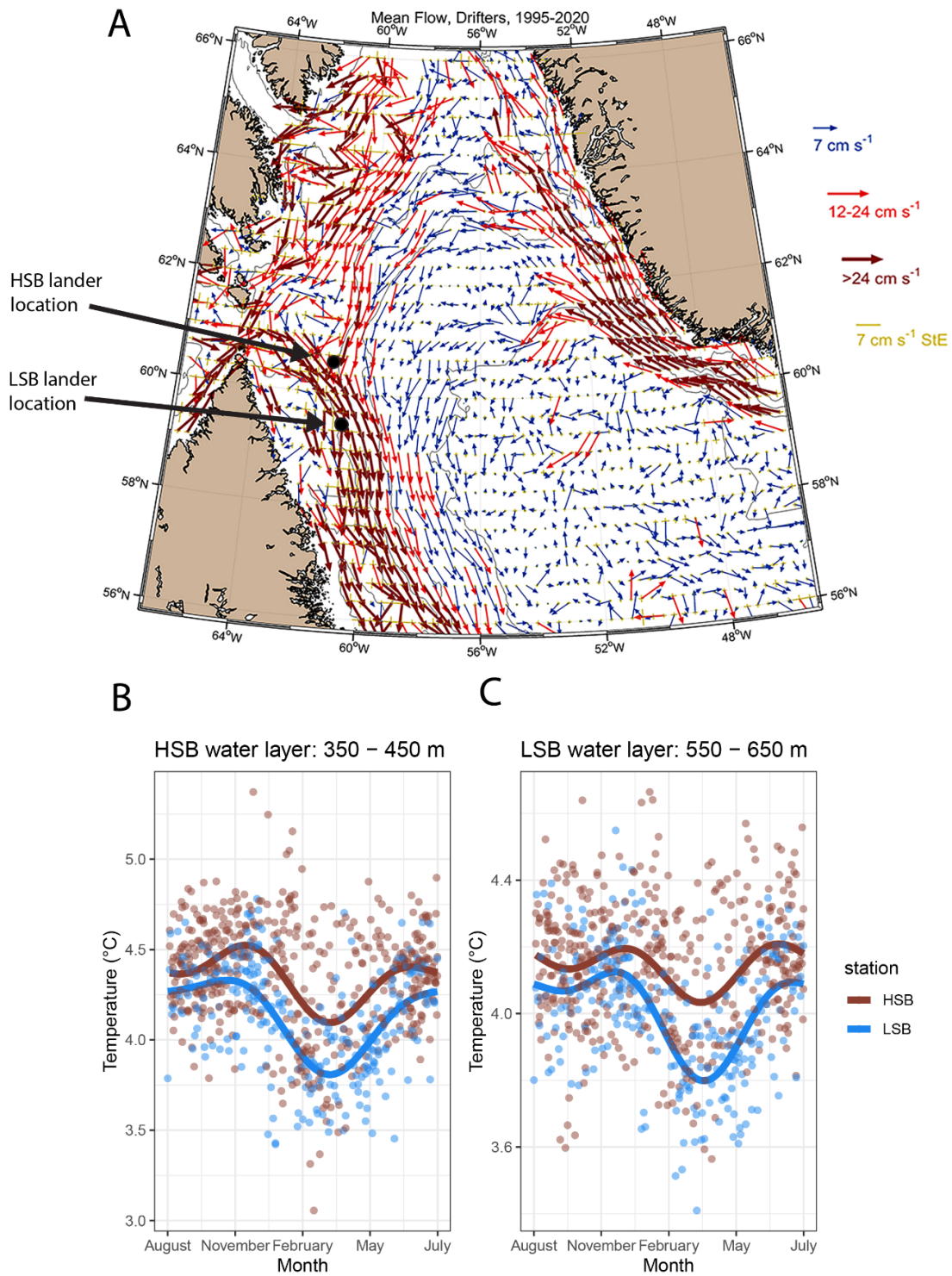


400

401 *Figure 4: Oxygen (A), nitrate (B), silicate (C) concentration profiles for the two transects, and D) fluorescence profiles for*  
 402 *the two CTD casts above the two lander locations. HSB = high-sponge-biomass site, LSB = low-sponge-biomass site. Black*  
 403 *lines indicate lander depths, dashed line indicates thermocline.*

404





405

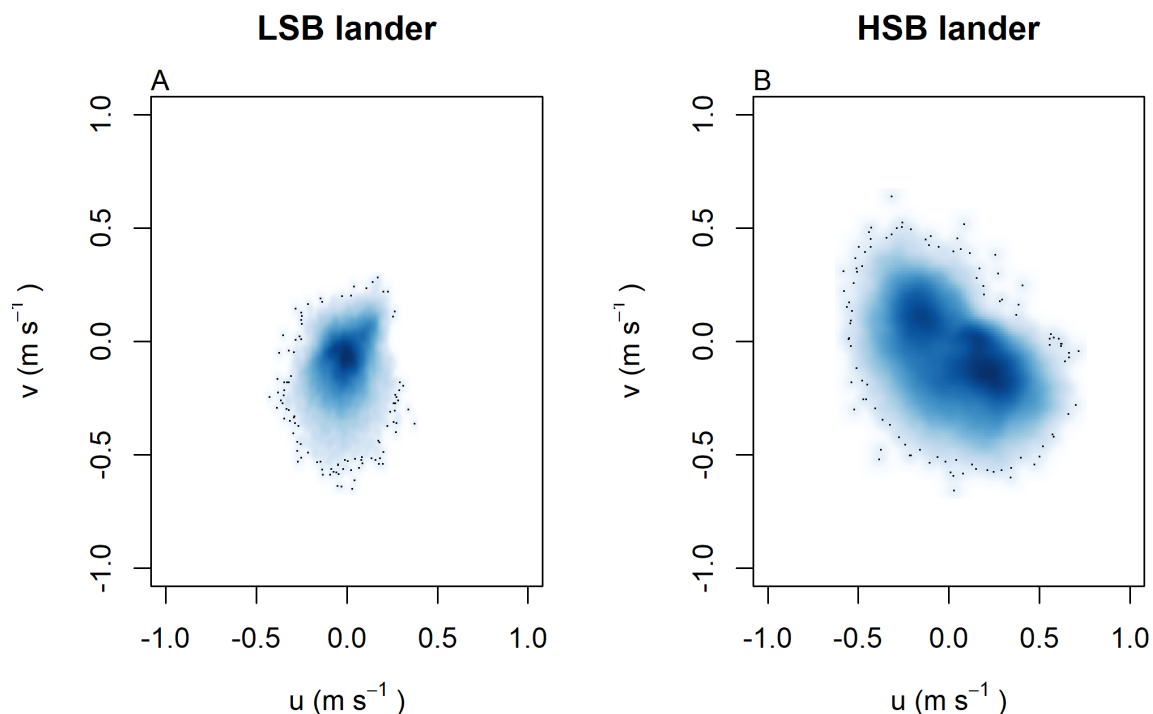
406 *Figure 5: A) general surface circulation pattern in the Labrador Sea based on drifter buoy data spanning from 1995 - 2020.*  
 407 *Arrows indicate mean direction, colours and length of arrow present the strength of the mean flow, the yellow arrows*  
 408 *present the standard error of the flow over 1995 – 2020. The lander locations are indicated by the coloured dots. B & C)*  
 409 *seasonal temperature, from Argo float profiles, of the water layer in which HSB/LSB lander was located. Dots represent*  
 410 *individual water-layer-binned temperature measurements vs. date of the year. The lines are a smoothed fit that show the*  
 411 *seasonal pattern.*

### 412 3.3 Year-long near-bottom measurements

#### 413 3.3.1 Near-bottom current velocities

414 In general, bottom current speeds were higher at the HSB compared to the LSB station (Table  
415 1; Figure 7). General current direction was south-easterly at HSB and south-south-westerly at  
416 LSB (Figure 6). Vertical velocity ( $w$ ) was on average upward and comparable between HSB  
417 and LSB, but the range in vertical velocity was higher at HSB ( $-0.35$  to  $0.32$   $\text{m s}^{-1}$ ) compared  
418 to LSB ( $-0.11$  to  $0.21$   $\text{m s}^{-1}$ ; Figure 7C). Bottom horizontal currents were twice as high at HSB  
419 than at the LSB (Table 1), and peak bottom horizontal current speeds were  $0.75$   $\text{m s}^{-1}$  (HSB)  
420 and  $0.65$   $\text{m s}^{-1}$  (LSB), with the third quantile at  $0.33$   $\text{m s}^{-1}$  (HSB) and  $0.18$   $\text{m s}^{-1}$  (LSB).

421



422

423 *Figure 6: horizontal current velocities at A) LSB lander and B) HSB lander.*

#### 424 3.4 Near-bottom environmental conditions

425 Bottom temperature was slightly warmer at HSB compared to LSB and increased at both sites  
426 ( $0.2 - 0.3$   $^{\circ}\text{C}$ ) during December and January (Figure 9). The benthic lander temperature aligned  
427 well with the seasonal temperature pattern retrieved by Argo float profiles (Figure 5 B & C).  
428 Turbidity measured by ABS was similar for the two stations (Table 1; Figure 9 B) and showed  
429 higher values in winter months. Chl-*a* remained low from October to February/March values  
430 started to increase for both landers (Figure 9 C). Bottom chl-*a* concentrations started to increase

431 after short ice-free period mid February and mid March Figure 9C; Figure S11D). The HSB  
 432 station showed highest chl-*a* concentrations from mid-March to the end of May, while at the  
 433 LSB station increased concentrations were observed from mid-March to early May.

434 Turbidity measured by OBS was elevated at HSB from February to April, and at LSB from  
 435 December to January. The higher variability in chl-*a* and turbidity at the LSB site over the year  
 436 (Table 1) was caused by several peaks in chl-*a* and turbidity that were an order of magnitude  
 437 higher than average values (Figure S8).

438 During several periods in the year-long time-series, turbidity measured by the ABS increased  
 439 at the turning of the tide and at high south-easterly current velocities at HSB (see e.g. Figure  
 440 10F). Strong along slope (southerly) bottom currents increased ABS turbidity and OBS  
 441 turbidity at LSB (Figure 10F). Cross-and along slope water transport influenced bottom  
 442 temperature. At the HSB lander, for example, in the first week of September, temperature  
 443 decreased when the current was directed northwest and increased when the current was directed  
 444 southeast (Figure 10 A-E).

445

446 *Table 1: Benthic lander mean and standard deviations over the year-long deployment period. Values are given as mean ±*  
 447 *standard deviation. HSB = high-sponge-biomass lander, LSB = low-sponge-biomass lander. ABS = acoustic backscatter*  
 448 *signal. OBS = optical backscatter signal*

<b>Variable</b>	<b>HSB</b>	<b>LSB</b>
<i>u</i> (eastward velocity; m s <sup>-1</sup> )	0.05 ± 0.22	-0.01 ± 0.09
<i>v</i> (northward velocity; m s <sup>-1</sup> )	-0.07 ± 0.16	-0.09 ± 0.11
<i>w</i> (vertical velocity; m s <sup>-1</sup> )	0.03 ± 0.05	0.02 ± 0.03
Bottom current speed (m s <sup>-1</sup> )	0.26 ± 0.14	0.14 ± 0.08
Temperature (°C)	3.70 ± 0.17	3.58 ± 0.17
Daily temperature variability (Δ°C d <sup>-1</sup> )	0.25 ± 0.16	0.17 ± 0.1
Turbidity by ABS (counts)	98.1 ± 9.8	96.6 ± 11.0
Chl- <i>a</i> concentration (μg L <sup>-1</sup> )	0.11 ± 0.03	0.08 ± 0.10
Turbidity by OBS (NTU)	0.20 ± 0.10	0.21 ± 0.27
Across slope velocity (m s <sup>-1</sup> )	0.01 ± 0.13	-0.01 ± 0.01
Along slope velocity (m s <sup>-1</sup> )	-0.08 ± 0.23	-0.09 ± 0.11

449

### 450 3.4.1 Tidal analysis of bottom currents and environmental conditions

451 Bottom current speeds showed semi-diurnal and spring-neap tidal patterns, with a peak every  
 452 fortnight for both sites (Figure 7 C; Figure 8 B; Figure 10). The major axes of the semidiurnal  
 453 tidal ellipses were directed in a northwest-southeast direction at HSB and a north-south  
 454 direction at LSB (Figure 7D). The tidal analysis presented in Table 2 and Figure 8 shows  
 455 notable differences in tidal characteristics between the LSB and HSB lander locations. While  
 456 semidiurnal tidal harmonics predominate at both locations, the semi-major axis at the HSB site

457 is approximately four times larger than the corresponding value at the LSB site. Moreover,  
 458 there is a significant discrepancy between the modelled and observed main semidiurnal tidal  
 459 harmonics (M2) at the HSB site, particularly in terms of magnitude and tidal ellipse  
 460 eccentricity. This indicates that the dominant barotropic semidiurnal tide (M2) is altered at the  
 461 HSB site, leading to strongly rectified near-bottom baroclinic tidal currents. There are no  
 462 substantial differences between the modelled (barotropic) and observed S2 tidal currents,  
 463 except for the tidal ellipse eccentricity at the LB site, likely due to the depth difference between  
 464 the model and observations at this location. Furthermore, spectral density for the HSB bottom  
 465 current components also peaked at shorter frequencies (3-6 h) and at the fourteen-day spring-  
 466 neap tide (Figure 8B). In addition, a superimposed seasonal pattern can be seen at both sites,  
 467 where the bottom current speed gradually increased from July 2018 to March 2019 and  
 468 decreased again from March 2019 to July 2019.

469 *Table 2: Tidal analysis of velocity time series from the HSB and LSB lander sites based on ADCP measurements and OTIS*  
 470 *tidal model analysis.  $A_{maj}$  and  $a_{min}$  are the semi-major and semi-minor axes of the tidal ellipse and  $\epsilon$  is the eccentricity*  
 471 *( $a_{min}/a_{maj}$ ). OTIS model data represent the barotropic tidal signal, whereas ADCP data show the near-bottom tidal*  
 472 *characteristics.*

LSB – lander data	$a_{maj}$ (cm s <sup>-1</sup> )	$a_{min}$ (cm s <sup>-1</sup> )	$\epsilon$ ( $a_{min}/a_{maj}$ )	Water depth (m)
M2	5.73	2.17	0.38	558
S2	1.74	0.51	0.30	
K1	0.65	0.05	0.08	
O1	0.10	0.03	0.25	
HSB – lander data				
M2	27.77	7.26	0.26	410
S2	9.61	2.88	0.30	
K1	0.88	0.44	0.51	
O1	0.36	0.21	0.58	
LSB – OTIS tidal model				
M2	6.08	1.48	0.24	629
S2	1.58	0.57	0.36	
K1	0.49	0.06	0.11	
O1	0.18	0.01	0.04	
HSB – OTIS tidal model				
M2	40.67	19.23	0.47	425
S2	10.45	4.47	0.43	
K1	1.35	0.53	0.39	
O1	0.80	0.38	0.48	

473

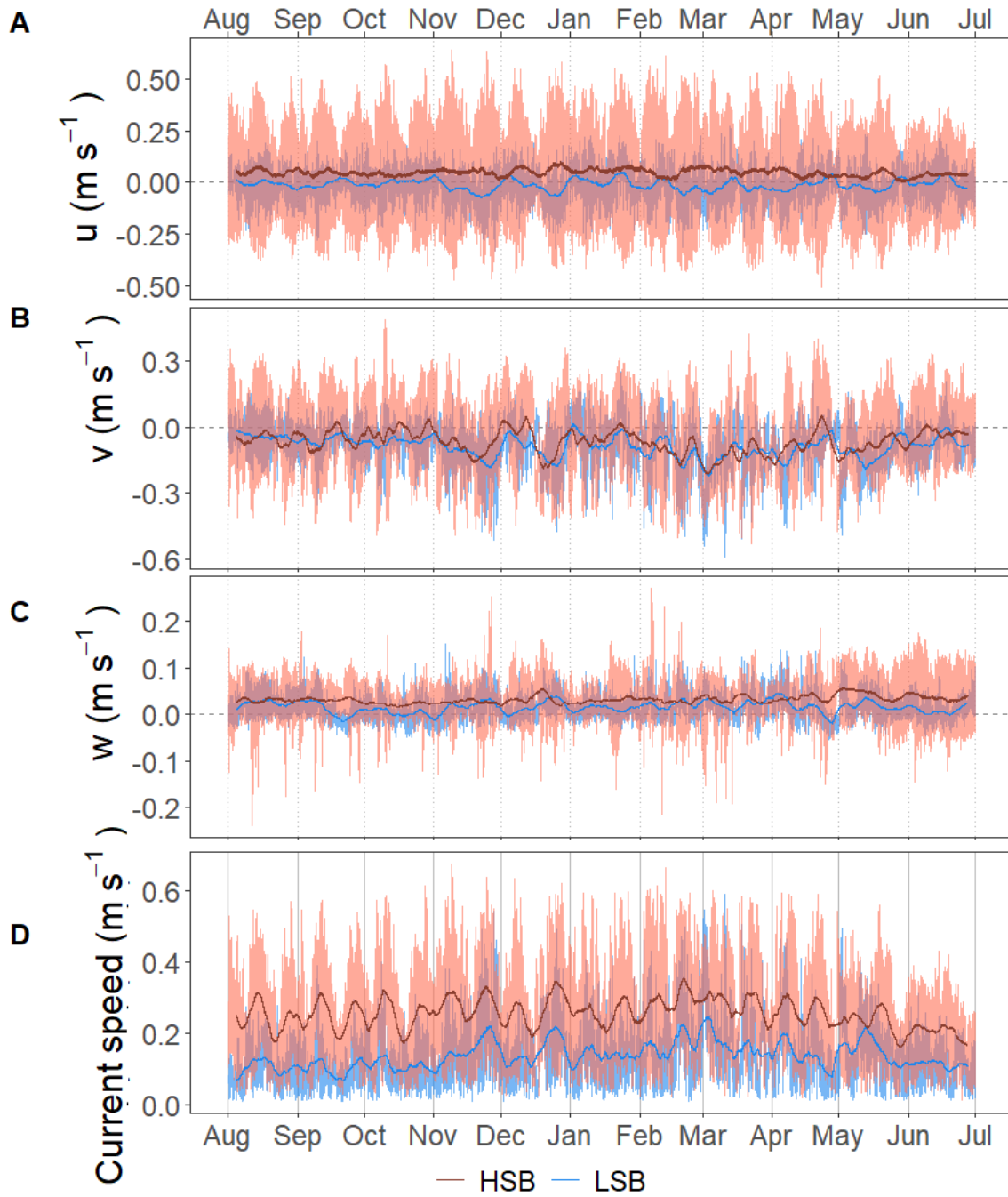
474 Temperature, chl-*a*, turbidity measured by ABS and OBS, all showed a reoccurring tidal peak,  
 475 with higher peaks in spectral density for the semidiurnal periodicity at HSB than at LSB (Figure  
 476 8C). Daily temperature fluctuations were higher at HSB than at LSB. During the spring bloom,  
 477 bottom chl-*a* concentration increased during strong south-easterly current velocities at HSB  
 478 (Figure S10) and showed a periodic reoccurring peak (Figure S11A).

479

480

481

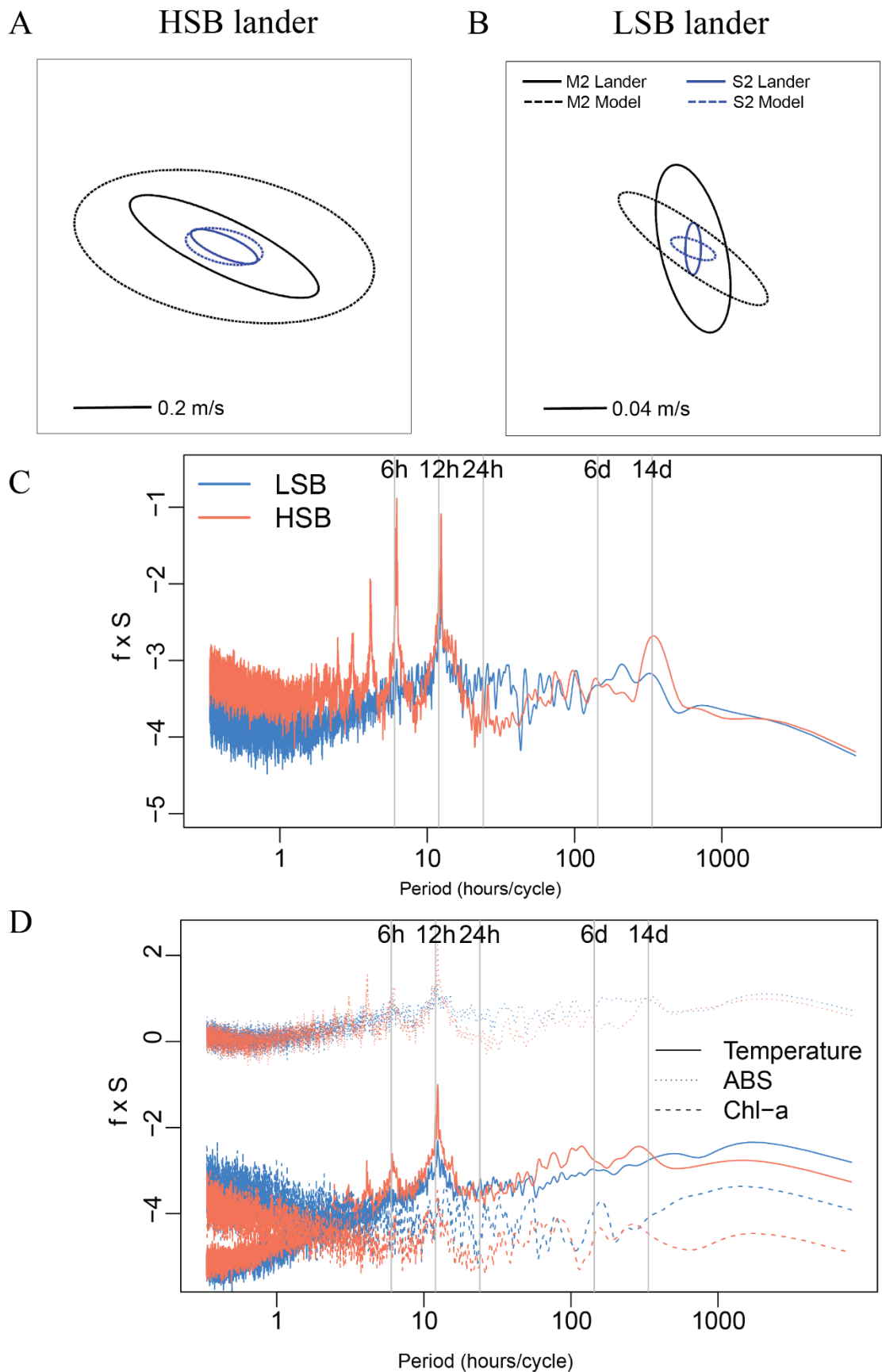
482



483

484 *Figure 7: Time series of the flow velocities with eastward  $u$  velocity (A), northward  $v$  velocity (B), vertical  $w$  velocity (C),*  
485 *and bottom current speed (D). Plots show the hourly averaged data as transparent lines and the seven-day rolling means as*  
486 *solid lines.*

487



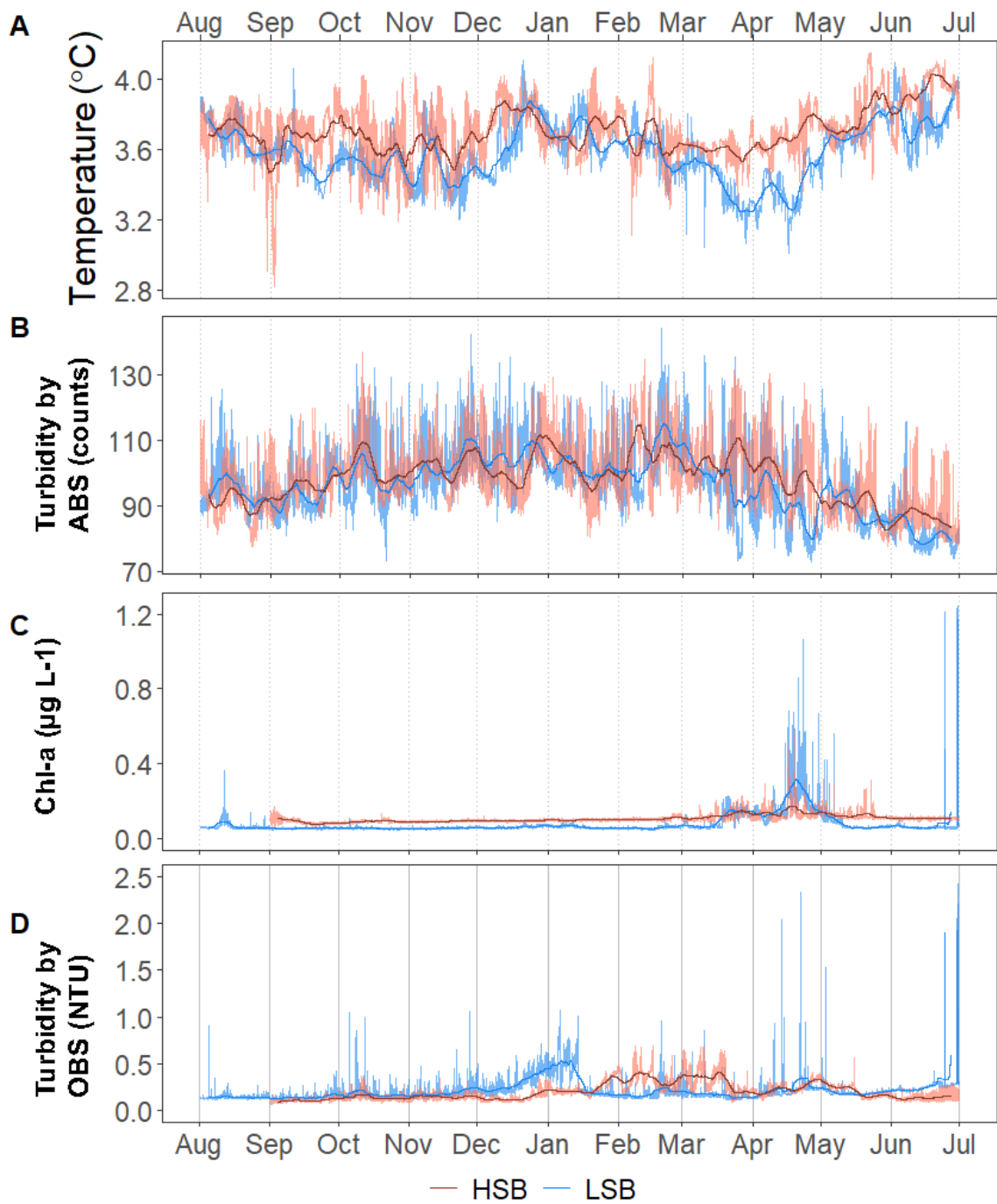
488

489 *Figure 8: A & B) Tidal current ellipses at the HSB and LSB lander sites for the two dominant semidiurnal tidal harmonics*

490 *M2 (black lines) and S2 (blue lines) derived from the unfiltered ADCP velocities (solid lines) and the OTIS inverse tidal*

491 *model (dashed lines) respectively. Variance preserving spectra for C) bottom current speed, (D) temperature, turbidity by*

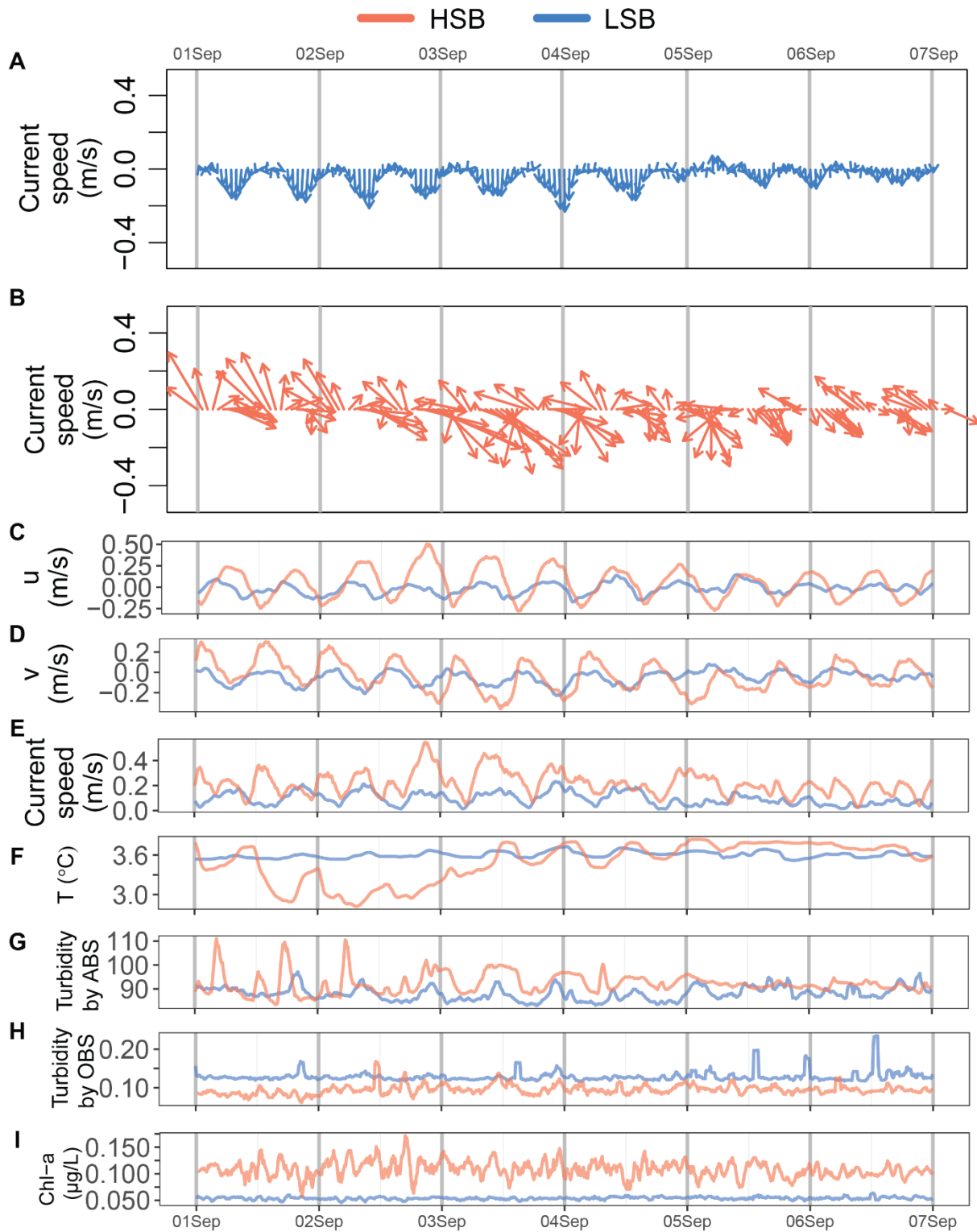
492 *acoustic backscatter signal (ABS), and chl-a.*



493

494 *Figure 9: Time series for temperature in °C (A), Turbidity by acoustic backscatter (ABS; in counts) (B), Chl-a concentration*  
 495 *in  $\mu\text{g L}^{-1}$  (C), and turbidity by optical backscatter (OBS) in NTU (D). Plots C and D are limited on the y-axis to  $1.25 \mu\text{g L}^{-1}$*   
 496 *and 2.5 NTU, respectively, for clarity. Chl-a and turbidity by OBS data without the Y-axis cut-offs are plotted in Figure S10.*

497



498

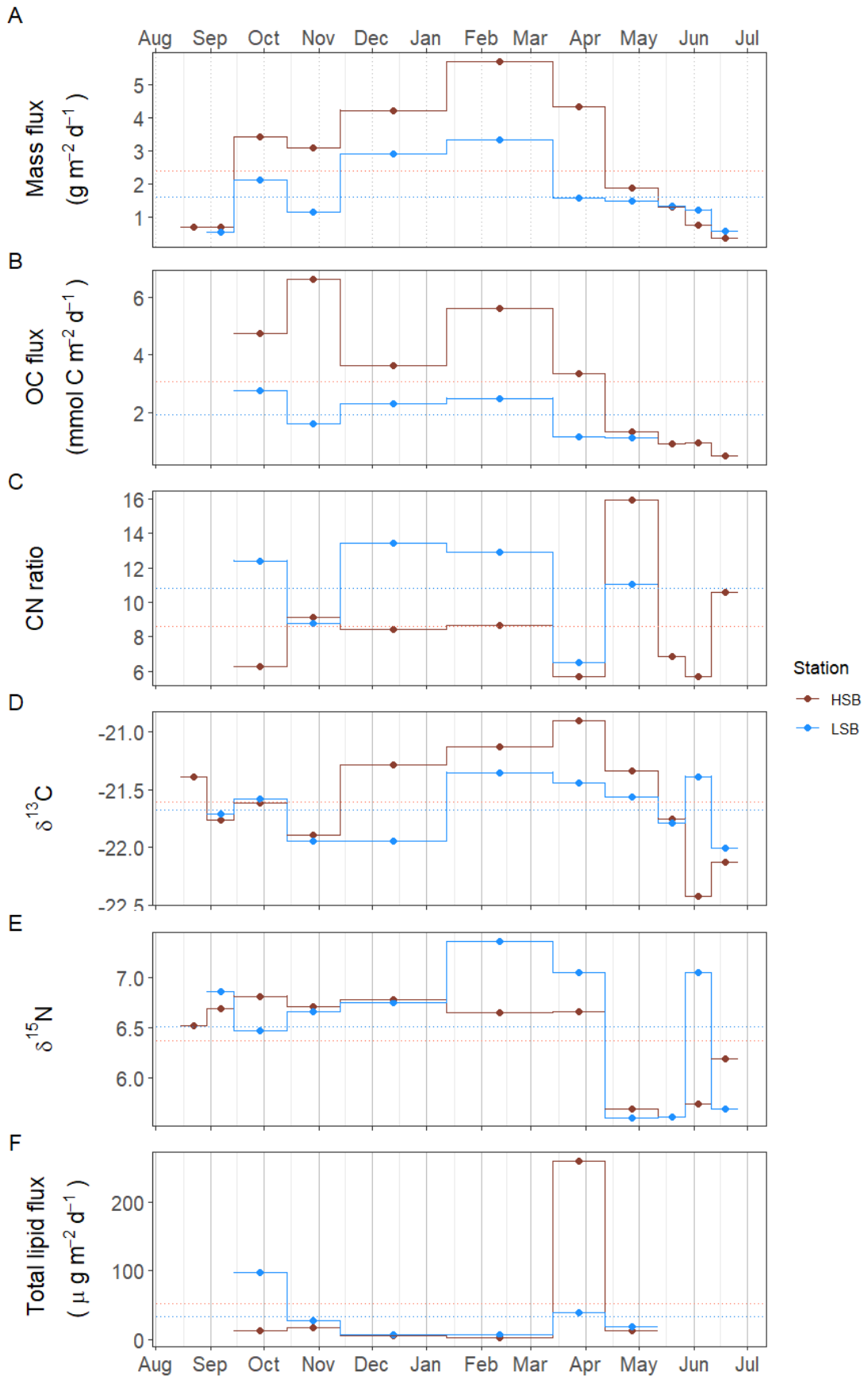
499 *Figure 10: Expanded detail for the first week of September for the current direction at LSB (A), current direction at HSB (B),*  
 500 *eastward velocity (C), northward velocity v (D), bottom current speed (E), temperature (F), turbidity by acoustic backscatter*  
 501 *(ABS; G), turbidity (H), and chl-a concentration (I).*

### 502 3.5 Mass deposition and organic carbon fluxes

503 The average mass fluxes were higher at HSB ( $2.46 \pm 1.76 \text{ g m}^{-2} \text{ day}^{-1}$ ) than at LSB ( $1.43 \pm 0.93$   
 504  $\text{g m}^{-2} \text{ day}^{-1}$ ), with highest fluxes in winter (October to April) at both sites, which corresponds  
 505 well with the superimposed seasonal patterns seen in ABS turbidity and bottom current speed.  
 506 Average POC fluxes were higher at HSB ( $3.07 \pm 1.91 \text{ mmol C m}^{-2} \text{ d}^{-1}$ ) than at LSB ( $1.91 \pm$



507 0.71 mmol C m<sup>-2</sup> d<sup>-1</sup>). Organic carbon content at HSB was highest in autumn/summer months  
508 (~2 %) and highest at LSB in autumn (2-4%; data not shown). Average C:N ratios were lower  
509 at HSB (8.6 ± 3.2) than at LSB (10.8 ± 2.7) and were higher in winter and also in May 2018  
510 (Figure 11C). The δ<sup>13</sup>C ratios of trapped material were higher in winter at HSB compared to  
511 LSB, and were higher in summer at LSB than at HSB (Figure 11D). The δ<sup>15</sup>N of trapped  
512 material was comparable between sites, although slightly higher at LSB. Winter δ<sup>15</sup>N values  
513 were highest compared to the rest of the year for both landers (Figure 11E). The lipid flux was  
514 slightly higher at LSB, with low values in winter and peak values during the spring bloom  
515 (Figure 11F). Unsaturated alcohols comprised the largest fraction of lipids at LSB, especially  
516 in autumn and winter (Figure S12B). Peak lipid flux in April consisted of 25% polyunsaturated  
517 fatty acids (PUFAs) at HSB (Figure S12C). Sterols made up the largest fraction of total lipids  
518 at HSB and LSB in May (Figure S12D). The sterol fraction was lower in spring at both sites.  
519 Swimmers were found in the sediment trap bottles, especially in the autumn months at LSB.  
520 These consisted mostly of copepods (e.g., *Calanus* sp.), mysids (e.g., *Boreomysis* sp.),  
521 amphipods (e.g., Eusiridae) and chaetognaths (i.e., arrow worms). Numbers of trapped  
522 swimmers were lowest during winter at both sites. In addition, several large sponge spicules  
523 were found in the bottles at HSB, but not at LSB.



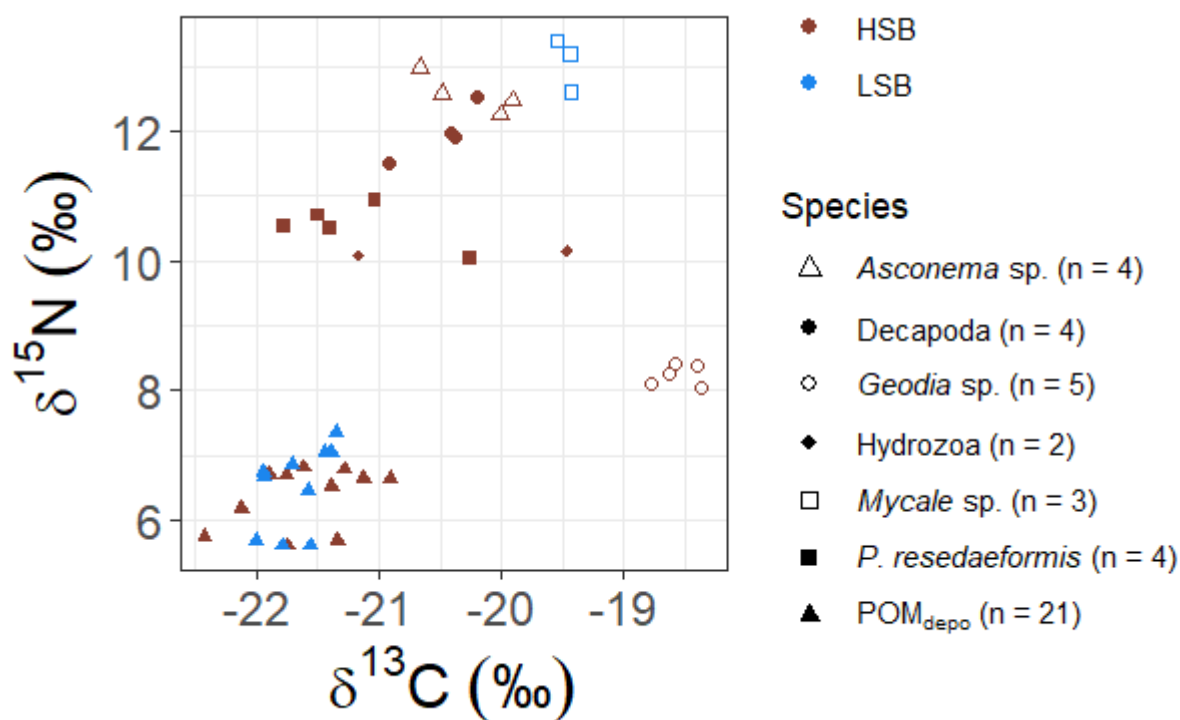
524

525 *Figure 11: Sediment trap content from the two benthic landers. HSB = high-sponge-biomass lander, LSB = low-sponge-*  
 526 *biomass lander. A) mass flux in  $\text{g m}^{-2} \text{d}^{-1}$ , B) organic carbon flux in  $\text{mmol C m}^{-2} \text{d}^{-1}$ , C) molar C:N ratio of trapped material,*  
 527 *D)  $\delta^{13}\text{C}$  of trapped material, E)  $\delta^{15}\text{N}$  of trapped material, F) total lipid flux in  $\mu\text{g m}^{-2} \text{d}^{-1}$ .*

528 3.6  $\delta^{13}\text{C}$  and  $\delta^{15}\text{N}$  isotopic ratios of benthic fauna and trapped material

529 The massive sponge *Geodia* spp. sampled at HSB showed a distinct isotopic signature  
530 compared to the other benthic organisms, with a relatively enriched  $\delta^{13}\text{C}$  ( $-18.55 \pm 0.17 \text{ ‰}$ )  
531 and a low  $\delta^{15}\text{N}$  ( $8.24 \pm 0.16 \text{ ‰}$ ; Figure 12). The gorgonian coral *Primnoa resedaeformis* had  
532  $\delta^{13}\text{C}$  of  $-21.19 \pm 0.59 \text{ ‰}$  and  $\delta^{15}\text{N}$  of  $10.54 \pm 0.33 \text{ ‰}$ . Compared to *P. resedaeformis*, Decapoda  
533 sp. showed slightly enriched  $\delta^{13}\text{C}$  ( $-20.48 \pm 0.31 \text{ ‰}$ ), and  $\delta^{15}\text{N}$  ( $11.97 \pm 0.43 \text{ ‰}$ ) values. The  
534 glass sponge *Asconema* sp., sampled at HSB, also had relatively enriched isotopic values ( $\delta^{13}\text{C}$ :  
535  $-20.27 \pm 0.36 \text{ ‰}$ , and  $\delta^{15}\text{N}$ :  $12.57 \pm 0.31 \text{ ‰}$ ) while the sponge *Mycale* sp., sampled at LSB,  
536 had a high  $\delta^{15}\text{N}$  isotopic ratio ( $13.05 \pm 0.41 \text{ ‰}$ ), and a  $\delta^{13}\text{C}$  ratio of  $-19.47 \pm 0.06 \text{ ‰}$ . Sediment  
537 trap samples had the lowest  $\delta^{15}\text{N}$  and  $\delta^{13}\text{C}$  isotopic ratios, with only small differences between  
538 HSB and LSB (Figure 11 D & E; Figure 12).

539



540

541 Figure 12: Carbon and nitrogen stable isotopes plots of megafauna and sediment trap samples. HSB = high-sponge-  
542 biomass, LSB = low-sponge-biomass.

543 4 Discussion

544 Hydrodynamic- and environmental conditions were compared at two contrasting high- and  
545 low-sponge-biomass sites along the northern Labrador shelf break. The aim was to compare  
546 differences between the two sites in terms of (i) seawater properties and regional hydrography  
547 (section 4.1, 4.2), (ii) bottom currents and environmental conditions, including seasonal

548 variations over the course of a year (section 4.3, 4.4), and (iii) benthic-pelagic coupling, organic  
549 matter supply and isotopic signatures of benthic macrofauna (sections 4.6, 4.6, and 4.7).

#### 550 4.1 Regional oceanography on the northern Labrador Shelf and Slope

551 The northern Labrador Shelf and Labrador Slope are known to be subject to strong tidal forcing  
552 which causes vertical mixing, high bottom current speeds (Griffiths et al., 1981; Drinkwater  
553 and Jones, 1987), and reduced stratification compared to the more northerly Baffin Island Shelf  
554 (Lazier 1982; Sutcliffe et al. 1983; Drinkwater and Harding 2001). The results of our drifter  
555 analysis confirm that around the HSB area three currents converge: the Hudson Strait Outflow,  
556 the Baffin Intermediate Current, and the West Greenland Current (Figure 5A; Smith et al.,  
557 1937; Yashayaev, 2007; Straneo and Saucier, 2008; Curry et al., 2011, 2014). These three  
558 currents transport, respectively, Hudson Strait Outflow Water, Arctic Water and/or Baffin Bay  
559 (intermediate) Water, and Irminger Water towards the northern Labrador Shelf and upper  
560 slope. Our CTD transects show the characteristics of these water masses, and are similar to  
561 earlier observations (Petrie et al., 1988; Fissel and Lemon, 1991; Drinkwater and Harding,  
562 2001). The warmer and saltier water at HSB ( $\Theta \sim 4.5$  °C and  $S \sim 34.9$ ) compared to LSB is  
563 likely caused by Irminger Water (Figure 5 B & C), which follows the Labrador slope in  
564 cyclonic direction beneath the cold water of the West Greenland Current and above the upper  
565 slope (Lazier et al., 2002). Our findings concur with previous work which showed that Irminger  
566 Water is gradually cooled while moving southward by mixing with the Baffin Island Current  
567 (Cuny et al., 2002). However, the Argo float temperature profiles indicate that the area around  
568 HSB might play an important role in transforming Irminger Water. For example, the 350-450  
569 m depth layer in the HSB area regularly showed presence of Irminger Water ( $>4.5$  °C), while  
570 it was only sporadically measured at LSB (Figure 5B). Irminger Water might therefore be  
571 cooled and freshened in the area around HSB due to convergence and consequently mixing  
572 occurs with the Hudson Outflow and Baffin Island Current. Our results support earlier findings  
573 that identified a connection between the Hudson Strait outflow strength and the southern  
574 Labrador Shelf water based on salinity measurements (Sutcliffe et al., 1983; Myers et al.,  
575 1990).

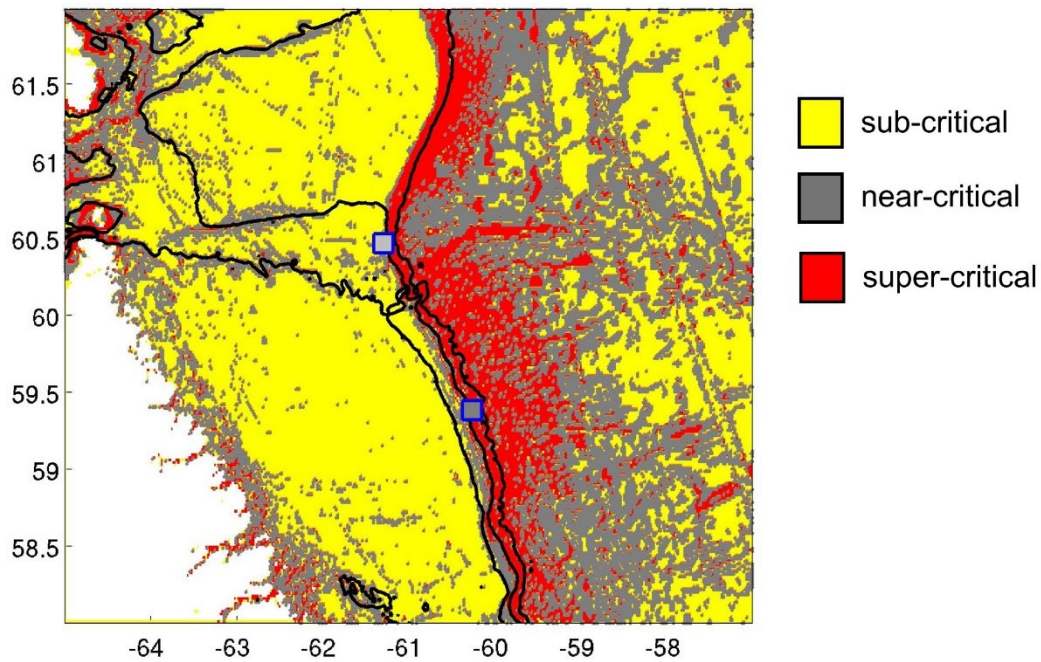
#### 576 4.2 Increased bottom nutrient concentrations

577 Both the LSB and HSB lander sites show higher nutrient concentrations in the bottom water  
578 compared with the other shelf/deep CTD stations, and this difference was more pronounced at  
579 the HSB lander location (Figure 4). Here we discuss two possible explanations for this  
580 observation: large scale advection of nutrient-rich water from Baffin Bay and sediment efflux  
581 of silicic acid. Intermediate water flows from Baffin Bay via the Davis Strait southward along

582 the continental slope (Curry et al., 2014). This water mass, referred to as Baffin Bay Water  
583 (BBW), contains high nutrient concentrations (e.g.,  $41.6 \pm 25.5 \mu\text{M Si(OH)}_4$ ,  $18.5 \pm 2.6 \mu\text{M}$   
584  $\text{NO}_3^-$ ; Sherwood et al., 2021) due to *in situ* remineralization of organic matter to deep water  
585 circulating in the Baffin Bay basin (Jones et al., 1984; Tremblay et al., 2002; Lehmann et al.,  
586 2019). Furthermore, BBW shows relatively high concentrations of silicate and phosphate  
587 compared to nitrate, due to denitrification at depth in Baffin Bay (Lehmann et al., 2019;  
588 Sherwood et al., 2021). Secondly, high efflux of silicic acid (nutrients) from the sediment could  
589 enhance bottom water silicate (nutrient) concentrations. Research on glass-sponge grounds on  
590 the Scotian shelf has shown that the biogenic silica efflux from sediments lead to higher bottom  
591 silicate concentrations (Maldonado et al., 2020a). This would also be possible for our study  
592 area. Given that the silicate concentration was elevated by  $\sim 2\text{-}3 \mu\text{M}$  up to 100 meters above  
593 the bottom (Figure 4), assuming that the length of the sponge ground was  $\sim 120 \text{ km}$  (Figure 1),  
594 and thereby estimating the retention time of a water parcel on the sponge grounds is about 33  
595 days (length sponge ground divided by residual current speed), this would mean that, under the  
596 assumption that the bottom 100m is well mixed, a sediment efflux of  $6 - 9 \text{ mmol Si m}^{-2} \text{ d}^{-1}$   
597 would be required. While this would be a substantial sediment efflux, silicate effluxes of  $2.4$   
598  $\text{mmol Si m}^{-2} \text{ d}^{-1}$  have been measured on the Scotian Shelf (Andrews and Hargrave, 1984;  
599 Maldonado et al., 2020a), and of up to  $14.1 \text{ mmol Si m}^{-2} \text{ d}^{-1}$  in the Laurentian Channel (East  
600 Canada; similar depth and temperature; Miatta and Snelgrove, 2021). Nonetheless, the higher  
601 silicate concentrations at HSB lander than at LSB lander imply that the source is located closer  
602 to HSB. The fact that phosphate was also enhanced in bottom waters at HSB, suggests that  
603 advection of nutrient-rich water from upstream is the more probable explanation. However,  
604 further work on bottom silicate concentrations in relation to sponge grounds in this area is  
605 needed to unravel the source of this excess silicate and investigate if and how sponge grounds  
606 benefit from this.

607 The elevated nutrient concentrations could be beneficial for benthic organisms, specifically,  
608 deep-sea sponges, which require silicic acid for spicule formation and skeletal growth (Whitney  
609 et al., 2005; Maldonado et al., 2011, 2020b; López-Acosta et al., 2016). Published kinetic  
610 uptake curves, describing silicic acid uptake rate *versus* concentration, suggests the  
611 concentration at the HSB lander ( $13.6 \mu\text{M}$ ) compared to LSB shelf ( $9.3 \mu\text{M}$ ) lead to a higher  
612 silicic acid uptake rates at the HSB site of 39% for *Axinella* spp. and 40% for *V. pourtalesii*  
613 (Maldonado et al., 2011, 2020b). Furthermore, elevated silicic acid concentrations on a spatial  
614 scale of kilometres are thought to allow the persistence of sponge grounds and build-up of  
615 (glass) sponge biomass over long timescales (Whitney et al., 2005; Maldonado et al., 2020a).

617 This study, to our knowledge, is the first to report year-long hydrodynamic- and environmental  
618 conditions measured simultaneously at a high- and low-sponge-biomass ground. Our  
619 measurements show high bottom currents at both sites with distinct differences in tidal  
620 dynamics. While semidiurnal tidal harmonics predominate at both sites, tidally driven  
621 horizontal current speeds were around five times higher at HSB than at LSB. At the HSB site,  
622 barotropic and near-bottom M2 tidal currents are oriented across-slope, but the near-bottom  
623 M2 tidal ellipse is smaller in magnitude and strongly indicating enhanced local near-bottom  
624 energy dissipation of the barotropic tide through tide-topography interaction (Table 2; Figure  
625 8). At the LSB site, near-bottom M2 and S2 tidal ellipses from the ADCP are oriented along-  
626 slope with a small across-slope component. In contrast, modelled barotropic semi-diurnal tidal  
627 harmonics were of similar magnitude, but mainly oriented across- interaction (Table 2; Figure  
628 8). This discrepancy is likely due to local changes in bathymetry (Figure S1), which are not  
629 resolved in the OTIS tidal model. The outcome of strongly enhanced current speeds at the HSB  
630 site is contrary to White (2003) who measured high current speeds in areas where no sponges  
631 were recorded, and vice versa, at the Porcupine Sea Bight. Caution should be applied  
632 comparing these areas, as the sponge fields in the Porcupine Sea Bight mostly consist of glass  
633 sponges, and here we see a mixture of glass sponges and massive demosponges. Bottom current  
634 speeds are higher at HSB than at LSB (Table 1), but bottom currents at LSB are still comparable  
635 with current speeds found at other sponge grounds on the Scotian Shelf (mean:  $0.12 \text{ m s}^{-1}$ ; Hanz  
636 et al., 2021a) and on the Arctic mid-Atlantic ridge (mean:  $0.14 \text{ m s}^{-1}$ ; Hanz et al., 2021b). The  
637 conversion of kinetic energy from barotropic to baroclinic tides and to turbulence over rough  
638 topography shapes the distribution of benthic filter feeding communities in many areas  
639 throughout the global ocean (van der Kaaden et al., 2024). At the northern Labrador shelf break,  
640 larger aggregations of sponges are mainly found on topographic slopes, where near-critical and  
641 super-critical reflection of internal waves are predicted (Figure 13).



642

643 *Figure 13: The internal wave slope parameter indicates sub-critical conditions across most of the Labrador Shelf and in the*  
 644 *deep Northwest Atlantic. Near-critical and super-critical conditions are primarily observed along the continental margin.*  
 645 *This analysis suggests that the HSB lander (northern point) was situated in near-critical conditions for the M2*  
 646 *tide, while the LSB lander (southern point) experienced supercritical bottom slopes for M2.*

647

#### 648 4.4 How can strong bottom currents benefit the benthic community?

649 Strong tidally-induced bottom currents can benefit the benthic community at the HSB site in  
 650 various ways. First, passive suspension feeders as the gorgonian *P. resedaeformis* benefit from  
 651 high horizontal currents through an increased particulate organic matter flux (Shimeta and  
 652 Jumars, 1991) and sponges (specifically glass sponges) could benefit from an increased water  
 653 flow rate through their body plan (Vogel, 1977; Leys et al., 2011), thereby increasing food  
 654 availability. Second, resuspension caused by oscillating tidal bottom currents enhance organic  
 655 matter and inorganic nutrient availability in the benthic boundary layer and enhance food  
 656 supply to the sponges (Roberts et al., 2018). In this study, high along-slope bottom currents at  
 657 both sites were associated with increased turbidity (both ABS and OBS), indicative of  
 658 resuspension. However, the beneficial effect of resuspension for sponge biomass is not yet fully  
 659 understood, as reoccurring strong turbidity flows (at LSB) could also prevent high sponge  
 660 biomass from developing by smothering young sponges when particles settle out (Klitgaard  
 661 and Tendal, 2004).

662 The substrate at HSB consisted mostly of pebbles, cobbles, and boulders (Dinn et al., 2020)  
 663 and a qualitative assessment of the sediment type at LSB suggested the dominance of muddy  
 664 soft sediment (Coté et al., 2019; J. Vad, *pers. com.*). As higher bottom currents would increase

665 bed shear stress and thereby enhance resuspension (Lesht, 1979; Jones et al., 1998), we argue  
666 that fine material is resuspended at HSB before its accumulation on the seafloor. This increases  
667 availability of organic matter to benthic suspension feeders in the benthic boundary layer and  
668 prevent smothering from sedimentation. Resuspension has also been linked to high sponge  
669 biomass (Davison et al., 2019), as potential food sources such as organic matter and bacteria  
670 can bind to suspended particles in the water column. The interaction of high bottom currents  
671 with rough topography causes turbulence and mixing of bottom waters (Witte et al., 1997; Leys  
672 et al., 2011; Culwick et al., 2020). As the substrate is likely rougher and bottom currents are  
673 higher at HSB than at LSB, the bottom water probably experiences more intense mixing and  
674 turbulence at HSB. Finally, periodic supply of fresh phytoplankton derived material during the  
675 spring bloom (Figure S10, Figure S11) increases the food availability of passive suspension  
676 feeders living on the sponge grounds. In short, the stronger tidal currents at HSB enhance  
677 bottom water mixing which replenishes oxygen, dissolved organic matter, POM, and  
678 (inorganic) nutrients in the benthic boundary layer, and thereby increases food supply to  
679 benthic fauna (Davison et al., 2019; Hanz et al., 2021b, 2021a).

#### 680 4.5 Surface productivity and benthic-pelagic coupling

681 The Hudson Strait outflow water is known to increase nutrient concentrations in the surface  
682 waters on the northern Labrador Shelf (Kollmeyer et al., 1967; Sutcliffe et al., 1983;  
683 Drinkwater and Harding, 2001). The increased nutrient supply supports high primary  
684 productivity in an area extending from the Hudson Strait to the southern Labrador Shelf,  
685 bounded by the thermal front associated with the 1,000 m isobath (Frajka-Williams et al., 2009;  
686 Frajka-Williams and Rhines, 2010; Cyr and Larouche, 2015). Previous studies show that  
687 surface chl-a concentrations are comparable between the two sponge grounds (see Figure 2A  
688 in Frajka-Williams and Rhines, 2010), suggesting that differences in surface productivity alone  
689 are insufficient to explain the differences sponge biomass between regions. Furthermore,  
690 studies elsewhere in the Canadian Arctic have shown that benthic biomass is explained not  
691 only by surface productivity but also by local hydrodynamics and benthic-pelagic coupling  
692 (Thomson, 1982; Grebmeier and Barry, 1991; Roy et al., 2014).

693 Our year-long recordings of bottom water chl-a concentrations provide evidence for strong  
694 benthic-pelagic coupling during spring in this region. The benthic landers showed early arrival  
695 of fresh phytodetritus in early March, a peak in chl-a mid April, and chl-a concentration was  
696 close to background values again from early May at LSB and from mid May at HSB (Figure  
697 9C). Studies on the onset of the phytoplankton bloom on the Labrador shelf show that blooms  
698 usually initiate around mid April and peak around mid June (Fuentes-Yaco et al., 2007; Frajka-



699 Williams and Rhines, 2010; Cyr et al., 2023). The study of Cyr et al. (2023) estimates that the  
700 standard deviation in timing of the initiation of the phytoplankton bloom is around 21 days. As  
701 environmental conditions of the Northern Labrador shelf were close to average during 2019  
702 (Cyr and Galbraith, 2021), we think its acceptable to assume phytoplankton bloom timing was  
703 similar to values found in literature. Therefore, arrival of phytodetritus at our benthic landers  
704 was then three months earlier to normal phytoplankton bloom timing. Earlier research has  
705 shown that chl-a starts to increase on the northern Labrador shelf from early March onwards  
706 (Harrison et al., 2013). During this time the water column is still relatively cold and poorly  
707 stratified, allowing for relatively high export of phytoplankton to the seafloor. Additionally,  
708 the short periods of low ice-cover mid February and mid March (Figure S11D) match the  
709 subsequent increase in bottom chl-a concentration seen for both landers (Figure 9C). The onset  
710 of the phytoplankton bloom for the northern Labrador shelf is around mid April, and related to  
711 the onset of stratification (Cyr et al., 2023) and sea-ice cover (Wu et al., 2007). The timing of  
712 peak bottom chl-a concentrations (mid April) and consequential decline compare well with the  
713 timing phytoplankton bloom initiation proposed by Cyr et al. (2023). They show there is a  
714 south-to-north progression of the phytoplankton bloom over the Labrador shelf, which matches  
715 with our data that shows chl-a concentrations stay elevated around three weeks longer at the  
716 more northern HSB lander. Furthermore, assuming surface chl-a concentration peaks in June,  
717 we can infer that there appears to be a decoupling between pelagic productivity and bottom  
718 chl-a concentration in summer, likely due to enhanced stratification and intense zooplankton  
719 grazing (Rivkin et al., 1996; Turner, 2015).

720 Our findings suggest strong benthic-pelagic coupling started weeks before the peak of the  
721 phytoplankton bloom, supplying fresh fluorescent material to the seafloor in spring for a period  
722 of weeks to months. Since the timing of phytoplankton bloom for high-latitude seas is shifting  
723 to earlier in the year due to rising temperatures and earlier sea-ice retreat (Edwards and  
724 Richardson, 2004; Wu et al., 2007; Hunter-Cevera et al., 2016), and since deep-sea sessile  
725 organisms, such as cold-water corals and deep-sea sponges demonstrate seasonality in their  
726 phenology (Leys and Lauzon, 1998; Maldonado, 2011; Maier et al., 2020a), the early arrival  
727 of phytoplankton-derived material could have consequences for their overall fitness and  
728 survival. Nevertheless, the effect of a shift in spring bloom timing for benthic suspension  
729 feeders, including deep-sea sponges, remains unknown.

730 Recent ABS measurements reveal a layer of increased 300 kHz backscatter along the northern  
731 Labrador Shelf, indicative of high abundance of micronekton and macrozooplankton  
732 (Chawarski et al., 2022). Earlier studies showed a high zooplankton biomass on the  
733 Newfoundland Shelf from July onwards (Head et al., 2003, 2013). In our traps the highest flux

734 of unsaturated alcohols, a biomarker for zooplankton (specifically copepods; Dalsgaard et al.,  
735 2003), and the highest numbers of swimmers were in summer and autumn. During the spring  
736 bloom, trapped material at LSB had the highest relative amount of unsaturated alcohols while  
737 at HSB the level of PUFAs, markers for phytoplankton derived-material, was highest  
738 (Dalsgaard et al., 2003). Furthermore, our observations suggest that the number of trapped  
739 swimmers was higher at LSB than at HSB. These results are consistent with the hypothesis that  
740 zooplankton biomass is high over the northern Labrador Shelf (Saglek Bank) and that  
741 zooplankton is transported by the southerly current along the Labrador Shelf together with the  
742 high phytoplankton biomass plume (Sutcliffe et al., 1983; Drinkwater and Harding, 2001).  
743 Overall, there was a larger fraction of zooplankton marker lipids in trapped material at LSB,  
744 which implies that zooplankton play a more important role in benthic-pelagic coupling at LSB  
745 than at HSB.

#### 746 4.6 Organic matter fluxes to the seafloor

747 Organic matter deposition was higher at the HSB lander than at the LSB lander. Overall,  
748 deposition was highest during the winter months and consisted of more degraded material than  
749 during summer, indicated by high C:N ratios and high  $\delta^{15}\text{N}$  values. This increased deposition  
750 in winter is likely resuspended material as shown by peaks in ABS turbidity in the bottom  
751 boundary layer and relate to higher current speeds. The C:N ratio of deposited matter was  
752 higher at LSB ( $\sim 13$ ) compared to HSB ( $\sim 8$ ), indicating the material was more degraded at LSB.  
753 Hanz et al. (2021a, 2021b) also found higher mass and carbon fluxes during winter months and  
754 low carbon fluxes when the spring/summer phytoplankton bloom arrived. They attributed this  
755 to the presence of more degraded and resuspended material in winter. Data concerning mass  
756 fluxes from sponge grounds remain scarce, but the fluxes measured here (HSB  $2.46 \pm 1.76 \text{ g}$   
757  $\text{m}^{-2} \text{ day}^{-1}$ , LSB:  $1.43 \pm 0.93 \text{ g m}^{-2} \text{ day}^{-1}$ ) were comparable to those of a *Vazella pourtalesii*  
758 sponge ground on the Scotian Shelf ( $3.17 \pm 3.42 \text{ g m}^{-2} \text{ day}^{-1}$ ; Hanz et al., 2021a) but  
759 substantially higher than those of a sponge ground on the Arctic mid-Atlantic ridge ( $0.03 -$   
760  $0.30 \text{ g m}^{-2} \text{ day}^{-1}$ ; Hanz et al., 2021b). Overall, our data suggest organic matter deposition fluxes  
761 are higher at HSB compared to LSB, and that the organic matter is of higher quality. The  
762 organic carbon fluxes (HSB:  $3.07 \pm 1.91 \text{ mmol C m}^{-2} \text{ d}^{-1}$ ; LSB:  $1.91 \pm 0.71 \text{ mmol C m}^{-2} \text{ d}^{-1}$ )  
763 reported in our study are considerably lower than those of a more shallow (150 – 250 m depth)  
764 *V. pourtalesii* sponge ground on the Scotian Shelf ( $8.3 \text{ mmol C m}^{-2} \text{ d}^{-1}$ ; Hanz et al., 2021a), but  
765 high compared to an Arctic mid-Atlantic ridge sponge ground (peak of  $1.6 \text{ mmol C m}^{-2} \text{ d}^{-1}$ ;  
766 Hanz et al., 2021b). The higher organic matter deposition rate and relative fresher material at  
767 HSB compared to LSB are likely related to its shallower position on the shelf and the more  
768 dynamic water column.

#### 769 4.7 Isotopic signatures of benthic macrofauna at two contrasting sponge grounds

770 Although the sample size was limited, the stable isotope data revealed interesting patterns of  
771 organic matter utilization by the benthic community. The gorgonian coral *P. resedaeformis* is  
772 found one trophic level (Fry, 2006) above the sediment trap material and therefore likely feeds  
773 on sinking organic matter, confirming previous observations (Sherwood et al., 2005, 2008).  
774 Sponges can generally be classified into two groups based on their associated microbial fauna,  
775 those with high microbial abundance (HMA) or those with low microbial abundance (LMA;  
776 Vacelet and Donadey, 1977). *Geodia* spp. can occur in high abundance and biomass on sponge  
777 grounds (Kutti et al., 2013). These sponges are considered HMA (Radax et al., 2012) and feed  
778 mostly on dissolved organic matter with additional particulate sources such as bacterioplankton  
779 (Bart et al., 2021). Many hexactinellidae that can form sponge grounds, for instance *Vazella*  
780 *pourtalessii* and *Aphrocallistes vastus*, are considered LMA sponges and feed mostly on  
781 bacterioplankton (Kahn et al., 2015). The high  $\delta^{15}\text{N}$  isotopic ratios for the sponges *Asconema*  
782 spp. ( $12.6 \pm 0.3 \text{‰ } \delta^{15}\text{N}$ ) and *Mycale* spp. ( $13.1 \pm 0.4 \text{‰ } \delta^{15}\text{N}$ ), have been observed previously  
783 for LMA sponges (Iken et al., 2001; Polunin, 2001; Kahn et al., 2018). Deep-sea LMA sponges  
784 typically have elevated  $\delta^{15}\text{N}$  values in the benthic food web (Kahn et al., 2018), a phenomenon  
785 that is still poorly understood. Possible explanations could be selective feeding on  $^{15}\text{N}$  enriched  
786 bacteria (Wilkinson et al., 1984), feeding on resuspended benthic bacteria (Kahn et al., 2018),  
787 or nitrogen (re)cycling within the sponge holobiont (Rooks et al., 2020; Hanz et al., 2022).  
788 Interestingly, the HMA massive sponge *Geodia* sp. has distinct  $\delta^{13}\text{C}$  and  $\delta^{15}\text{N}$  values, which  
789 was also observed in Hanz et al. (2022), indicating different feeding or metabolic strategies.  
790 Recent research on *Geodia baretii* has indeed demonstrated that these sponges rely in large  
791 part on DOM for their metabolic requirements (Bart et al., 2021; de Kluijver et al., 2021). In  
792 this study, *Geodia* spp. ( $8.2 \pm 0.2 \text{‰ } \delta^{15}\text{N}$ ) was one trophic level higher than oceanic DOM  
793  $\delta^{15}\text{N}$  ( $\sim 5 \text{‰}$ ; Benner et al., 2005; Sigman et al., 2009) and  $\delta^{15}\text{N-NO}_3^-$  ( $\sim 5 \text{‰}$ ; Sigman et al.,  
794 2009; Sherwood et al., 2021), limiting our ability to distinguish between DOM and  $\text{NO}_3^-$  (by  
795 i.e., denitrification; Hoffmann et al., 2009) as potential nitrogen sources. The  $\delta^{13}\text{C}$  value of  
796 *Geodia* spp. ( $-18.4 \pm 0.17 \text{‰ } \delta^{13}\text{C}$ ) is  $\pm 3.5 \text{‰}$  higher than bottom water  $\delta^{13}\text{C-DOC}$  values on  
797 the Labrador Shelf (Barber et al., 2017), i.e. more than four times higher than the expected  
798  $0.8 \text{‰ } \delta^{13}\text{C}$  step per trophic level (Vander Zanden and Rasmussen, 2001). Alternatively, *Geodia*  
799 spp. could capitalize on DIC via their symbionts (de Kluijver et al., 2021), as recently observed  
800 in Arctic *Geodia* spp. assemblages (Morganti et al., 2022) and other deep-sea sponges (van  
801 Duyl et al., 2020). Even limited chemoautotrophic assimilation of high  $\delta^{13}\text{C-DIC}$  ( $\sim 0 \text{‰ } \delta^{13}\text{C}$ )  
802 could explain the high  $\delta^{13}\text{C}$  values of *Geodia* spp. These results indicate that passive suspension  
803 feeders benefit from high tidal currents through an increased particulate organic matter flux

804 (Shimeta and Jumars, 1991), whereas sponges likely benefit from replenishment of nutrients,  
805 oxygen, and dissolved organic matter (Schlappy et al., 2010).

## 806 5 Conclusion

807 The aim this research was to obtain a better understanding of the environmental conditions in  
808 which sponge grounds occur and investigate the conditions in which high-sponge-biomass  
809 could develop. This study identified that the high-biomass sponge ground on the northern  
810 Labrador Shelf differ from the low-biomass sponge ground in the following ways: a more  
811 dynamic water column with strong tidal bottom currents and near-bottom energy dissipation  
812 by tide-topography interactions, increased bottom inorganic nutrient concentrations, and higher  
813 organic matter flux to the seafloor. Furthermore, both sponge grounds experienced strong  
814 benthic-pelagic coupling during spring and a decoupling during summer months. The elevated  
815 bottom nutrient concentrations at the high-sponge-biomass ground could be related to large  
816 scale circulation or sediment effluxes, and future work is needed to assess this. Our findings  
817 suggest a relation between slope-criticality and sponge biomass on the northern Labrador Shelf  
818 which could be interesting to investigate in future work. The deep-sea sponges and corals  
819 benefit from the dynamic water column in the high-biomass sponge ground by increased  
820 availability of food sources and nutrients.

## 821 6 Funding statement

822 This research was supported by the European Union's Horizon 2020 Research and Innovation  
823 Programme under grant agreement nos. 678760 (ATLAS) and 818123 (iAtlantic). This output  
824 reflects only the authors' view, and the European Union cannot be held responsible for any use  
825 that may be made of the information contained therein. Department of Fisheries and Oceans  
826 contributions were funded through the departmental International Governance Strategy  
827 programme awarded to EK. DvO was supported by the Innovational Research Incentives  
828 Scheme of the Netherlands Organisation for Scientific Research (NWO), respectively, under  
829 grant agreement 864.13.007. EdF was partly supported by ArcticNet Network of Centres of  
830 Excellence, Glacier troughs as biodiversity and abundance hotspots in Arctic and subarctic  
831 regions project, ArcticNet Phase V (Geoffroy et al.). The data presented herein were collected  
832 by the Canadian research icebreaker CCGS Amundsen and made available by the Amundsen  
833 Science program, which was supported by the Canada Foundation for Innovation and Natural  
834 Sciences and Engineering Research Council of Canada. The views expressed in this publication  
835 do not necessarily represent the views of Amundsen Science or that of its partners. Ship-time  
836 on the CCGS Amundsen was also funded by an NSERC ship-time grant (Edinger et al., grant

837 nr.: RGPST-515528-2018), ArcticNet Network of Centers of Excellence Canada, and the  
838 Department of Fisheries and Oceans Canada (DFO; Coté et al.). The funders had no role in  
839 study design, data collection, and analysis, decision to publish, or preparation of the  
840 manuscript.

841

## 842 7 Author statement

843 EDF: sample analysis, data analysis, and writing; IY: data collection, data analysis, and writing.  
844 CM: conceptualization, data analysis and writing; JV: data collection and data analysis; FM:  
845 conceptualization, sample analysis and data analysis; GD: conceptualization, data analysis;  
846 EK, EH, IY, SWR, MR: conceptualization and site selection; SWR, MR, EK, BM, GT: site  
847 contribution and preparation of benthic landers; GW: conceptualization, sample analysis, data  
848 analysis, and writing; SB: data collection and sample analysis; DvO: conceptualization, data  
849 analysis, writing. All authors contributed to the article and approved the submitted version.

## 850 8 Acknowledgements

851 We would like to thank the skillful crew and technicians on board CCGS Amundsen for their  
852 support during the fieldwork. Specifically, we thank Dr. Paul Snelgrove (Memorial University  
853 of Newfoundland), Dr. David Cote (DFO) and Shawn Meredyk (Amundsen Science) for their  
854 assistance in facilitating our field programme. Cam Lirette (DFO) assisted in preparing various  
855 data layers to assist in site selection. We would also like to thank Jan Peene for nutrient  
856 analysis, Peter van Breugel and Jurian Brasser for help in measuring  
857 macrofauna/POM/sediment trap stable isotopes, and Pascal Guillot for quality assurance of the  
858 CTD profiles. Finally, we thank Kevin MacIsaac and Marc Ringuette for their help in  
859 identifying the sediment trap swimmers.

## 860 9 Data availability

861 Raw data will be stored on zenodo and URL will be provided upon acceptance of the  
862 manuscript.

## 863 10 References

864 Abelson, A., and Denny, M. (1997). Settlement of Marine Organisms in Flow. *Annu. Rev.*  
865 *Ecol. Syst.* 28, 317–339. doi: 10.1146/annurev.ecolsys.28.1.317

- 866 Andrews, D., and Hargrave, B. T. (1984). Close interval sampling of interstitial silicate and  
867 porosity in marine sediments. *Geochim. Cosmochim. Acta* 48, 711–722. doi:  
868 10.1016/0016-7037(84)90097-8
- 869 Barber, A., Sirois, M., Chaillou, G., and Gélinas, Y. (2017). Stable isotope analysis of  
870 dissolved organic carbon in Canada’s eastern coastal waters. *Limnol. Oceanogr.* 62,  
871 S71–S84. doi: 10.1002/lno.10666
- 872 Bart, M. C., Mueller, B., Rombouts, T., van de Ven, C., Tompkins, G. J., Osinga, R., et al.  
873 (2021). Dissolved organic carbon (DOC) is essential to balance the metabolic  
874 demands of four dominant North-Atlantic deep-sea sponges. *Limnol. Oceanogr.* 66,  
875 925–938. doi: 10.1002/lno.11652
- 876 Beazley, L. I., Kenchington, E. L., Murillo, F. J., and Sacau, M. del M. (2013). Deep-sea  
877 sponge grounds enhance diversity and abundance of epibenthic megafauna in the  
878 Northwest Atlantic. *ICES J. Mar. Sci.* 70, 1471–1490. doi: 10.1093/icesjms/fst124
- 879 Beazley, L., Kenchington, E., Murillo, F., Brickman, D., Wang, Z., Davies, A., et al. (2021).  
880 Climate change winner in the deep sea? Predicting the impacts of climate change on  
881 the distribution of the glass sponge *Vazella pourtalesii*. *Mar. Ecol. Prog. Ser.* 657, 1–  
882 23. doi: 10.3354/meps13566
- 883 Beazley, L., Wang, Z., Kenchington, E., Yashayaev, I., Rapp, H. T., Xavier, J. R., et al.  
884 (2018). Predicted distribution of the glass sponge *Vazella pourtalesi* on the Scotian  
885 Shelf and its persistence in the face of climatic variability. *PLOS ONE* 13, e0205505.  
886 doi: 10.1371/journal.pone.0205505
- 887 Belkin, I. M. (2009). Rapid warming of Large Marine Ecosystems. *Prog. Oceanogr.* 81, 207–  
888 213. doi: 10.1016/j.pocean.2009.04.011
- 889 Benner, R., Louchouart, P., and Amon, R. M. W. (2005). Terrigenous dissolved organic  
890 matter in the Arctic Ocean and its transport to surface and deep waters of the North  
891 Atlantic. *Glob. Biogeochem. Cycles*, 11.
- 892 Bergquist, P. R. (1978). *Sponges*. University of California Press.
- 893 Bloomfield, P. (2004). *Fourier analysis of time series: an introduction*. John Wiley & Sons.
- 894 Brito-Morales, I., Schoeman, D. S., Molinos, J. G., Burrows, M. T., Klein, C. J., Arafeh-  
895 Dalmau, N., et al. (2020). Climate velocity reveals increasing exposure of deep-ocean  
896 biodiversity to future warming. *Nat. Clim. Change* 10, 576–581. doi: 10.1038/s41558-  
897 020-0773-5
- 898 Brodnicke, O. B., Meyer, H. K., Busch, K., Xavier, J. R., Knudsen, S. W., Møller, P. R., et al.  
899 (2023). Deep-sea sponge derived environmental DNA analysis reveals demersal fish  
900 biodiversity of a remote Arctic ecosystem. *Environ. DNA* 5, 1405–1417. doi:  
901 10.1002/edn3.451
- 902 Buhl-Mortensen, L., Vanreusel, A., Gooday, A. J., Levin, L. A., Priede, I. G., Buhl-  
903 Mortensen, P., et al. (2010). Biological structures as a source of habitat heterogeneity  
904 and biodiversity on the deep ocean margins. *Mar. Ecol.* 31, 21–50. doi:  
905 10.1111/j.1439-0485.2010.00359.x

- 906 Canadian Ice Service (2022). Latest Ice conditions. Available at:  
907 [https://www.canada.ca/en/environment-climate-change/services/ice-forecasts-](https://www.canada.ca/en/environment-climate-change/services/ice-forecasts-observations/latest-conditions.html)  
908 [observations/latest-conditions.html](https://www.canada.ca/en/environment-climate-change/services/ice-forecasts-observations/latest-conditions.html) (Accessed January 2, 2022).
- 909 Cathalot, C., Van Oevelen, D., Cox, T. J. S., Kutti, T., Lavaleye, M., Duineveld, G., et al.  
910 (2015). Cold-water coral reefs and adjacent sponge grounds: hotspots of benthic  
911 respiration and organic carbon cycling in the deep sea. *Front. Mar. Sci.* 2. doi:  
912 10.3389/fmars.2015.00037
- 913 Centurioni, L. R., Turton, J., Lumpkin, R., Braasch, L., Brassington, G., Chao, Y., et al.  
914 (2019). Global in situ Observations of Essential Climate and Ocean Variables at the  
915 Air–Sea Interface. *Front. Mar. Sci.* 6. doi: 10.3389/fmars.2019.00419
- 916 Chawarski, J., Klevjer, T., Coté, D., and Geoffroy, M. (2022). The transformation of  
917 mesopelagic structure across polar fronts. *Res. Sq.* doi: 10.21203/rs.3.rs-244272/v1
- 918 Christie, W. W. (1982). A simple procedure for rapid transmethylolation of glycerolipids and  
919 cholesteryl esters. *J. Lipid Res.* 23, 1072–1075. doi: 10.1016/S0022-2275(20)38081-0
- 920 Colaço, A., Rapp, H. T., Campaña-Llovet, N., and Pham, C. K. (2022). Bottom trawling in  
921 sponge grounds of the Barents Sea (Arctic Ocean): A functional diversity approach.  
922 *Deep Sea Res. Part Oceanogr. Res. Pap.* 183, 103742. doi:  
923 10.1016/j.dsr.2022.103742
- 924 Coté, D., Edinger, E. N., and Mercier, A. (2018). CCGS Amundsen Field Report. Integrated  
925 studies and ecosystem characterization of the Labrador Sea Deep Ocean (ISECOLD).  
926 Available at: <https://amundsenscience.com/expeditions/2018-expedition/>
- 927 Coté, D., Geoffroy, M., Sherwood, O. A., Neves, B. M., Mercier, A., Hubert, C., et al.  
928 (2019). CCGS Amundsen Field Report. Integrated studies and ecosystem  
929 characterization of the Labrador Sea Deep Ocean (ISECOLD). Available at:  
930 <https://zenodo.org/records/3862120>
- 931 Culwick, T., Phillips, J., Goodwin, C., Rayfield, E. J., and Hendry, K. R. (2020). Sponge  
932 Density and Distribution Constrained by Fluid Forcing in the Deep Sea. *Front. Mar.*  
933 *Sci.* 7, 395. doi: 10.3389/fmars.2020.00395
- 934 Cuny, J., Rhines, P. B., Niiler, P. P., and Bacon, S. (2002). Labrador Sea Boundary Currents  
935 and the Fate of the Irminger Sea Water. *J. Phys. Oceanogr.* 32, 627–647. doi:  
936 10.1175/1520-0485(2002)032<0627:LSBCAT>2.0.CO;2
- 937 Curry, B., Lee, C. M., and Petrie, B. (2011). Volume, Freshwater, and Heat Fluxes through  
938 Davis Strait, 2004–05. *J. Phys. Oceanogr.* 41, 429–436. doi: 10.1175/2010JPO4536.1
- 939 Curry, B., Lee, C. M., Petrie, B., Moritz, R. E., and Kwok, R. (2014). Multiyear Volume,  
940 Liquid Freshwater, and Sea Ice Transports through Davis Strait, 2004–10. *J. Phys.*  
941 *Oceanogr.* 44, 1244–1266. doi: 10.1175/JPO-D-13-0177.1
- 942 Cyr, F., and Galbraith, P. S. (2021). A climate index for the Newfoundland and Labrador  
943 shelf. *Earth Syst. Sci. Data* 13, 1807–1828. doi: 10.5194/essd-13-1807-2021
- 944 Cyr, F., and Larouche, P. (2015). Thermal Fronts Atlas of Canadian Coastal Waters.  
945 *Atmosphere-Ocean* 53, 212–236. doi: 10.1080/07055900.2014.986710

- 946 Cyr, F., Lewis, K., Bélanger, D., Regular, P., Clay, S., and Devred, E. (2023). Physical  
947 controls and ecological implications of the timing of the spring phytoplankton bloom  
948 on the Newfoundland and Labrador shelf. *Limnol. Oceanogr. Lett.* n/a. doi:  
949 10.1002/lol2.10347
- 950 Dalsgaard, J., St. John, M., Kattner, G., Müller-Navarra, D., and Hagen, W. (2003). “Fatty  
951 acid trophic markers in the pelagic marine environment,” in *Advances in Marine*  
952 *Biology*, (Elsevier), 225–340. doi: 10.1016/S0065-2881(03)46005-7
- 953 Davison, J. J., van Haren, H., Hosegood, P., Piechaud, N., and Howell, K. L. (2019). The  
954 distribution of deep-sea sponge aggregations (Porifera) in relation to oceanographic  
955 processes in the Faroe-Shetland Channel. *Deep Sea Res. Part Oceanogr. Res. Pap.*  
956 146, 55–61. doi: 10.1016/j.dsr.2019.03.005
- 957 de Kluijver, A., Bart, M. C., van Oevelen, D., de Goeij, J. M., Leys, S. P., Maier, S. R., et al.  
958 (2021). An Integrative Model of Carbon and Nitrogen Metabolism in a Common  
959 Deep-Sea Sponge (*Geodia barretti*). *Front. Mar. Sci.* 7, 1131. doi:  
960 10.3389/fmars.2020.596251
- 961 Dinn, C., Zhang, X., Edinger, E., and Leys, S. P. (2020). Sponge communities in the eastern  
962 Canadian Arctic: species richness, diversity and density determined using targeted  
963 benthic sampling and underwater video analysis. *Polar Biol.* 43, 1287–1305. doi:  
964 10.1007/s00300-020-02709-z
- 965 Drinkwater, K. F., and Harding, G. C. (2001). Effects of the Hudson Strait outflow on the  
966 biology of the Labrador Shelf. *Can. J. Fish. Aquat. Sci.* 58, 171–184. doi:  
967 10.1139/f00-210
- 968 Drinkwater, K. F., and Jones, E. P. (1987). Density stratification, nutrient and chlorophyll  
969 distributions in the Hudson Strait region during summer and their relation to tidal  
970 mixing. *Cont. Shelf Res.* 7, 599–607. doi: 10.1016/0278-4343(87)90025-2
- 971 Dunbar, M. J. (1951). *Eastern Arctic waters: a summary of our present knowledge of the*  
972 *physical oceanography of the eastern arctic area, from Hudson bay to cape Farewell*  
973 *and from Bell Isle to Smith sound*. Ottawa: Fisheries Research Board of Canada.
- 974 Edwards, M., and Richardson, A. J. (2004). Impact of climate change on marine pelagic  
975 phenology and trophic mismatch. *Nature* 430, 881–884. doi: 10.1038/nature02808
- 976 Egbert, G. D., and Erofeeva, S. Y. (2002). Efficient Inverse Modeling of Barotropic Ocean  
977 Tides. *J. Atmospheric Ocean. Technol.* 19, 183–204. doi: 10.1175/1520-  
978 0426(2002)019<0183:EIMOBO>2.0.CO;2
- 979 Elipot, S., Lumpkin, R., Perez, R. C., Lilly, J. M., Early, J. J., and Sykulski, A. M. (2016). A  
980 global surface drifter data set at hourly resolution. *J. Geophys. Res. Oceans* 121,  
981 2937–2966. doi: 10.1002/2016JC011716
- 982 Elipot, S., Sykulski, A. M., Lumpkin, R., Centurioni, L. R., and Pazos, M. (2022). Hourly  
983 location, current velocity, and temperature collected from Global Drifter Program  
984 drifters world-wide. Available at: <https://doi.org/10.25921/x46c-3620> (Accessed  
985 January 7, 2023).
- 986 Fissel, D. B., and Lemon, D. D. (1991). Analysis of physical oceanographic data from the  
987 Labrador Shelf, summer 1980. Available at:  
988 <https://www.osti.gov/etdweb/biblio/5105285> (Accessed December 17, 2021).



- 989 Frajka-Williams, E., and Rhines, P. B. (2010). Physical controls and interannual variability of  
990 the Labrador Sea spring phytoplankton bloom in distinct regions. *Deep Sea Res. Part*  
991 *Oceanogr. Res. Pap.* 57, 541–552. doi: 10.1016/j.dsr.2010.01.003
- 992 Frajka-Williams, E., Rhines, P. B., and Eriksen, C. C. (2009). Physical controls and  
993 mesoscale variability in the Labrador Sea spring phytoplankton bloom observed by  
994 Seaglider. *Deep Sea Res. Part Oceanogr. Res. Pap.* 56, 2144–2161. doi:  
995 10.1016/j.dsr.2009.07.008
- 996 Fry, B. (2006). *Stable Isotope Ecology*. New York: Springer-Verlag. doi: 10.1007/0-387-  
997 33745-8
- 998 Fuentes-Yaco, C., Koeller, P. A., Sathyendranath, S., and Platt, T. (2007). Shrimp (*Pandalus*  
999 *borealis*) growth and timing of the spring phytoplankton bloom on the  
1000 Newfoundland–Labrador Shelf. *Fish. Oceanogr.* 16, 116–129. doi: 10.1111/j.1365-  
1001 2419.2006.00402.x
- 1002 GEBCO Bathymetric Compilation Group (2023). The GEBCO\_2023 Grid - a continuous  
1003 terrain model of the global oceans and land. doi: 10.5285/f98b053b-0cbc-6c23-e053-  
1004 6c86abc0af7b
- 1005 Gille, S. T., Metzger, E. J., and Tokmakian (2004). Seafloor Topography and Ocean  
1006 Circulation. *Oceanography*. Available at: <https://doi.org/10.5670/oceanog.2004.66>
- 1007 Grebmeier, J. M., and Barry, J. P. (1991). The influence of oceanographic processes on  
1008 pelagic-benthic coupling in polar regions: A benthic perspective. *J. Mar. Syst.* 2, 495–  
1009 518. doi: 10.1016/0924-7963(91)90049-Z
- 1010 Griffiths, D. K., Pingree, R. D., and Sinclair, M. (1981). Summer tidal fronts in the near-  
1011 arctic regions of Foxe Basin and Hudson Bay. *Deep Sea Res. Part Oceanogr. Res.*  
1012 *Pap.* 28, 865–873. doi: 10.1016/S0198-0149(81)80006-4
- 1013 Grolemond, G., and Wickham, H. (2011). Dates and Times Made Easy with lubridate. *J. Stat.*  
1014 *Softw.* 40, 1–25.
- 1015 Guillot, P. (2018). Cruise Bright/SN/Atlas 1802 (leg 2) CTD processing notes. Amundsen  
1016 Science.
- 1017 Haalboom, S., de Stigter, H. C., Mohn, C., Vandorpe, T., Smit, M., de Jonge, L., et al. (2023).  
1018 Monitoring of a sediment plume produced by a deep-sea mining test in shallow water,  
1019 Málaga Bight, Alboran Sea (southwestern Mediterranean Sea). *Mar. Geol.* 456,  
1020 106971. doi: 10.1016/j.margeo.2022.106971
- 1021 Haalboom, S., de Stigter, H., Duineveld, G., van Haren, H., Reichart, G.-J., and Mienis, F.  
1022 (2021). Suspended particulate matter in a submarine canyon (Whittard Canyon, Bay  
1023 of Biscay, NE Atlantic Ocean): Assessment of commonly used instruments to record  
1024 turbidity. *Mar. Geol.* 434, 106439. doi: 10.1016/j.margeo.2021.106439
- 1025 Hanz, U., Beazley, L., Kenchington, E., Duineveld, G., Rapp, H. T., and Mienis, F. (2021a).  
1026 Seasonal Variability in Near-bed Environmental Conditions in the *Vazella pourtalesii*  
1027 Glass Sponge Grounds of the Scotian Shelf. *Front. Mar. Sci.* 7, 597682. doi:  
1028 10.3389/fmars.2020.597682
- 1029 Hanz, U., Riekenberg, P., de Kluijver, A., van der Meer, M., Middelburg, J. J., de Goeij, J.  
1030 M., et al. (2022). The important role of sponges in carbon and nitrogen cycling in a

- 1031 deep-sea biological hotspot. *Funct. Ecol.* 36, 2188–2199. doi: 10.1111/1365-  
1032 2435.14117
- 1033 Hanz, U., Roberts, E. M., Duineveld, G., Davies, A., Haren, H. van, Rapp, H. T., et al.  
1034 (2021b). Long-term Observations Reveal Environmental Conditions and Food Supply  
1035 Mechanisms at an Arctic Deep-Sea Sponge Ground. *J. Geophys. Res. Oceans* 126,  
1036 e2020JC016776. doi: <https://doi.org/10.1029/2020JC016776>
- 1037 Harrison, G. W., Yngve Børsheim, K., Li, W. K. W., Maillet, G. L., Pepin, P., Sakshaug, E.,  
1038 et al. (2013). Phytoplankton production and growth regulation in the Subarctic North  
1039 Atlantic: A comparative study of the Labrador Sea-Labrador/Newfoundland shelves  
1040 and Barents/Norwegian/Greenland seas and shelves. *Prog. Oceanogr.* 114, 26–45.  
1041 doi: 10.1016/j.pocean.2013.05.003
- 1042 Head, E. J. H., Harris, L. R., and Yashayaev, I. (2003). Distributions of *Calanus* spp. and  
1043 other mesozooplankton in the Labrador Sea in relation to hydrography in spring and  
1044 summer (1995–2000). *Prog. Oceanogr.* 59, 1–30. doi: 10.1016/S0079-  
1045 6611(03)00111-3
- 1046 Head, E. J. H., Melle, W., Pepin, P., Bagøien, E., and Broms, C. (2013). On the ecology of  
1047 *Calanus finmarchicus* in the Subarctic North Atlantic: A comparison of population  
1048 dynamics and environmental conditions in areas of the Labrador Sea-  
1049 Labrador/Newfoundland Shelf and Norwegian Sea Atlantic and Coastal Waters. *Prog.*  
1050 *Oceanogr.* 114, 46–63. doi: 10.1016/j.pocean.2013.05.004
- 1051 Hoffmann, F., Radax, R., Woebken, D., Holtappels, M., Lavik, G., Rapp, H. T., et al. (2009).  
1052 Complex nitrogen cycling in the sponge *Geodia barretti*. *Environ. Microbiol.* 11,  
1053 2228–2243. doi: 10.1111/j.1462-2920.2009.01944.x
- 1054 Hogg, M., Tendal, O., Conway, K., Pomponi, S., Gutt, J., Krautter, M., et al. (2010). Deep-  
1055 sea sponge grounds: Reservoirs of biodiversity.
- 1056 Howell, K.-L., Piechaud, N., Downie, A.-L., and Kenny, A. (2016). The distribution of deep-  
1057 sea sponge aggregations in the North Atlantic and implications for their effective  
1058 spatial management. *Deep Sea Res. Part Oceanogr. Res. Pap.* 115, 309–320. doi:  
1059 10.1016/j.dsr.2016.07.005
- 1060 Hunter-Cevera, K. R., Neubert, M. G., Olson, R. J., Solow, A. R., Shalapyonok, A., and  
1061 Sosik, H. M. (2016). Physiological and ecological drivers of early spring blooms of a  
1062 coastal phytoplankter. *Science* 354, 326–329. doi: 10.1126/science.aaf8536
- 1063 Iken, K., Brey, T., Wand, U., Voigt, J., and Junghans, P. (2001). Food web structure of the  
1064 benthic community at the Porcupine Abyssal Plain (NE Atlantic): a stable isotope  
1065 analysis. *Prog. Oceanogr.* 50, 383–405. doi: 10.1016/S0079-6611(01)00062-3
- 1066 Jones, E. P., Dyrssen, D., and Coote, A. R. (1984). Nutrient Regeneration in Deep Baffin Bay  
1067 with Consequences for Measurements of the Conservative Tracer NO and Fossil Fuel  
1068 CO<sub>2</sub> in the Oceans. *Can. J. Fish. Aquat. Sci.* 41, 30–35. doi: 10.1139/f84-003
- 1069 Jones, S. E., Jago, C. F., Bale, A. J., Chapman, D., Howland, R. J. M., and Jackson, J. (1998).  
1070 Aggregation and resuspension of suspended particulate matter at a seasonally  
1071 stratified site in the southern North Sea: physical and biological controls. *Cont. Shelf*  
1072 *Res.* 18, 1283–1309. doi: 10.1016/S0278-4343(98)00044-2

- 1073 Jorda, G., Marbà, N., Bennett, S., Santana-Garcon, J., Agusti, S., and Duarte, C. M. (2020).  
1074 Ocean warming compresses the three-dimensional habitat of marine life. *Nat. Ecol.*  
1075 *Evol.* 4, 109–114. doi: 10.1038/s41559-019-1058-0
- 1076 Kahn, A. S., Chu, J. W. F., and Leys, S. P. (2018). Trophic ecology of glass sponge reefs in  
1077 the Strait of Georgia, British Columbia. *Sci. Rep.* 8, 756. doi: 10.1038/s41598-017-  
1078 19107-x
- 1079 Kahn, A. S., Yahel, G., Chu, J. W. F., Tunnicliffe, V., and Leys, S. P. (2015). Benthic grazing  
1080 and carbon sequestration by deep-water glass sponge reefs: Deep-water glass sponge  
1081 reefs. *Limnol. Oceanogr.* 60, 78–88. doi: 10.1002/lno.10002
- 1082 Kazanidis, G., van Oevelen, D., Veuger, B., and Witte, U. F. M. (2018). Unravelling the  
1083 versatile feeding and metabolic strategies of the cold-water ecosystem engineer  
1084 *Spongosorites coralliophaga* (Stephens, 1915). *Deep Sea Res. Part Oceanogr. Res.*  
1085 *Pap.* 141, 71–82. doi: 10.1016/j.dsr.2018.07.009
- 1086 Kelley, D., and Richards, C. (2020). *oce: Analysis of Oceanographic Data*. Available at:  
1087 <https://CRAN.R-project.org/package=oce>
- 1088 Kenchington, E. L., Lirette, C., Cogswell, A., Archambault, D., Archambault, P., Benoit, H.,  
1089 et al. (2010). Delineating Coral and Sponge Concentrations in the Biogeographic  
1090 Regions of the East Coast of Canada Using Spatial Analyses. *DFO Can Sci Advis Sec*  
1091 *Res Doc*, vi + 202 pp.
- 1092 Kenchington, E., Power, D., and Koen-Alonso, M. (2013). Associations of demersal fish with  
1093 sponge grounds on the continental slopes of the northwest Atlantic. *Mar. Ecol. Prog.*  
1094 *Ser.* 477, 217–230. doi: 10.3354/meps10127
- 1095 Kenchington, E., Yashayaev, I., Tendal, O. S., and Jørgensbye, H. (2017). Water mass  
1096 characteristics and associated fauna of a recently discovered *Lophelia pertusa*  
1097 (*Scleractinia*: *Anthozoa*) reef in Greenlandic waters. *Polar Biol.* 40, 321–337. doi:  
1098 10.1007/s00300-016-1957-3
- 1099 Kieke, D., and Yashayaev, I. (2015). Studies of Labrador Sea Water formation and variability  
1100 in the subpolar North Atlantic in the light of international partnership and  
1101 collaboration. *Prog. Oceanogr.* 132, 220–232. doi: 10.1016/j.pocean.2014.12.010
- 1102 Kiriakoulakis, K., Bett, B. J., White, M., and Wolff, G. A. (2004). Organic biogeochemistry  
1103 of the Darwin Mounds, a deep-water coral ecosystem, of the NE Atlantic. *Deep Sea*  
1104 *Res. Part Oceanogr. Res. Pap.* 51, 1937–1954. doi: 10.1016/j.dsr.2004.07.010
- 1105 Klitgaard, A. B. (1995). The fauna associated with outer shelf and upper slope sponges  
1106 (*Porifera*, *Demospongiae*) at the Faroe Islands, northeastern Atlantic. *Sarsia* 80, 1–22.  
1107 doi: 10.1080/00364827.1995.10413574
- 1108 Klitgaard, A. B., and Tendal, O. S. (2004). Distribution and species composition of mass  
1109 occurrences of large-sized sponges in the northeast Atlantic. *Prog. Oceanogr.* 61, 57–  
1110 98. doi: 10.1016/j.pocean.2004.06.002
- 1111 Knudby, A., Kenchington, E., and Murillo, F. J. (2013). Modeling the Distribution of *Geodia*  
1112 *Sponges* and Sponge Grounds in the Northwest Atlantic. *PLoS ONE* 8, e82306. doi:  
1113 10.1371/journal.pone.0082306

- 1114 Kollmeyer, R. C., United States. Coast Guard. Oceanographic Unit, McGill, D. A. (David A.  
1115 ), and Corwin, N. (1967). *Oceanography of the Labrador Sea in the vicinity of*  
1116 *Hudson Strait in 1965*. Washington, D.C. : U.S. Coast Guard Oceanographic Unit.  
1117 Available at: <http://archive.org/details/oceanographyofla00koll> (Accessed January 28,  
1118 2022).
- 1119 Kutti, T., Bannister, R. J., and Fosså, J. H. (2013). Community structure and ecological  
1120 function of deep-water sponge grounds in the Traenadypet MPA—Northern  
1121 Norwegian continental shelf. *Cont. Shelf Res.* 69, 21–30. doi:  
1122 10.1016/j.csr.2013.09.011
- 1123 Kutti, T., Fosså, J., and Bergstad, O. (2015). Influence of structurally complex benthic  
1124 habitats on fish distribution. *Mar. Ecol. Prog. Ser.* 520, 175–190. doi:  
1125 10.3354/meps11047
- 1126 Lazier, J., Hendry, R., Clarke, A., Yashayaev, I., and Rhines, P. (2002). Convection and  
1127 restratification in the Labrador Sea, 1990–2000. *Deep Sea Res. Part Oceanogr. Res.*  
1128 *Pap.* 49, 1819–1835. doi: 10.1016/S0967-0637(02)00064-X
- 1129 Lehmann, N., Kienast, M., Granger, J., Bourbonnais, A., Altabet, M. A., and Tremblay, J.-É.  
1130 (2019). Remote Western Arctic Nutrients Fuel Remineralization in Deep Baffin Bay.  
1131 *Glob. Biogeochem. Cycles* 33, 649–667. doi: 10.1029/2018GB006134
- 1132 Lesht, B. M. (1979). Relationship between sediment resuspension and the statistical  
1133 frequency distribution of bottom shear stress. *Mar. Geol.* 32, M19–M27. doi:  
1134 10.1016/0025-3227(79)90142-7
- 1135 Leys, S. P., and Lauzon, N. R. J. (1998). Hexactinellid sponge ecology: growth rates and  
1136 seasonality in deep water sponges. *J. Exp. Mar. Biol. Ecol.* 230, 111–129. doi:  
1137 10.1016/S0022-0981(98)00088-4
- 1138 Leys, S. P., Yahel, G., Reidenbach, M. A., Tunnicliffe, V., Shavit, U., and Reiswig, H. M.  
1139 (2011). The Sponge Pump: The Role of Current Induced Flow in the Design of the  
1140 Sponge Body Plan. *PLoS ONE* 6, e27787. doi: 10.1371/journal.pone.0027787
- 1141 López-Acosta, M., Leynaert, A., and Maldonado, M. (2016). Silicon consumption in two  
1142 shallow-water sponges with contrasting biological features. *Limnol. Oceanogr.* 61,  
1143 2139–2150. doi: 10.1002/lno.10359
- 1144 Lovelace, R., Félix, R., and Talbot, J. (2022). *slopes: Calculate Slopes of Roads, Rivers and*  
1145 *Trajectories*.
- 1146 Maier, S. R., Bannister, R. J., van Oevelen, D., and Kutti, T. (2020a). Seasonal controls on  
1147 the diet, metabolic activity, tissue reserves and growth of the cold-water coral  
1148 *Lophelia pertusa*. *Coral Reefs* 39, 173–187. doi: 10.1007/s00338-019-01886-6
- 1149 Maier, S. R., Kutti, T., Bannister, R. J., Fang, J. K.-H., van Breugel, P., van Rijswijk, P., et al.  
1150 (2020b). Recycling pathways in cold-water coral reefs: Use of dissolved organic  
1151 matter and bacteria by key suspension feeding taxa. *Sci. Rep.* 10, 9942. doi:  
1152 10.1038/s41598-020-66463-2
- 1153 Maldonado, M. (2011). The ecology of the sponge larva. *Can. J. Zool.* doi: 10.1139/z05-177
- 1154 Maldonado, M., Beazley, L., López-Acosta, M., Kenchington, E., Casault, B., Hanz, U., et al.  
1155 (2020a). Massive silicon utilization facilitated by a benthic-pelagic coupled feedback

- 1156 sustains deep-sea sponge aggregations. *Limnol. Oceanogr.*, lno.11610. doi:  
1157 10.1002/lno.11610
- 1158 Maldonado, M., López-Acosta, M., Beazley, L., Kenchington, E., Koutsouveli, V., and  
1159 Riesgo, A. (2020b). Cooperation between passive and active silicon transporters  
1160 clarifies the ecophysiology and evolution of biosilicification in sponges. *Sci. Adv.* 6,  
1161 eaba9322. doi: 10.1126/sciadv.aba9322
- 1162 Maldonado, M., Navarro, L., Grasa, A., Gonzalez, A., and Vaquerizo, I. (2011). Silicon  
1163 uptake by sponges: a twist to understanding nutrient cycling on continental margins.  
1164 *Sci. Rep.* 1, 30. doi: 10.1038/srep00030
- 1165 Maldonado, M., Ribes, M., and van Duyl, F. C. (2012). “Nutrient Fluxes Through Sponges,”  
1166 in *Advances in Marine Biology*, (Elsevier), 113–182. doi: 10.1016/B978-0-12-  
1167 394283-8.00003-5
- 1168 MATLAB (2010). *version 7.10.0 (R2010a)*. Natick, Massachusetts: The MathWorks Inc.
- 1169 McIntyre, F. D., Drewery, J., Eerkes-Medrano, D., and Neat, F. C. (2016). Distribution and  
1170 diversity of deep-sea sponge grounds on the Rosemary Bank Seamount, NE Atlantic.  
1171 *Mar. Biol.* 163, 143. doi: 10.1007/s00227-016-2913-z
- 1172 Meyer, H. K., Roberts, E. M., Rapp, H. T., and Davies, A. J. (2019). Spatial patterns of arctic  
1173 sponge ground fauna and demersal fish are detectable in autonomous underwater  
1174 vehicle (AUV) imagery. *Deep Sea Res. Part Oceanogr. Res. Pap.* 153, 103137. doi:  
1175 10.1016/j.dsr.2019.103137
- 1176 Miatta, M., and Snelgrove, P. VR. (2021). Benthic nutrient fluxes in deep-sea sediments  
1177 within the Laurentian Channel MPA (eastern Canada): The relative roles of  
1178 macrofauna, environment, and sea pen octocorals. *Deep Sea Res. Part Oceanogr. Res.*  
1179 *Pap.* 178, 103655. doi: 10.1016/j.dsr.2021.103655
- 1180 Michna, P., and Woods, M. (2019). *RNetCDF: Interface to “NetCDF” Datasets*. Available  
1181 at: <https://CRAN.R-project.org/package=RNetCDF>
- 1182 Mienis, F., Duineveld, G. C. A., Davies, A. J., Ross, S. W., Seim, H., Bane, J., et al. (2012).  
1183 The influence of near-bed hydrodynamic conditions on cold-water corals in the  
1184 Viosca Knoll area, Gulf of Mexico. *Deep Sea Res. Part Oceanogr. Res. Pap.* 60, 32–  
1185 45. doi: 10.1016/j.dsr.2011.10.007
- 1186 Morganti, T. M., Slaby, B. M., de Kluijver, A., Busch, K., Hentschel, U., Middelburg, J. J., et  
1187 al. (2022). Giant sponge grounds of Central Arctic seamounts are associated with  
1188 extinct seep life. *Nat. Commun.* 13, 638. doi: 10.1038/s41467-022-28129-7
- 1189 Morrison, K. M., Meyer, H. K., Roberts, E. M., Rapp, H. T., Colaço, A., and Pham, C. K.  
1190 (2020). The First Cut Is the Deepest: Trawl Effects on a Deep-Sea Sponge Ground  
1191 Are Pronounced Four Years on. *Front. Mar. Sci.* 7. Available at:  
1192 <https://www.frontiersin.org/article/10.3389/fmars.2020.605281> (Accessed February 1,  
1193 2022).
- 1194 Murillo, F. J., Muñoz, P. D., Cristobo, J., Ríos, P., González, C., Kenchington, E., et al.  
1195 (2012). Deep-sea sponge grounds of the Flemish Cap, Flemish Pass and the Grand  
1196 Banks of Newfoundland (Northwest Atlantic Ocean): Distribution and species  
1197 composition. *Mar. Biol. Res.* 8, 842–854. doi: 10.1080/17451000.2012.682583

- 1198 Murillo, F., Kenchington, E., Tompkins, G., Beazley, L., Baker, E., Knudby, A., et al. (2018).  
1199 Sponge assemblages and predicted archetypes in the eastern Canadian Arctic. *Mar.*  
1200 *Ecol. Prog. Ser.* 597, 115–135. doi: 10.3354/meps12589
- 1201 Myers, R. A., Akenhead, S. A., and Drinkwater, K. (1990). The influence of Hudson Bay  
1202 runoff and ice-melt on the salinity of the inner Newfoundland Shelf. *Atmosphere-*  
1203 *Ocean* 28, 241–256. doi: 10.1080/07055900.1990.9649377
- 1204 Neuwirth, E. (2014). *RColorBrewer: ColorBrewer Palettes*. Available at: [https://CRAN.R-](https://CRAN.R-project.org/package=RColorBrewer)  
1205 [project.org/package=RColorBrewer](https://CRAN.R-project.org/package=RColorBrewer)
- 1206 Newton, P. P., Lampitt, R. S., Jickells, T. D., King, P., and Boutle, C. (1994). Temporal and  
1207 spatial variability of biogenic particles fluxes during the JGOFS northeast Atlantic  
1208 process studies at 47°N, 20°W. *Deep Sea Res. Part Oceanogr. Res. Pap.* 41, 1617–  
1209 1642. doi: 10.1016/0967-0637(94)90065-5
- 1210 Pedersen, T. L. (2019). *patchwork: The Composer of Plots*. Available at: [https://CRAN.R-](https://CRAN.R-project.org/package=patchwork)  
1211 [project.org/package=patchwork](https://CRAN.R-project.org/package=patchwork)
- 1212 Petrie, B., Akenhead, S. A., Lazier, J., and Loder, J. (1988). The cold intermediate layer on  
1213 the Labrador and Northeast Newfoundland Shelves, 1978–86.
- 1214 Pham, C. K., Murillo, F. J., Lirette, C., Maldonado, M., Colaço, A., Ottaviani, D., et al.  
1215 (2019). Removal of deep-sea sponges by bottom trawling in the Flemish Cap area:  
1216 conservation, ecology and economic assessment. *Sci. Rep.* 9, 15843. doi:  
1217 10.1038/s41598-019-52250-1
- 1218 Pile, A. J., and Young, C. M. (2006). The natural diet of a hexactinellid sponge: Benthic–  
1219 pelagic coupling in a deep-sea microbial food web. *Deep Sea Res. Part Oceanogr.*  
1220 *Res. Pap.* 53, 1148–1156. doi: 10.1016/j.dsr.2006.03.008
- 1221 Polunin; (2001). Feeding relationships in Mediterranean bathyal assemblages elucidated by  
1222 stable nitrogen and carbon isotope data. *Mar Ecol Prog Ser* 220, 13–23.
- 1223 Puerta, P., Johnson, C., Carreiro-Silva, M., Henry, L.-A., Kenchington, E., Morato, T., et al.  
1224 (2020). Influence of Water Masses on the Biodiversity and Biogeography of Deep-  
1225 Sea Benthic Ecosystems in the North Atlantic. *Front. Mar. Sci.* 7, 239. doi:  
1226 10.3389/fmars.2020.00239
- 1227 R Core Team (2019). R: A Language and Environment for Statistical Computing. Available  
1228 at: <https://www.R-project.org/>
- 1229 Radax, R., Rattei, T., Lanzen, A., Bayer, C., Rapp, H. T., Urich, T., et al. (2012).  
1230 Metatranscriptomics of the marine sponge *Geodia barretti*: tackling phylogeny and  
1231 function of its microbial community. *Environ. Microbiol.* 14, 1308–1324. doi:  
1232 10.1111/j.1462-2920.2012.02714.x
- 1233 Rivkin, R. B., Legendre, L., Deibel, D., Tremblay, J.-É., Klein, B., Crocker, K., et al. (1996).  
1234 Vertical Flux of Biogenic Carbon in the Ocean: Is There Food Web Control? *Science*  
1235 272, 1163–1166. doi: 10.1126/science.272.5265.1163
- 1236 Rix, L., de Goeij, J. M., Mueller, C. E., Struck, U., Middelburg, J. J., van Duyl, F. C., et al.  
1237 (2016). Coral mucus fuels the sponge loop in warm- and cold-water coral reef  
1238 ecosystems. *Sci. Rep.* 6, 18715. doi: 10.1038/srep18715

- 1239 Roberts, E. M., Mienis, F., Rapp, H. T., Hanz, U., Meyer, H. K., and Davies, A. J. (2018).  
1240 Oceanographic setting and short-timescale environmental variability at an Arctic  
1241 seamount sponge ground. *Deep Sea Res. Part Oceanogr. Res. Pap.* 138, 98–113. doi:  
1242 10.1016/j.dsr.2018.06.007
- 1243 Robertson, L. M., Hamel, J.-F., and Mercier, A. (2017). Feeding in deep-sea demosponges:  
1244 Influence of abiotic and biotic factors. *Deep Sea Res. Part Oceanogr. Res. Pap.* 127,  
1245 49–56. doi: 10.1016/j.dsr.2017.07.006
- 1246 Rooks, C., Fang, J. K.-H., Mørkved, P. T., Zhao, R., Rapp, H. T., Xavier, J. R., et al. (2020).  
1247 Deep-sea sponge grounds as nutrient sinks: denitrification is common in boreo-Arctic  
1248 sponges. *Biogeosciences* 17, 1231–1245. doi: 10.5194/bg-17-1231-2020
- 1249 Roy, V., Iken, K., and Archambault, P. (2014). Environmental Drivers of the Canadian Arctic  
1250 Megabenthic Communities. *PLOS ONE* 9, e100900. doi:  
1251 10.1371/journal.pone.0100900
- 1252 Schläppy, M.-L., Weber, M., Mendola, D., Hoffmann, F., and de Beer, D. (2010).  
1253 Heterogeneous oxygenation resulting from active and passive flow in two  
1254 Mediterranean sponges, *Dysida avara* and *Chondrosia reniformis*. *Limnol. Oceanogr.*  
1255 55, 1289–1300. doi: 10.4319/lo.2010.55.3.1289
- 1256 Sherwood, O. A., Davin, S. H., Lehmann, N., Buchwald, C., Edinger, E. N., Lehmann, M. F.,  
1257 et al. (2021). Stable isotope ratios in seawater nitrate reflect the influence of Pacific  
1258 water along the northwest Atlantic margin. *Biogeosciences* 18, 4491–4510. doi:  
1259 10.5194/bg-18-4491-2021
- 1260 Sherwood, O. A., Heikoop, J. M., Scott, D. B., Risk, M. J., Guilderson, T. P., and McKinney,  
1261 R. A. (2005). Stable isotopic composition of deep-sea gorgonian corals *Primnoa* spp.:  
1262 a new archive of surface processes. *Mar. Ecol. Prog. Ser.* 301, 135–148. doi:  
1263 10.3354/meps301135
- 1264 Sherwood, O. A., Jamieson, R. E., Edinger, E. N., and Wareham, V. E. (2008). Stable C and  
1265 N isotopic composition of cold-water corals from the Newfoundland and Labrador  
1266 continental slope: Examination of trophic, depth and spatial effects. *Deep Sea Res.*  
1267 *Part Oceanogr. Res. Pap.* 55, 1392–1402. doi: 10.1016/j.dsr.2008.05.013
- 1268 Shimeta, J., and Jumars, P. A. (1991). Physical mechanisms and rates of particle capture by  
1269 suspension feeders. *Ocean. Mar Biol Annu Rev*, 191–257.
- 1270 Shumway, R. H., Stoffer, D. S., and Stoffer, D. S. (2000). *Time series analysis and its*  
1271 *applications*. Springer.
- 1272 Sigman, D. M., Karsh, K. L., and Casciotti, K. L. (2009). “Nitrogen Isotopes in the Ocean,”  
1273 in *Encyclopedia of Ocean Sciences*, (Elsevier Ltd), 40–54. doi: 10.1016/B978-  
1274 012374473-9.00632-9
- 1275 signal developers (2014). *signal: Signal processing*. Available at: [http://r-forge.r-](http://r-forge.r-project.org/projects/signal/)  
1276 [project.org/projects/signal/](http://r-forge.r-project.org/projects/signal/)
- 1277 Smith, E. J., Soule, F. M., and Mosby, O. (1937). The Marion and General Greene  
1278 expeditions to Davis Strait and Labrador Sea. *US Coast Guard Bull* 19.
- 1279 Stoffer, D. (2020). *astsa: Applied Statistical Time Series Analysis*. Available at:  
1280 <https://CRAN.R-project.org/package=astsa>

- 1281 Straneo, F., and Saucier, F. (2008). The outflow from Hudson Strait and its contribution to  
1282 the Labrador Current. *Deep Sea Res. Part Oceanogr. Res. Pap.* 55, 926–946. doi:  
1283 10.1016/j.dsr.2008.03.012
- 1284 Sutcliffe, W. H. Jr., Loucks, R. H., Drinkwater, K. F., and Coote, A. R. (1983). Nutrient Flux  
1285 onto the Labrador Shelf from Hudson Strait and its Biological Consequences. *Can. J.*  
1286 *Fish. Aquat. Sci.* 40, 1692–1701. doi: 10.1139/f83-196
- 1287 Thomson, D. H. (1982). Marine Benthos in the Eastern Canadian High Arctic: Multivariate  
1288 Analyses of Standing Crop and Community Structure. *Arctic* 35, 61–74.
- 1289 Tremblay, J.-É., Gratton, Y., Carmack, E. C., Payne, C. D., and Price, N. M. (2002). Impact  
1290 of the large-scale Arctic circulation and the North Water Polynya on nutrient  
1291 inventories in Baffin Bay. *J. Geophys. Res. Oceans* 107, 26-1-26–14. doi:  
1292 10.1029/2000JC000595
- 1293 Turner, J. T. (2015). Zooplankton fecal pellets, marine snow, phytodetritus and the ocean's  
1294 biological pump. *Prog. Oceanogr.* 130, 205–248. doi: 10.1016/j.pocean.2014.08.005
- 1295 Vacelet, J., and Donadey, C. (1977). Electron microscope study of the association between  
1296 some sponges and bacteria. *J. Exp. Mar. Biol. Ecol.* 30, 301–314. doi: 10.1016/0022-  
1297 0981(77)90038-7
- 1298 van der Kaaden, A.-S., van Oevelen, D., Mohn, C., Soetaert, K., Rietkerk, M., van de Koppel,  
1299 J., et al. (2024). Resemblance of the global depth distribution of internal-tide  
1300 generation and cold-water coral occurrences. *Ocean Sci.* 20, 569–587. doi:  
1301 10.5194/os-20-569-2024
- 1302 van Duyl, F. C., Lengger, S. K., Schouten, S., Lundälv, T., van Oevelen, D., and Müller, C.  
1303 E. (2020). Dark CO<sub>2</sub> fixation into phospholipid-derived fatty acids by the cold-water  
1304 coral associated sponge *Hymedesmia* (*Stylopus*) *coriacea* (Tisler Reef, NE  
1305 Skagerrak). *Mar. Biol. Res.*, 1–17. doi: 10.1080/17451000.2019.1704019
- 1306 van Duyl, F., Hegeman, J., Hoogstraten, A., and Maier, C. (2008). Dissolved carbon fixation  
1307 by sponge–microbe consortia of deep water coral mounds in the northeastern Atlantic  
1308 Ocean. *Mar. Ecol. Prog. Ser.* 358, 137–150. doi: 10.3354/meps07370
- 1309 Vander Zanden, M. J., and Rasmussen, J. B. (2001). Variation in  $\delta^{15}\text{N}$  and  $\delta^{13}\text{C}$  trophic  
1310 fractionation: Implications for aquatic food web studies. *Limnol. Oceanogr.* 46, 2061–  
1311 2066. doi: 10.4319/lo.2001.46.8.2061
- 1312 Vaughan, D., and Dancho, M. (2020). *tibbletime: Time Aware Tibbles*. Available at:  
1313 <https://CRAN.R-project.org/package=tibbletime>
- 1314 Vieira, R. P., Bett, B. J., Jones, D. O. B., Durden, J. M., Morris, K. J., Cunha, M. R., et al.  
1315 (2020). Deep-sea sponge aggregations (*Pheronema carpenteri*) in the Porcupine  
1316 Seabight (NE Atlantic) potentially degraded by demersal fishing. *Prog. Oceanogr.*  
1317 183, 102189. doi: 10.1016/j.pocean.2019.102189
- 1318 Vogel, S. (1977). Current-induced flow through living sponges in nature. *Proc. Natl. Acad.*  
1319 *Sci.* 74, 2069–2071. doi: 10.1073/pnas.74.5.2069
- 1320 White, M. (2003). Comparison of near seabed currents at two locations in the Porcupine Sea  
1321 Bight—implications for benthic fauna. *J. Mar. Biol. Assoc. U. K.* 83, 683–686. doi:  
1322 10.1017/S0025315403007641h



- 1323 Whitney, F., Conway, K., Thomson, R., Barrie, V., Krautter, M., and Mungov, G. (2005).  
1324 Oceanographic habitat of sponge reefs on the Western Canadian Continental Shelf.  
1325 *Cont. Shelf Res.* 25, 211–226. doi: 10.1016/j.csr.2004.09.003
- 1326 Wickham, H. (2007). Reshaping Data with the reshape Package. *J. Stat. Softw.* 21, 1–20.
- 1327 Wickham, H. (2016). *ggplot2: Elegant Graphics for Data Analysis*. Springer-Verlag New  
1328 York. Available at: <https://ggplot2.tidyverse.org>
- 1329 Wickham, H., and Bryan, J. (2019). *readxl: Read Excel Files*. Available at: [https://CRAN.R-](https://CRAN.R-project.org/package=readxl)  
1330 [project.org/package=readxl](https://CRAN.R-project.org/package=readxl)
- 1331 Wilke, C. O. (2019). *cowplot: Streamlined Plot Theme and Plot Annotations for “ggplot2.”*  
1332 Available at: <https://CRAN.R-project.org/package=cowplot>
- 1333 Wilkinson, C. R., Garrone, R., Vacelet, J., and Smith, D. C. (1984). Marine sponges  
1334 discriminate between food bacteria and bacterial symbionts: electron microscope  
1335 radioautography and in situ evidence. *Proc. R. Soc. Lond. B Biol. Sci.* 220, 519–528.  
1336 doi: 10.1098/rspb.1984.0018
- 1337 Witte, U., Brattegard, T., Graf, G., and Springer, B. (1997). Particle capture and deposition  
1338 by deep-sea sponges from the Norwegian-Greenland Sea. *Mar. Ecol. Prog. Ser.* 154,  
1339 241–252. doi: 10.3354/meps154241
- 1340 Wu, Y., Peterson, I. K., Tang, C. C. L., Platt, T., Sathyendranath, S., and Fuentes-Yaco, C.  
1341 (2007). The impact of sea ice on the initiation of the spring bloom on the  
1342 Newfoundland and Labrador Shelves. *J. Plankton Res.* 29, 509–514. doi:  
1343 10.1093/plankt/fbm035
- 1344 Wurz, E., Beazley, L., MacDonald, B., Kenchington, E., Rapp, H. T., and Osinga, R. (2021).  
1345 The Hexactinellid Deep-Water Sponge *Vazella pourtalesii* (Schmidt, 1870)  
1346 (Rossellidae) Copes With Temporarily Elevated Concentrations of Suspended Natural  
1347 Sediment. *Front. Mar. Sci.* 8. doi: 10.3389/fmars.2021.611539
- 1348 Xie, Y. (2020). *knitr: A General-Purpose Package for Dynamic Report Generation in R*.  
1349 Available at: <https://yihui.org/knitr/>
- 1350 Yahel, G., Whitney, F., Reisinger, H. M., Eerkes-Medrano, D. I., and Leys, S. P. (2007). In  
1351 situ feeding and metabolism of glass sponges (Hexactinellida, Porifera) studied in a  
1352 deep temperate fjord with a remotely operated submersible. *Limnol. Oceanogr.* 52,  
1353 428–440. doi: 10.4319/lo.2007.52.1.0428
- 1354 Yashayaev, I. (2007). Hydrographic changes in the Labrador Sea, 1960–2005. *Prog.*  
1355 *Oceanogr.* 73, 242–276. doi: 10.1016/j.pocan.2007.04.015
- 1356 Yashayaev, I. (2024). Intensification and shutdown of deep convection in the Labrador Sea  
1357 were caused by changes in atmospheric and freshwater dynamics. *Commun. Earth*  
1358 *Environ.* 5, 1–23. doi: 10.1038/s43247-024-01296-9
- 1359 Yashayaev, I., and Loder, J. W. (2017). Further intensification of deep convection in the  
1360 Labrador Sea in 2016. *Geophys. Res. Lett.* 44, 1429–1438. doi:  
1361 10.1002/2016GL071668

## 1362 11 Supplementary material

## 1363 11.1 Tables

1364 *Table S1: Overview of lander deployment locations and CTD cast locations.*

station	instrument	date/period	latitude	longitude	depth
HSB bl	benthic lander	27-7-2018 to 2-7-2019	60.47	-61.29	410
LSB bl	benthic lander	27-7-2018 to 1-7-2019	59.38	-60.28	558
HSB ctd1	CTD	2018-08-03 07:37:08	60.47	-59.26	2428
HSB ctd2	CTD	2018-08-02 17:21:58	60.47	-60.38	1877
HSB ctd3	CTD	2018-07-30 15:27:05	60.47	-61.30	391
HSB ctd4	CTD	2018-07-30 07:31:07	60.46	-62.12	359
HSB ctd5	CTD	2018-07-27 19:41:58	60.40	-62.90	289
LSB ctd1	CTD	2018-07-29 04:30:19	59.53	-58.64	2563
LSB ctd2	CTD	2018-07-28 23:25:52	59.48	-59.45	1938
LSB ctd3	CTD	2018-07-28 09:52:11	59.38	-60.27	608
LSB ctd4	CTD	2018-07-28 06:12:07	59.31	-61.02	192
LSB ctd5	CTD	2018-07-28 03:10:24	59.22	-61.83	138

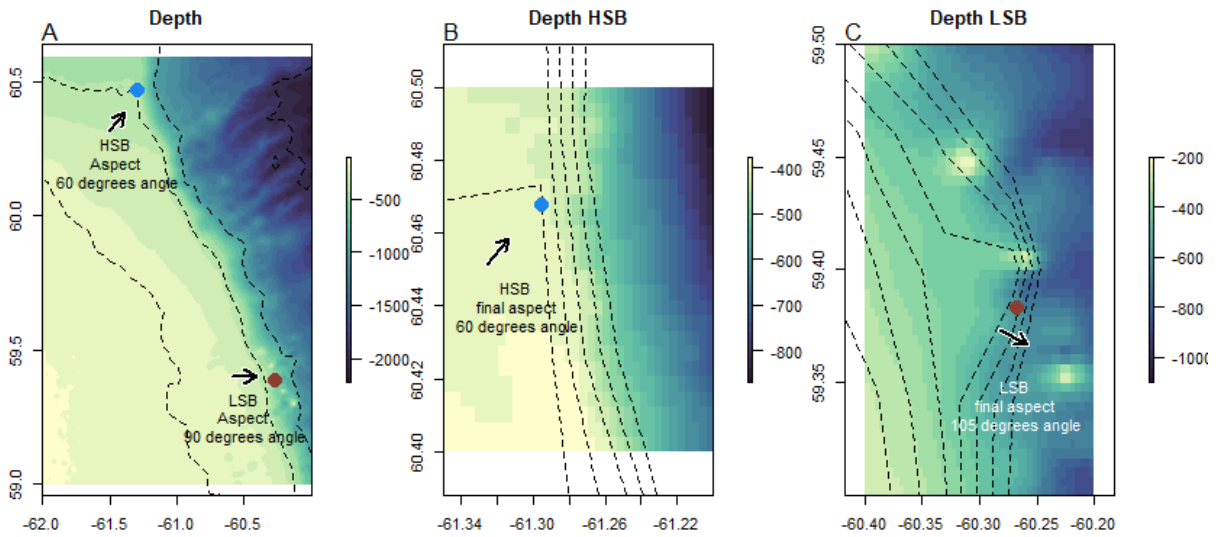
1365

1366 *Table S3: Overview of rock dredge transects. HSB = high-sponge-biomass site, LSB = low-sponge-biomass site, (Coté et al., 2019).*

1367

Station Name	Start Lat	Start Long	End Lat	End Long	Logged bottom depth (m)	Time at bottom (min)	Length of cable out (m)	Max vessel speed (knots)	Comments
LSB rd	59.38	-60.27	59.37	-60.29	552	10	1500	1	NA
HSB rd	60.47	-61.28	60.48	-61.30	404	20	507	2	Small catch

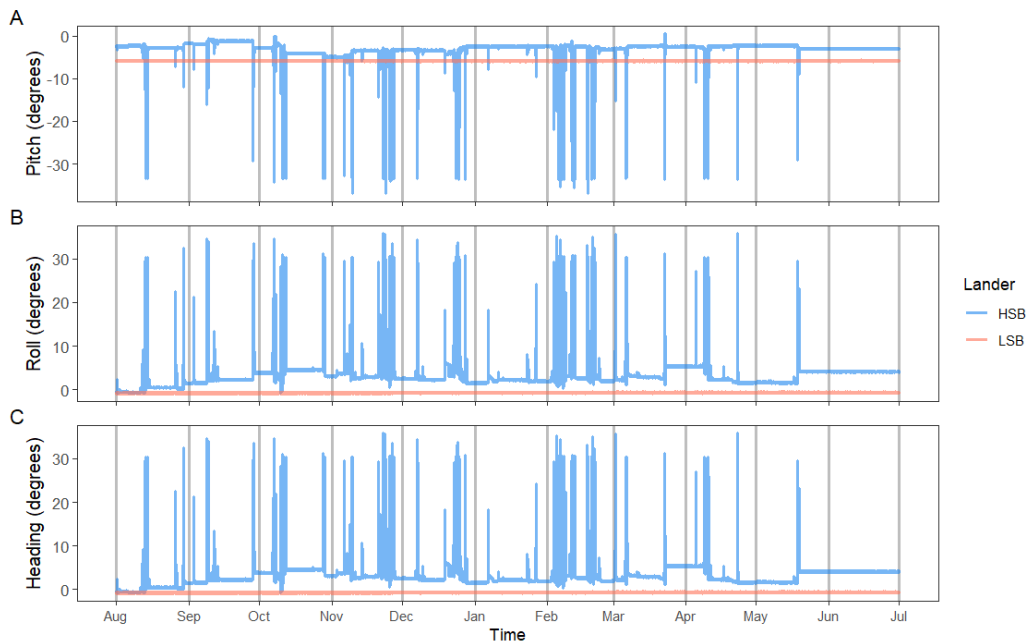
1368



1370

1371 *Figure S1: slope direction or aspect estimation for HSB and LSB. A) map of study area with estimated slope aspects of 60°*  
 1372 *and 90° angle for HSB and LSB, respectively. Contour lines at 200, 400, and 1000 metre is shown. B) expanded detail on*  
 1373 *HSB shows angle of 60° is a good estimate. Contour lines at 400, 425, 475, 500 are shown. C) expanded detail on LSB site*  
 1374 *shows angle of 105° is better estimate. Contour lines at 450, 475, 500, 525, 550, 575, 600 metre depth are shown. Note the*  
 1375 *different colour scales for depth. Locations of lander is indicated by coloured dots, with HSB = blue, and LSB = brown/red.*

1376

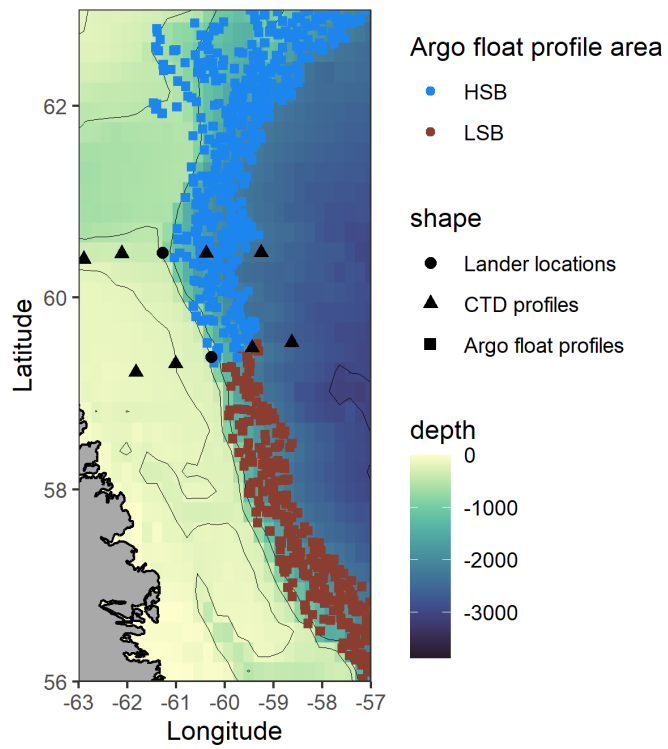


1377

1378 *Figure S2: Pitch (A), Roll (B), and Heading (C) data of the ADCPs from both benthic landers.*

1379

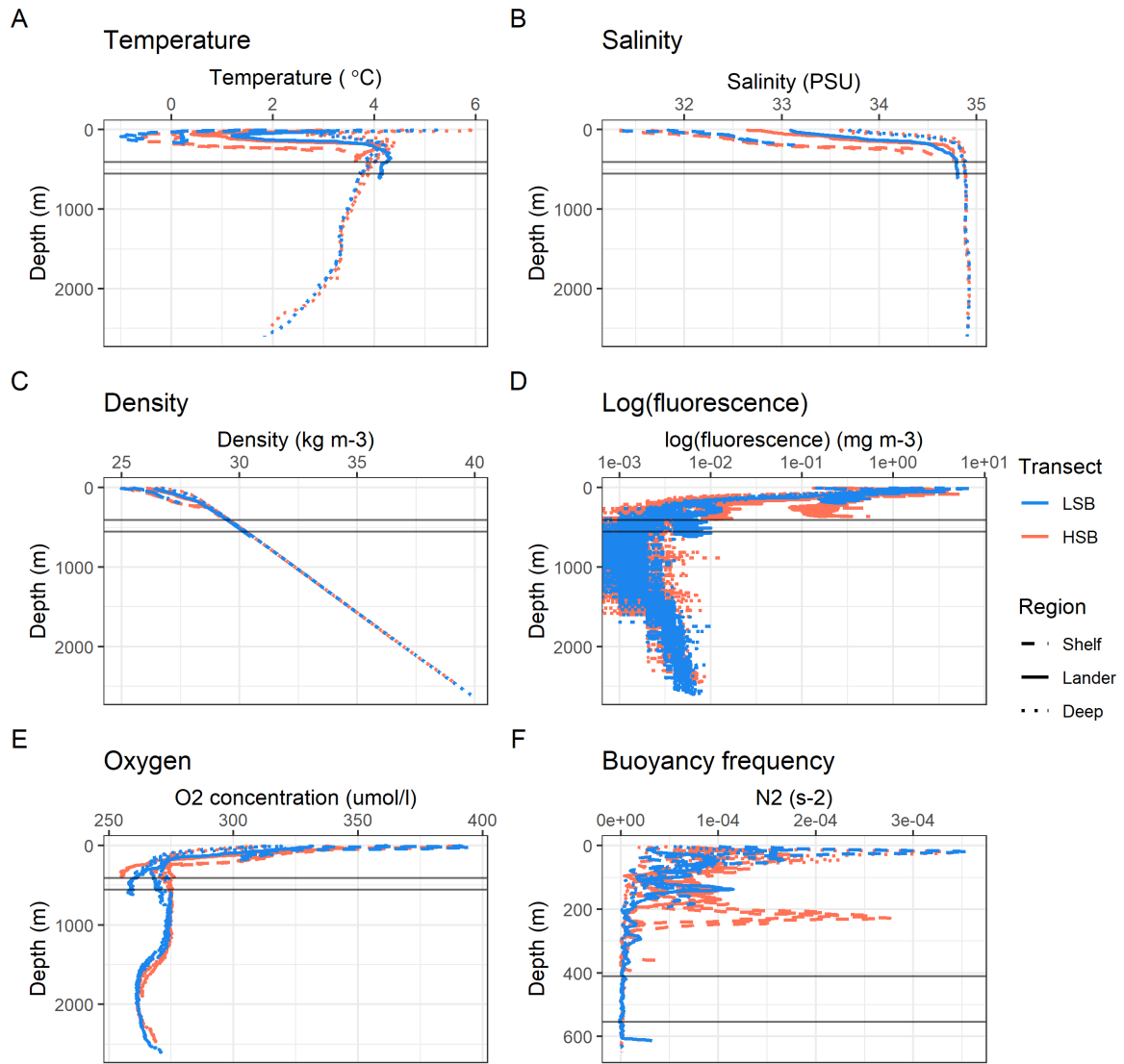
### Argofloat profile locations



1380

1381  
1382

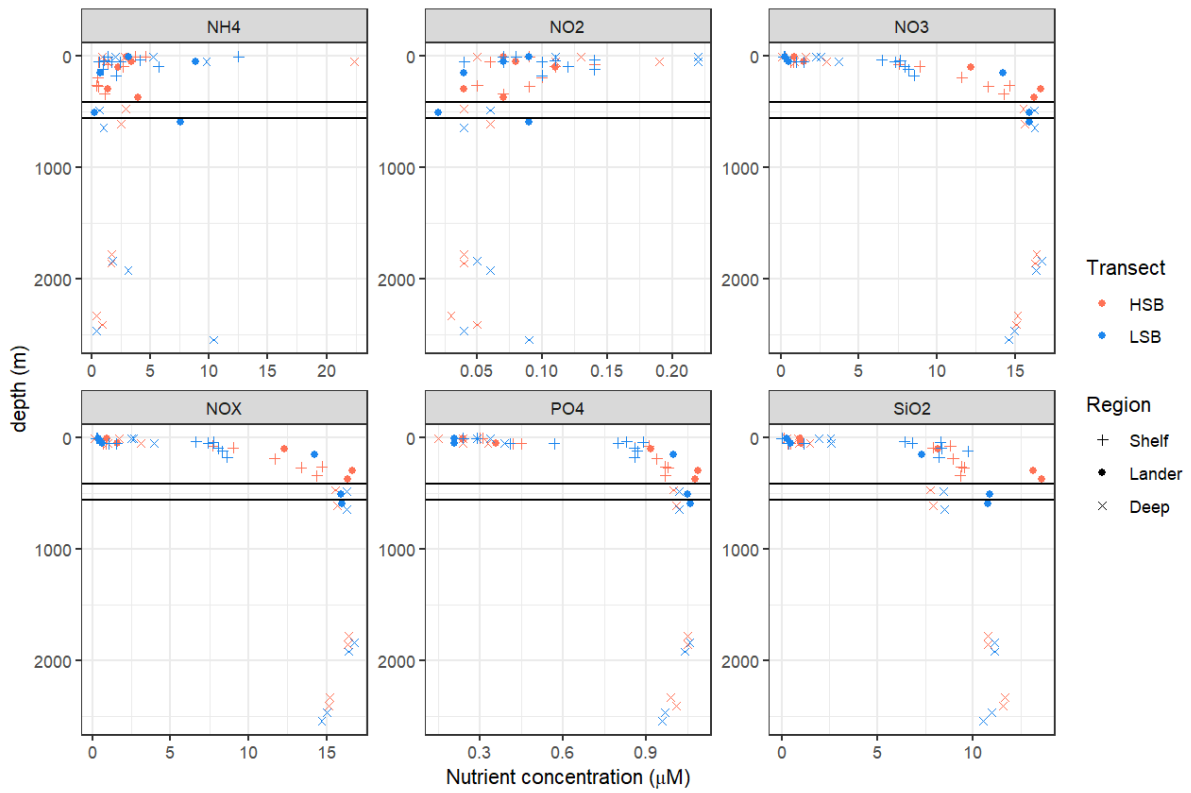
Figure S3: Locations of Argo float profiles used for assessing the regional oceanography. Coloured squares indicate Argo float profiles, and black triangles/dots the location of CTD profiles/benthic lander location.



1383

1384  
1385  
1386

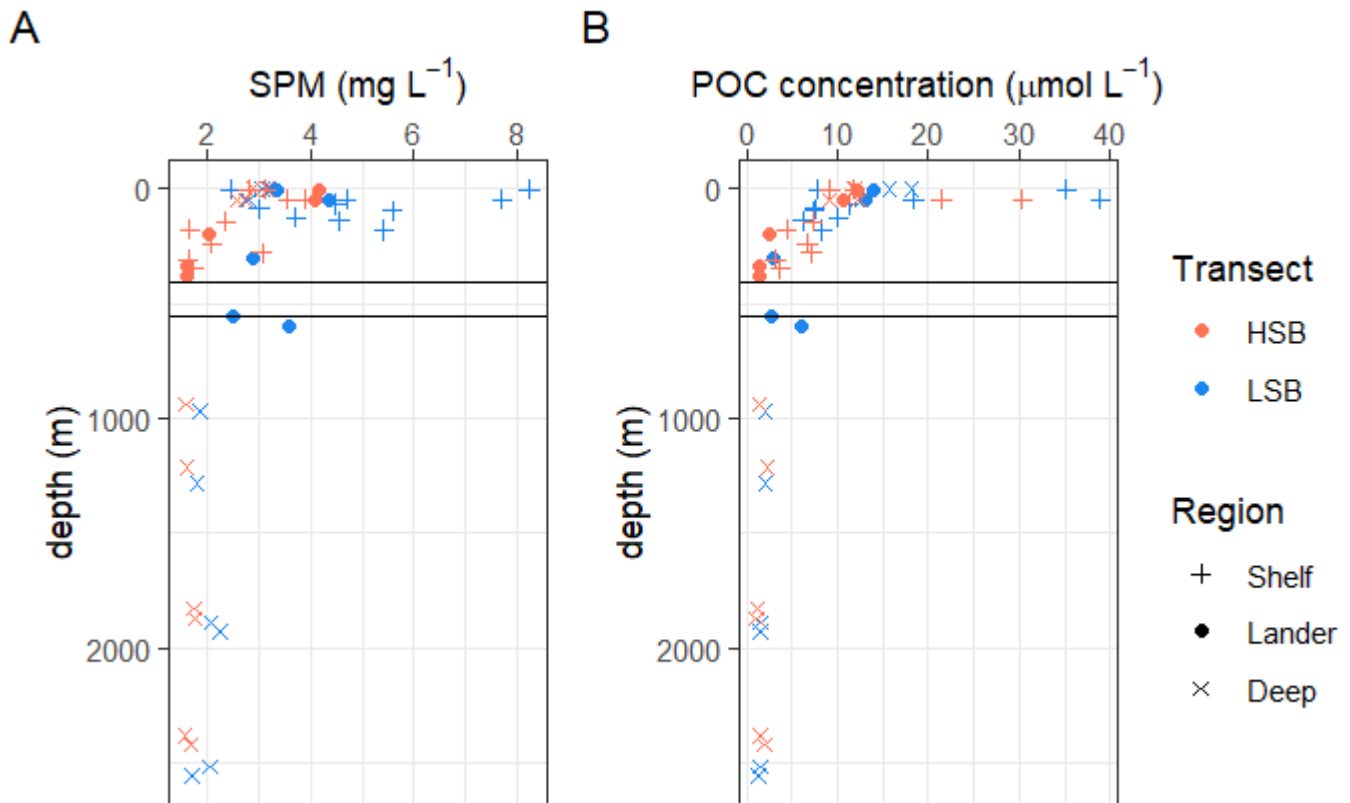
Figure S4: CTD profiles with temperature (A), salinity (B), density (C), Fluorescence (D), Oxygen (E), Buoyancy frequency (F). LSB = Low-sponge-biomass transect, HSB = High-sponge-biomass transect. Buoyancy frequency is smoothed over 15 m for visibility, and the plot only shows top 650 m of the water column, as deeper waters have values close to zero.



1387

1388  
1389

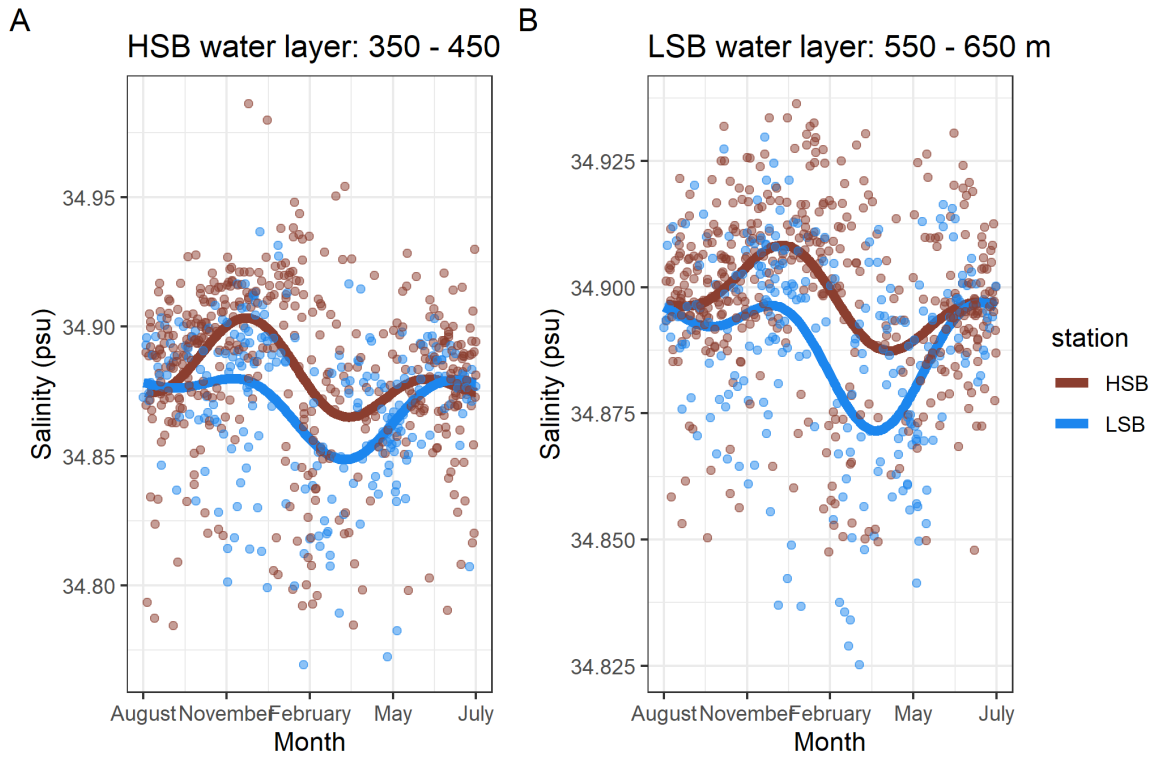
Figure S5: nutrient profiles for the two transects over the complete depth. HSB = high-sponge-biomass, LSB = low-sponge-biomass.



1390

1391  
1392  
1393

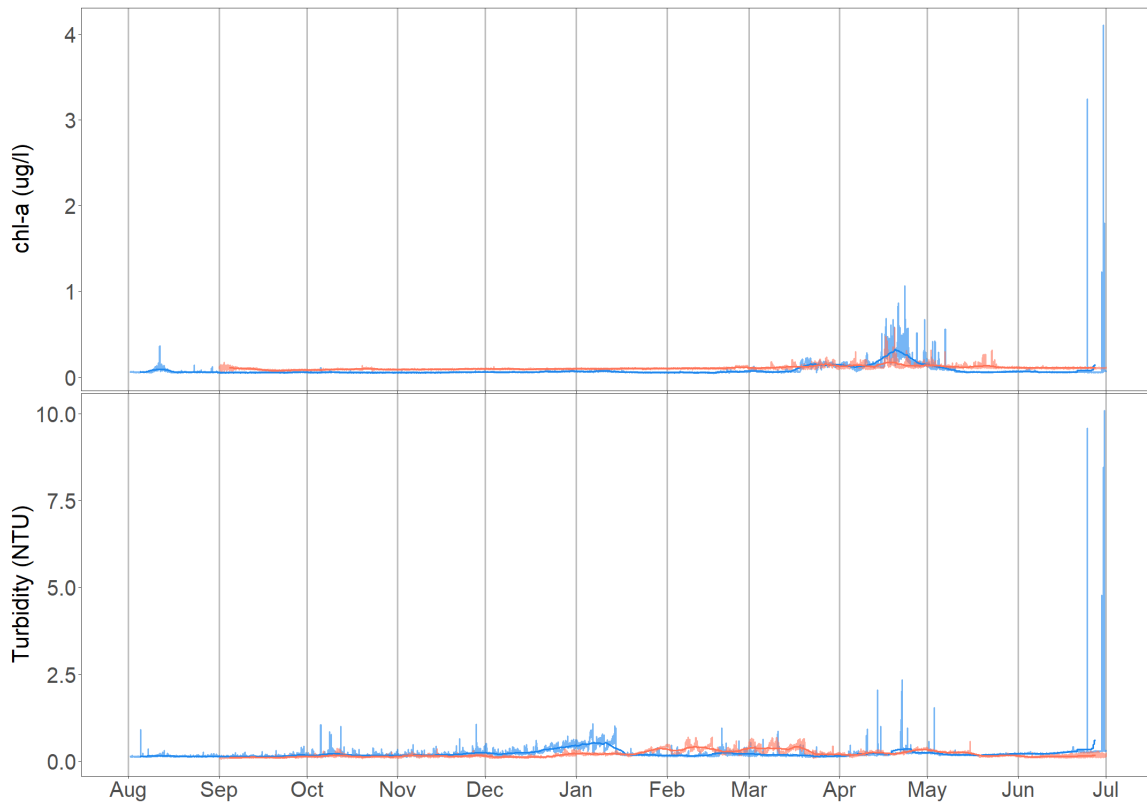
Figure S6: A) Suspended particulate matter (SPM) concentration and B) particulate organic carbon concentration of the CTD the two transects. HSB = high-sponge-biomass transect, LSB = low-sponge-biomass transect. The horizontal lines resemble depth of benthic landers, where the top line is the HSB lander depth, and lowest line resembles LSB lander depth.



1394

1395  
1396

Figure S7: A) seasonal salinity, from Argo float data, of the water layer in which HSB lander is located. B) seasonal salinity of the water layer in which LSB is located.



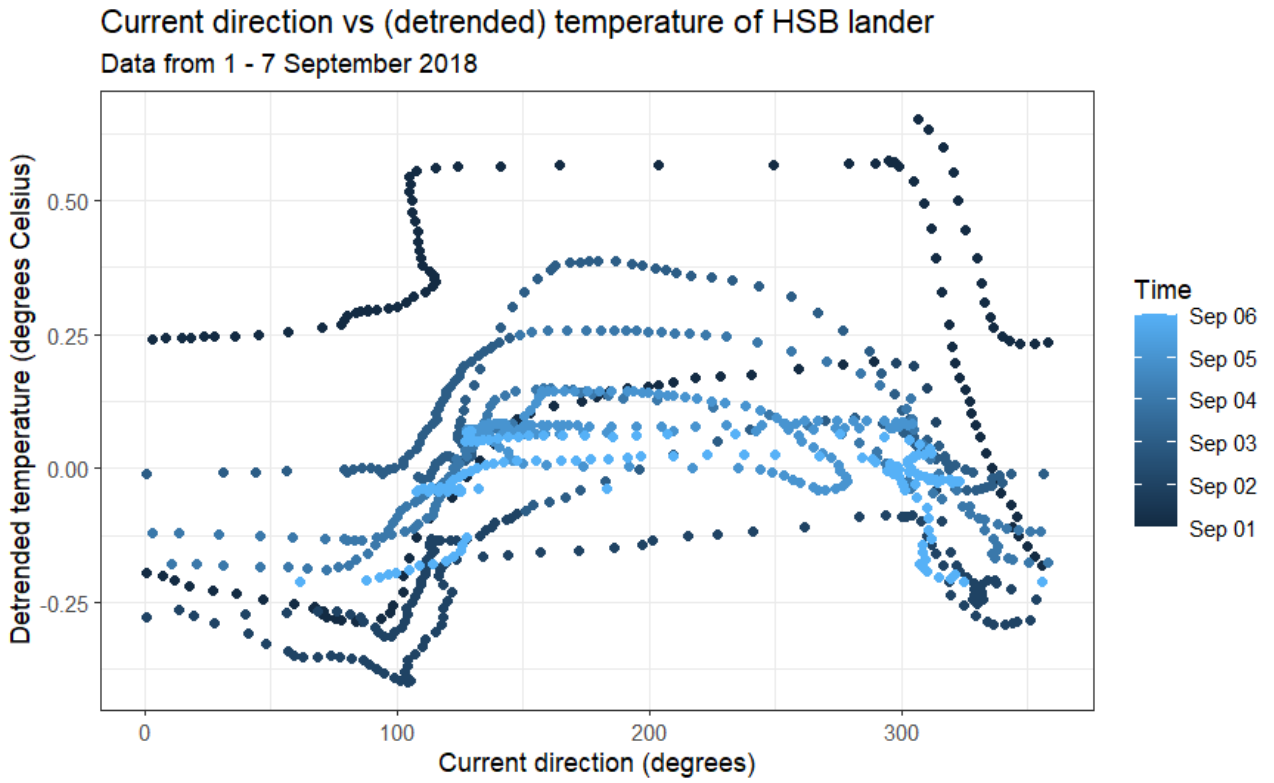
1397

1398

Figure S8: Chlorophyll-a and turbidity data without cutting the y-axis at  $1.25 \mu\text{g L}^{-1}$ , and 2.5 NTU, respectively.

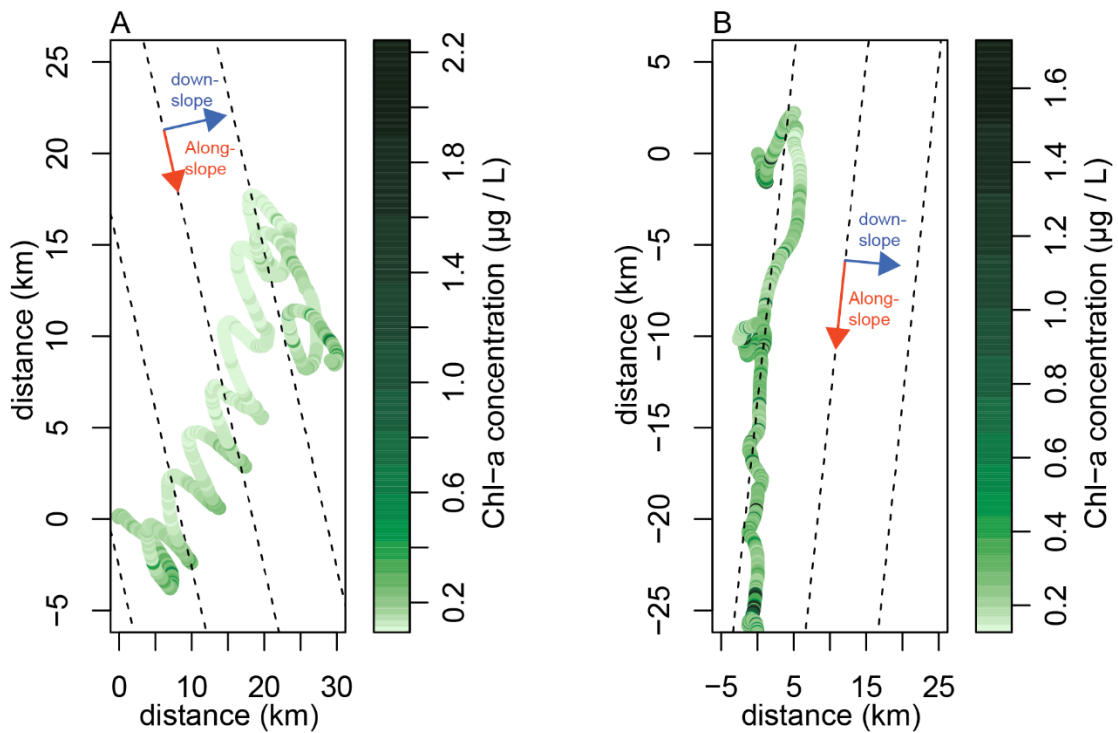
1399

1400



1401

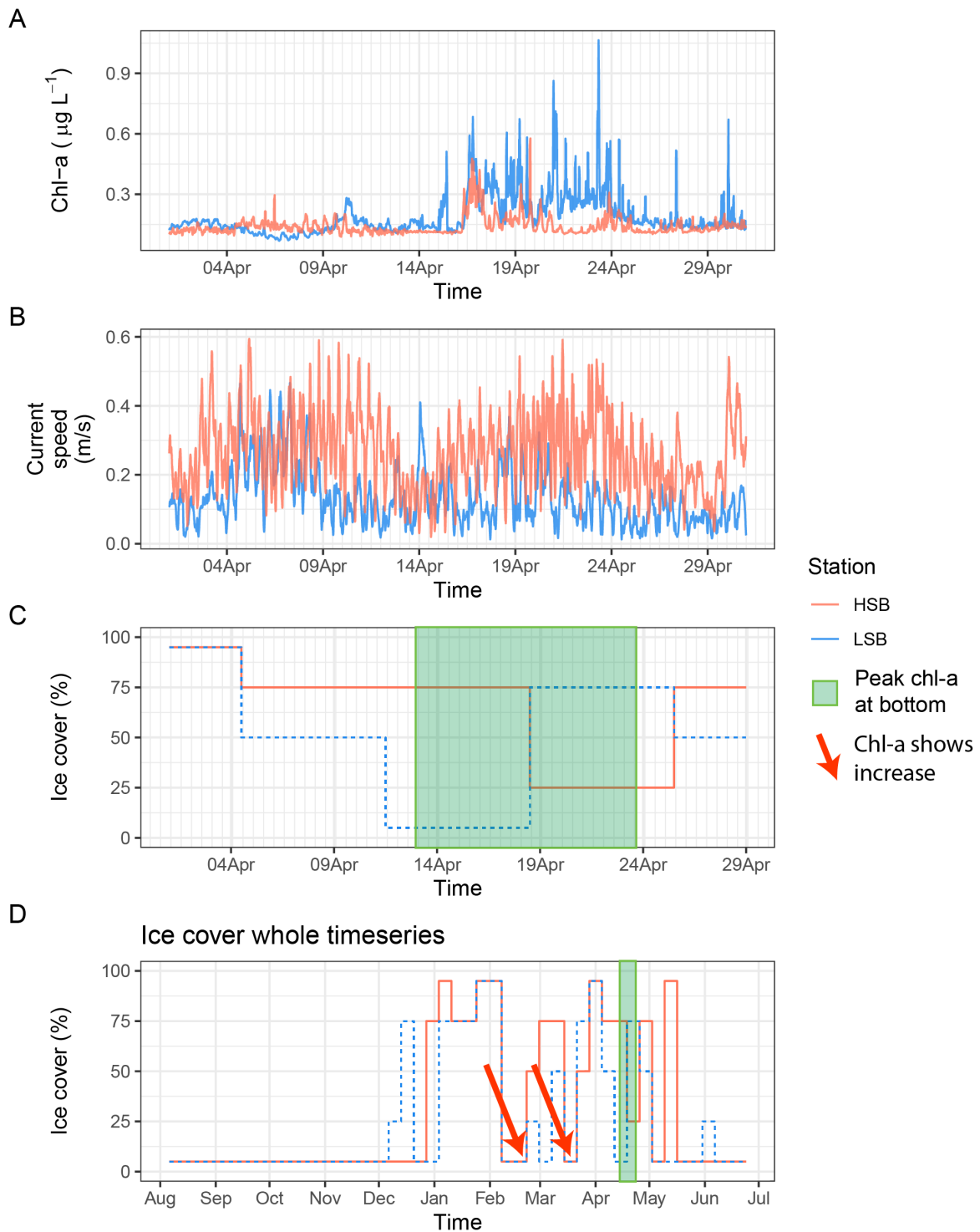
1402 *Figure S9: bottom current direction and (detrended temperature at the HSB lander with data from 1 - 7 September 2018.*



1403

1404 *Figure S10: progressive vector plots with chlorophyll-a as colour variable from 19 to 24 April 2019. With A) the high-*  
1405 *sponge-biomass (HSB) lander and b) the low-sponge-biomass (LSB) lander. Dotted lines represent the along slope direction*  
1406 *at the respective sites. Note colour is in log-scale.*





1407

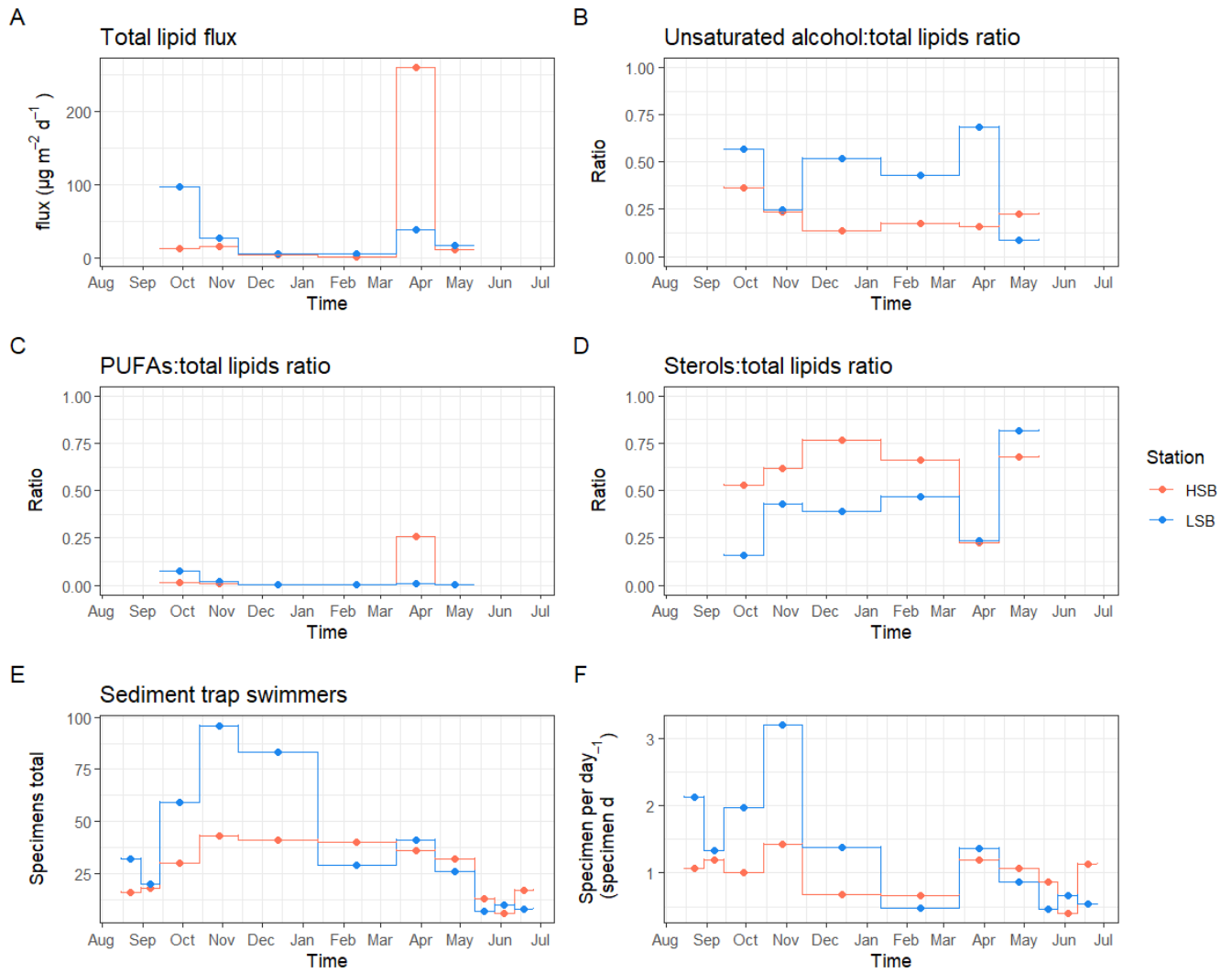
1408

1409

1410

1411

Figure S11: Spring Chlorophyll-a (A), bottom current speed (B), ice cover (C), during the spring bloom period (1 April-1 May, 2019), and ice cover for the whole deployment length (D). Green squares indicate peak bottom chl-a concentrations measured (Figure 9 in the paper), red arrows indicate moment after which chl-a increases at both landers (Figure 9 in paper).



1412

1413

1414

1415

Figure S12: Sediment trap lipid fluxes. A) Total lipid flux, B) unsaturated alcohol:total lipids ratio, C) poly-unsaturated fatty acid:total lipids ratio, D) sterol:total lipids ratio. E) Swimmers inside sediment trap bottles F) Swimmers per bottle divided by days that bottle was open.